PROTON-COUPLED ELECTRON TRANSFER IN MOLECULAR AND MATERIAL CATALYSIS

BY

APARNA KARIPPARA HARSHAN

DISSERTATION

Submitted in partial fulfillment of the requirements
for the degree of Doctor of Philosophy in Chemistry
in the Graduate College of the
University of Illinois at Urbana-Champaign, 2018

Urbana, Illinois

Doctoral Committee:

Professor Nancy Makri, Chair
Professor Sharon Hammes-Schiffer, Director of Research
Assistant Professor Joshua Vura-Weis
Assistant Professor Lisa Olshansky

ABSTRACT

Proton-coupled electron transfer (PCET) plays an important role in a variety of electrochemical and photo-excited reactions occurring in molecular, material, and biological systems. In this thesis, the role of PCET in hydrogen evolution molecular electrocatalysts, and iron-doped nickel-oxyhydroxide thin films used for oxygen evolution reaction, are explored by means of quantum chemistry. Detailed electronic structural analysis performed using density functional theory is used to provide atomic level understanding of these catalytic systems. The electron-proton nonadiabaticity of PCET process is investigated for the phenoxyl/phenol self-exchange reaction, and the results show that the vibronic coupling is dependent on the molecular geometry. This diagnostic is important for the calculation of PCET rate constants. The rate constants and kinetic isotope effects for concerted PCET in a set of hydroquinone derivatives are calculated and analyzed in comparison with experimental data.

ACKNOWLEDGEMENTS

Firstly, I would like to thank my advisor, Prof. Sharon Hammes-Schiffer, for her guidance, support, and mentorship during my doctoral studies. I am grateful to be able to learn how to look simultaneously at both the broad view and the minute details relevant in research, thereby able to view various perspectives to approach scientific problems.

Over the period of five years, I have had the opportunity to work closely with several group members and learned something novel every time. I would like to thank Dr. Brian Solis and Dr. Andrew Sirjoosingh for their help in my first year of graduate school, when I had started with iron-glyoxime project and phenoxyl/phenol project. I am also grateful towards Zachary Goldsmith, with whom I worked on the NiFeOOH system, and whose experience with periodic density functional theory was a great help for me. I am thankful to Dr. Mioy Huynh for his enthusiastic help and cooperation in the hydroquinone project. I am also thankful to Dr. Soumya Ghosh and Dr. Puja Goyal for their help and advice at various stages of my research projects. I am also thankful to Dr. Alexander Soudackov, who helped me with multiple projects, for his constant guidance. His encouragement to delve deeper into the underlying physics of systems under study has been very inspiring.

Three of the four projects I worked on have been collaborations with experimentalists, and one of them was also in collaboration with another theory group. The experience gained from working with specialists of different areas has widened my perspectives and augmented my skills as a researcher. For this I am thankful to both my advisor and my funding agency, the Center for Chemical Innovation, for providing me with the opportunity to gain exposure to different fields of chemical research. I would like to thank Prof. Harry Gray and Prof. Jay Winkler at CalTech, Prof. Giulia Galli and Dr. Marton Vörös at the University of Chicago, and Prof. Shannon Stahl and Dr. James Gerken at the University of Wisconsin Madison, and Prof. Massimo Bietti at the University of Rome Tor Vergata for their cooperation, especially for adding their intuitive insights from experience in their own field of research that ended up being helpful in theoretical investigations by our group.

As an international student coming to the United States for the first time, also as an introverted person, my advisor and my research group has been immensely accommodative towards me, and for this I would like to thank each one of them. Finally, I would like to thank my family - my parents and my younger brother, whose emotional support throughout my undergraduate and graduate years has been vital for me in pursuing a career in basic science.

TABLE OF CONTENTS

CHAPTER 1: Introduction

Reactions classified as proton-coupled electron transfer (PCET) can range from sequential one-electron one-proton transfer processes common in electrocatalytic processes, to multiple concerted proton transfer processes.[1-5] A schematic representation of PCET between molecules is depicted in Figure 1.1. PCET is central for many types of applications, such as electrocatalysis, solar cells, artificial photosynthesis, and biological systems.[6-7] PCET is an important part of molecular and material electrocatalysis for hydrogen and oxygen evolution processes in fuel cells. Several such catalysts have been studied experimentally and computationally,[5, 8-11] and the possibility of designing new and efficient electrocatalysts from earth-abundant elements is significant to the development of alternative energy sources. PCET reactions can also be found in enzyme catalysis[12] and biomimetic systems.[13]

The application of PCET theories to enzymatic reactions helps the understanding of important biological processes. PCET processes are also observed in photo-induced reactions, in which case the excited states become significant, and the coupling between electronic and vibrational states could cause complex reaction mechanisms.[14-16] In all of these examples, elucidation of the mechanism and factors affecting it can be useful in tuning the relevant systems to exhibit desired properties, such as increased turnover number or smaller overpotential. The challenges to do so using quantum chemical methods arise from the coupling of electron and proton motion, and how it is treated computationally. In this thesis, various aspects and applications of PCET reactions are investigated using different computational and theoretical methods that are chosen as suitable for each system.

In Chapter 2, density functional theory (DFT) is used to study a set of fluorinated diglyoxime-iron complexes, $[(dAr^{F}gBF_2)_2Fe(py)_2]$ (**A**), and $[(dAr^{F}g_2H\text{-}BF_2)Fe(py)_2]$ (**B**), which have been shown to evolve hydrogen at moderate overpotentials. **B** differs from **A** in that one BF_2 bridge is replaced by a proton bridge of the form O-H-O. The experimentally observed turnover numbers and catalytic efficiency for the system with the proton bridge was almost double that of the system with the BF_2 bridge.[17] By investigating all possible reaction intermediates involved in the hydrogen evolution reaction (HER) pathways for both compounds, the catalysis in **B** was found to proceed via two parallel pathways, where one pathway is similar to that for **A**, and the additional pathway arises from protonation of the O-H-O bridge, followed by spontaneous reduction to an Fe^0 intermediate and intramolecular proton transfer from the ligand to the metal center to form the same active Fe^{II}-hydride species. The calculations predict that the relative probabilities for the two pathways, and therefore the relative magnitudes of the catalytic peaks, could be tuned by altering the pK_a of the acid or the substituents on the ligands of the electrocatalysts.[18] The ability to tune the catalytic pathways through acid strength or ligand substituents is important for designing more effective catalysts for energy conversion processes.

Whereas Chapter 2 deals with molecular electrocatalysts in solution, the next chapter expands upon the application of periodic DFT to understand the detailed electronic structure of a thin film catalytic material. NiFe oxyhydroxide materials are highly active electrocatalysts for the oxygen evolution reaction (OER), an important process for carbon-neutral energy storage. Recent spectroscopic and computational studies increasingly support iron as the site of catalytic activity but differ with respect to the relevant iron redox state.[19] A combination of hybrid periodic DFT calculations and spectroelectrochemical experiments elucidate the electronic structure and redox thermodynamics of Ni-only and mixed NiFe oxyhydroxide thin-film electrocatalysts. The ultraviolet/visible light absorbance of the Ni-only catalyst depends on the applied potential as metal ions in the film are oxidized prior to the onset of OER activity. In contrast, absorbance changes are negligible in a 25% Fe-doped catalyst up to the onset of OER activity. First principles calculations of proton-coupled redox potentials and magnetizations reveal that the Ni-only system features oxidation of Ni^{2+} to Ni^{3+}, followed by oxidation to a mixed $Ni^{3+/4+}$ state at a potential coincident with the onset of OER activity. Calculations on the 25% Fe-doped system show the catalyst is redox inert prior to the onset of catalysis, which coincides with the formation of Fe^{4+} and mixed Ni oxidation states. The calculations indicate that introduction of Fe dopants changes the character of the conduction band minimum from Ni-oxide in the Ni-only to predominantly Fe-oxide in the NiFe electrocatalyst. These findings provide a unified experimental and theoretical description of the electrochemical and optical properties of Ni and NiFe oxyhydroxide electrocatalysts and serve as an important benchmark for computational characterization of mixed-metal oxidation states in heterogeneous catalysts.[20]

In both Chapters 2 and 3, the PCET processes were expected to occur mainly adiabatically, but this is not always the case. Chapter 4 probes a prototypical example of a nonadiabatic PCET process, the phenoxyl/phenol system, and the factors affecting the adiabatic or nonadiabatic nature of PCET. The electron-proton nonadiabaticity of PCET reactions can be determined by a semiclassical method using an adiabaticity parameter p defined as the ratio of an effective proton tunneling time and an electronic transition time:

$$p = \frac{\tau_{\mathrm{p}}}{\tau_{\mathrm{e}}} \tag{1-1}$$

The effective electronic transition time τ_{e} between two states coupled by V^{el} is given by

$$\tau_{\mathrm{e}} = \frac{\hbar}{V^{\mathrm{el}}} \tag{1-2}$$

which is in the form of time-energy uncertainty relation, and is equivalent to the period of Rabi oscillations in a two-level system.

The effective proton tunneling time τ_{p} can be determined through a simple curve crossing formulation. In this formulation, the region where the electronic transition occurs can be characterized by a width dx defined as

$$dx \approx \frac{V^{\mathrm{el}}}{\left|\Delta F\right|} \tag{1-3}$$

where V^{el} is the electronic coupling between the diabatic electronic states with potentials $V_1(\mathrm{x})$ and $V_2(\mathrm{x})$, and $|\Delta F|$ is the difference between the slopes of the two diabatic potentials at the crossing point:

$$\left|\Delta F\right| = \left|\frac{dV_2}{dx} - \frac{dV_1}{dx}\right| \tag{1-4}$$

The effective proton tunneling time through this region of width dx can then be expressed as

$$\tau_{\mathrm{p}} = \frac{V^{\mathrm{el}}}{\left|\Delta F\right| v_t} \tag{1-5}$$

where v_t is the tunneling velocity of the proton defined as

$$v_t = \sqrt{\frac{2(V_\mathrm{c} - E)}{m_\mathrm{p}}} \tag{1-6}$$

Here V_c is the energy at which the potential energy curves cross, m_p is the proton mass, and E is the tunneling energy, which is defined as the energy of the degenerate proton vibrational levels in the reactant and product potential wells.

The adiabaticity parameter p is defined as the ratio of the proton tunneling time and the electronic transition time:

$$p = \frac{\tau_\mathrm{p}}{\tau_\mathrm{e}} = \frac{\left|V_{12}\right|^2}{\hbar\left|\Delta F\right|\upsilon_t} \tag{1-7}$$

This is reminiscent of the well-known expression for the parameter γ_{LZ} in the Landau-Zener probability[21-22] of the transition between the two linear intersecting terms

$$P_{\mathrm{LZ}} = 1 - \exp(-2\pi\gamma_{\mathrm{LZ}}) \tag{1-8}$$

where

$$\gamma_{\mathrm{LZ}} = \frac{\left|V_{12}\right|^2}{\hbar\left|\alpha\right|} \tag{1-9}$$

where α is the model parameter describing the linear time dependence of the energy gap

$$V_2(t) - V_1(t) = \alpha t \tag{1-10}$$

Assuming that the proton is moving with constant tunneling velocity υ_t the parameter α can be expressed as

$$\alpha = v_t \Delta F \tag{1-11}$$

thus leading to a formally equivalent expression as given above for the adiabaticity parameter p. It should be noted, however, that the analogy with the Landau-Zener model is purely formal because the inter-level transition in the Landau-Zener model does not involve tunneling along the classical coordinate *x*, which is treated classically as an external time-dependent parameter.

It should be noted that the effective proton tunneling time utilized in this semiclassical formalism is an experimentally inaccessible measure of how fast or slow the proton moves in the small region near the crossing point of the diabatic potentials. This effective proton tunneling time is not related to the physical motion of a proton or to the tunneling splitting. In the well-known case of proton tunneling in the malonaldehyde molecule, which is a classic example for a symmetric double well potential, the tunneling splitting was found to be 21.58 cm^{-1} using microwave spectroscopic studies,[23] which corresponds to 1.5 ps, about two orders of magnitude larger than the effective proton tunneling times τ_p reported in Chapter 4. This tunneling splitting is related to the vibronic coupling that appears as a squared prefactor in the vibronically nonadiabatic PCET rate constant expressions discussed in Chapter 5. In the electronically adiabatic limit, the vibronic coupling for PCET reactions is half the tunneling splitting associated with the electronic ground state proton potential. In general, this form of the vibronic coupling must be multiplied by the factor

$$\kappa = \sqrt{2\pi p}\,\frac{e^{p\ln p-p}}{\Gamma(p+1)} \tag{1-12}$$

Most PCET rate constant expressions rely on the Condon approximation, which assumes that the vibronic coupling is independent of the nuclear coordinates of the solute and the solvent or protein. Herein we test the Condon approximation for PCET vibronic couplings. The dependence of the vibronic coupling on molecular geometry is investigated for an ‘open’ and a ‘stacked’ transition state geometry of the phenoxyl-phenol self-exchange reaction. The calculations indicate that the open geometry is electronically nonadiabatic, corresponding to an electron-proton transfer (EPT) mechanism that involves significant electronic charge redistribution, while the stacked geometry is predominantly electronically adiabatic, corresponding primarily to a hydrogen atom transfer (HAT) mechanism with negligible electronic charge redistribution. Consequently, a single molecular system can exhibit both HAT and EPT character. Thus, the Condon approximation is shown to be invalid for the solute nuclear coordinates in certain PCET systems. These results have significant implications for the calculation of rate constants, as well as mechanistic interpretations, of PCET reactions.[24]

In chapter 5, the PCET rate constant expressions mentioned above are used to investigate a chemically and biologically significant system exhibiting concerted PCET. Benzoquinone/hydroquinone couples play an important role in charge transfer processes associated with photosynthesis and respiration.[25-27] The reactions of cumyloxyl radial ($CumO^{\bullet}$) with two hydroquinone derivatives, one with and one without an intra-molecular hydrogen bond, were studied using laser flash photolysis, and the spectroscopic results suggested that the intramolecularly hydrogen bonded system undergoes concerted E2PT, where the electron transfer is accompanied by two proton transfers, an inter-molecular PT between the radical and the quinone system, and an intermolecular PT between the oxygen of the quinone and the nitrogen of the piperidyl substituent ring. Computationally, the PCET rate constants were calculated by thermal averaging of rate constants calculated from a vibronically nonadiabatic expression.[2, 28-29] The potential energy surfaces for the single and double proton transfer reactions were generated using constrained DFT with configuration interaction (CDFT-CI). The concerted PCET with smaller kinetic isotope effect (KIE) was shown to be having contributions from higher excited states to the overall rate.

1.1. Figure

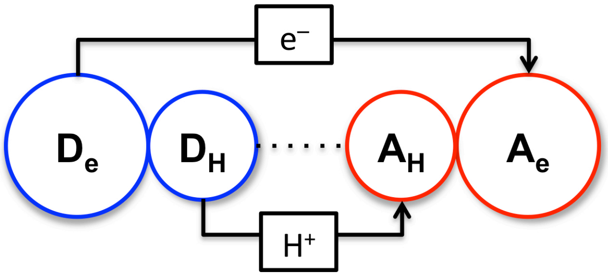

Figure 1.1. Simplified schematic of a PCET process where one electron and one proton are transferred across D_eD_H to A_eA_H. Here, D_e is electron donor and A_e is electron acceptor. D_H and A_H are proton donor and acceptor, respectively. D_e and D_H can be the same atom in a molecule, or they could be different atoms in the same molecule. Electron and proton transfer can also happen in opposite direction.

1.2. References

1. Cukier, R.; Nocera, D. G., Proton-coupled electron transfer. *Ann. Rev. Phys. Chem.* **1998,** *49*, 337-369.

2. Hammes-Schiffer, S.; Soudackov, A. V., Proton-coupled electron transfer in solution, proteins, and electrochemistry. *J. Phys. Chem. B* **2008,** *112* (45), 14108-14123.

3. Warren, J. J.; Tronic, T. A.; Mayer, J. M., Thermochemistry of proton-coupled electron transfer reagents and its implications. *Chem. Rev.* **2010,** *110*, 6961-7001.

4. Auer, B.; Fernandez, L. E.; Hammes-Schiffer, S., Theoretical analysis of proton relays in electrochemical proton-coupled electron transfer. *J. Am. Chem. Soc* **2011,** *133* (21), 8282-8292.

5. Solis, B. H.; Hammes-Schiffer, S., Proton-coupled electron transfer in molecular electrocatalysis: Theoretical methods and design principles. *Inorg. Chem.* **2014,** *53* (13), 6427-6443.

6. Huynh, M. H. V.; Meyer, T. J., Proton-coupled electron transfer. *Chem. Rev.* **2007,** *107* (11), 5004-5064.

7. Hammes-Schiffer, S.; Stuchebrukhov, A. A., Theory of coupled electron and proton transfer reactions. *Chem. Rev.* **2010,** *110* (12), 6939-6960.

8. Dempsey, J. L.; Brunschwig, B. S.; Winkler, J. R.; Gray, H. B., Hydrogen evolution catalyzed by cobaloximes. *Acc. Chem. Res.* **2009,** *42* (12), 1995-2004.

9. Horvath, S.; Fernandez, L. E.; Soudackov, A. V.; Hammes-Schiffer, S., Insights into proton-coupled electron transfer mechanisms of electrocatalytic H_2 oxidation and production. *Proc. Natl. Acad. Sci. U.S.A.* **2012,** *109* (30), 15663-15668.

10. Burke, M. S.; Enman, L. J.; Batchellor, A. S.; Zou, S.; Boettcher, S. W., Oxygen evolution reaction electrocatalysis on transition metal oxides and (oxy)hydroxides: Activity trends and design principles. *Chem. Mater.* **2015,** *27*, 7549-7558.

11. Ghosh, S.; Castillo-Lora, J.; Soudackov, A. V.; Mayer, J. M.; Hammes-Schiffer, S., Theoretical insights into proton-coupled electron transfer from a photoreduced ZnO nanocrystal to an organic radical. *Nano Lett.* **2017,** *17* (9), 5762-5767.

12. Schilter, D.; Camara, J. M.; Huynh, M. T.; Hammes-Schiffer, S.; Rauchfuss, T. B., Hydrogenase enzymes and their synthetic models: the role of metal hydrides. *Chem. Rev.* **2016,** *116* (15), 8693-8749.

13. Huynh, M. T.; Mora, S. J.; Villalba, M.; Tejeda-Ferrari, M. E.; Liddell, P. A.; Cherry, B. R.; Teillout, A.-L.; Machan, C. W.; Kubiak, C. P.; Gust, D.; Moore, T. A.; Hammes-Schiffer, S.; Moore, A. L., Concerted one-electron two-proton transfer processes in models inspired by the Tyr-His couple of photosystem II. *ACS Cent. Sci.* **2017,** *3* (5), 372-380.

14. Soudackov, A. V.; Hazra, A.; Hammes-Schiffer, S., Multidimensional treatment of stochastic solvent dynamics in photoinduced proton-coupled electron transfer processes: Sequential, concerted, and complex branching mechanisms. *J. Chem. Phys.* **2011,** *135* (14), 144115.

15. Goyal, P.; Hammes-Schiffer, S., Role of solvent dynamics in photoinduced proton-coupled electron transfer in a phenol–amine complex in solution. *J. Phys. Chem. Lett.* **2015,** *6* (18), 3515-3520.

16. Goyal, P.; Hammes-Schiffer, S., Tuning the ultrafast dynamics of photoinduced proton-coupled electron transfer in energy conversion processes. *ACS Energy Lett.* **2017,** *2* (2), 512-519.

17. Rose, M. J.; Gray, H. B.; Winkler, J. R., Hydrogen generation catalyzed by fluorinated diglyoxime-iron complexes at low overpotentials. *J. Am. Chem. Soc.* **2012,** *134*, 8310-8313.

18. Harshan, A. K.; Solis, B. H.; Winkler, J. R.; Gray, H. B.; Hammes-Schiffer, S., Computational study of fluorinated diglyoxime-iron complexes: Tuning the electrocatalytic pathways for hydrogen evolution. *Inorg. Chem.* **2016,** *55* (6), 2934-2940.

19. Chen, J. Y.; Dang, L.; Liang, H.; Bi, W.; Gerken, J. B.; Jin, S.; Alp, E. E.; Stahl, S. S., Operando analysis of NiFe and Fe oxyhydroxide electrocatalysts for water oxidation: Detection of Fe^{4+} by Mossbauer spectroscopy. *J. Am. Chem. Soc* **2015,** *137* (48), 15090-3.

20. Goldsmith, Z. K.; Harshan, A. K.; Gerken, J. B.; Vörös, M.; Galli, G.; Stahl, S. S.; Hammes-Schiffer, S., Characterization of NiFe oxyhydroxide electrocatalysts by integrated electronic structure calculations and spectroelectrochemistry. *Proc. Natl. Acad. Sci. U.S.A.* **2017,** *114* (12), 3050-3055.

21. Landau, L. D., LD Landau, Phys. Z. Sowjetunion 2, 46 (1932). *Phys. Z. Sowjetunion* **1932,** *2*, 46.

22. Zener, C., Non-adiabatic crossing of energy levels. *Proc. R. Soc. London, Ser. A* **1932,** *137*, 696.

23. Baughcum, S. L.; Smith, Z.; Wilson, E. B.; Duerst, R. W., Microwave spectroscopic study of malonaldehyde. 3. Vibration-rotation interaction and one-dimensional model for proton tunneling. *Journal of the American Chemical Society* **1984,** *106* (8), 2260-2265.

24. Harshan, A. K.; Yu, T.; Soudackov, A. V.; Hammes-Schiffer, S., Dependence of vibronic coupling on molecular geometry and environment: Bridging hydrogen atom transfer and electron–proton transfer. *J. Am. Chem. Soc* **2015,** *137* (42), 13545-13555.

25. Lovley, D. R.; Coates, J. D.; Blunt-Harris, E. L.; Phillips, E. J.; Woodward, J. C., Humic substances as electron acceptors for microbial respiration. *Nature* **1996,** *382* (6590), 445.

26. Moore, G. A.; Rossi, L.; Nicotera, P.; Orrenius, S.; O'Brien, P. J., Quinone toxicity in hepatocytes: studies on mitochondrial Ca^{2+} release induced by benzoquinone derivatives. *Arch. Biochem. Biophys.* **1987,** *259* (2), 283-295.

27. Lahtinen, R.; Fermın, D. J.; Kontturi, K.; Girault, H. H., Artificial photosynthesis at liquid-liquid interfaces: photoreduction of benzoquinone by water soluble porphyrin species. *J. Electroanal. Chem* **2000,** *483* (1-2), 81-87.

28. Soudackov, A.; Hammes-Schiffer, S., Derivation of rate expressions for nonadiabatic proton-coupled electron transfer reactions in solution. *J. Chem. Phys.* **2000,** *113* (6), 2385-2396.

29. Soudackov, A.; Hatcher, E.; Hammes-Schiffer, S., Quantum and dynamical effects of proton donor-acceptor vibrational motion in nonadiabatic proton-coupled electron transfer reactions. *J. Chem. Phys.* **2005,** *122* (1), 014505.

CHAPTER 2: Computational Study of Fluorinated Diglyoxime-Iron Complexes: Tuning the Electrocatalytic Pathways for Hydrogen[§]

2.1. Introduction

The design of molecular electrocatalysts with first-row transition metals is important for developing sustainable energy sources.[1-10] In an effort toward the design of more effective solar cells, a wide variety of molecular electrocatalysts based on cobalt,[11-29] nickel,[30-37] or iron[38-48] have been proposed for the production of molecular hydrogen. We and others have shown that cobalt diglyoxime electrocatalysts evolve molecular hydrogen with relatively high turnover frequencies and moderate overpotentials.[13-14, 16-18, 20, 22, 29] These cobalt catalysts also have been studied in depth by theoretical methods.[22, 24-25, 28] Importantly, two iron analogs of these cobalt glyoximes, depicted in Figure 2.1, have been found to evolve hydrogen at similarly moderate overpotentials in dichloromethane.[49] These two complexes, $[(\mathrm{dAr^FgBF_2})_2\mathrm{Fe(py)_2}]$ and $[(\mathrm{dAr^Fg_2H\text{-}BF_2})\mathrm{Fe(py)_2}]$ [$\mathrm{dAr^Fg}$ = bis(pentafluorophenyl-glyoximato), py = pyridine], exhibit turnover frequencies of 20 s^{-1} at −0.9 V vs SCE and 200 s^{-1} at −0.8 V vs SCE, respectively. These species are denoted **A** and **B**, respectively, and differ only in that one BF_2 bridge is replaced by a proton bridge (O-H-O) in **B**.

The experimental cyclic voltammograms (CVs) for both Fe-glyoxime complexes are depicted in Figure 2.2 for different concentrations of trifluoroacetic acid (TFA). The catalytic waves are identified by an increase in peak current with increasing TFA

[§] Reproduced with permission from:
Harshan, A. K.; Solis, B. H.; Winkler, J. R.; Gray, H. B.; Hammes-Schiffer, S., *Inorg. Chem.* **2016,** *55* (6), 2934-2940. Copyright 2016 American Chemical Society

concentration, thereby implying the formation of a catalytically active Fe-hydride intermediate. As shown in Figure 2.2, the CVs for these two complexes are qualitatively different: only the more negative peak is catalytic for **A**, but both peaks are catalytic for **B**. This observation suggests that a catalytically active Fe-hydride is formed after both reduction steps for **B** but only after the second reduction (i.e., at the more negative peak) for **A**. This qualitative difference in the CVs may arise from ligand protonation at the O-H-O bridge in **B**, which could allow additional pathways for hydrogen evolution.[8, 28, 50] In this chapter, we use computational tools to investigate the mechanisms for these two complexes in order to shed light on the qualitative differences between the CVs. Specifically, we use density functional theory (DFT) to calculate the relative reduction potentials and pK_a's for species that participate in steps along the possible catalytic cycles and to identify the thermodynamically favorable pathways. Subsequently, based on the simulation of CVs for both electrocatalysts, we confirm that the hypothesized mechanisms are consistent with the experimental data.

2.2. Computational Methods

The methods used for computing reduction potentials and pK_a's from the calculated free energy differences are discussed in detail elsewhere.[51] The DFT calculations reported here were performed using the BP86 functional[52-53] with the 6-31+G(d,p) basis set[54] for the central part of the molecule and the smaller 6-31G basis set for the axial pyridine ligands and the peripheral pentafluorophenyl rings. Benchmarking with different functionals is given in the Supporting Information (Appendix A). The BP86 functional, which provides physically reasonable spin densities with minimal spin contamination, affords structures and reduction potentials that are consistent with available experimental values. Solvation effects for the dichloromethane solvent were described with the conductor-like polarizable continuum model (C-PCM)[55-56] using Bondi radii,[57] including non-electrostatic interactions resulting from dispersion,[58] repulsion,[59] and cavity formation.[60] All calculations were performed using the Gaussian09 package.[61]

The geometry optimizations were performed for complexes in the gas phase. The neutral species were also optimized in dichloromethane, but the presence of solvent did not cause significant changes in the geometry (Table A.1). The free energy differences of reduction or deprotonation in dichloromethane were calculated using a Born-Haber thermodynamic cycle, in which the gas phase free energies included zero-point energy and entropic effects, and the solvation free energies were calculated for the gas-phase optimized geometries. These free energy differences were converted to relative reduction potentials and pK_a's using reference reactions.[24, 51, 62] All reduction potentials were calculated relative to the experimentally determined $E_{1/2}$ = –0.94 V vs SCE for **A**, corresponding to the $[\mathrm{Fe^{I}py}]^{-}/[\mathrm{Fe^{0}py}]^{2-}$ reduction. The pK_a's were calculated relative to the pK_a of $[\mathrm{Fe^{I}py}\ldots\mathbf{H}]^{0}$ for **B** because the mechanistic analysis below suggests that the pK_a of this species is similar to that of TFA.

2.3. Results and Discussion

Selected bond lengths and angles of the experimental crystal structures are compared with those of the calculated gas-phase optimized structures for A and B in Table 2.1. Overall, the calculated geometries agree well with the crystal structures, with deviations less than 0.1 Å for bond lengths and less than 1.5° for the angles probed. The intermediates formed by addition of a proton were also examined computationally. Protonation of the O-H-O bridge (i.e., ligand protonation) is denoted as Fe…H, in contrast to protonation at the Fe center, which is denoted as FeH. High-spin structures were also investigated, but the low-spin structures were more thermodynamically stable for all intermediates studied (Table A.2) except $[\mathrm{Fe^{II}py}]^0$ for **A** and **B** and the ligand protonated $[\mathrm{Fe^{II}py\ldots H}]^+$ for **B**.

According to X-ray crystal structures,[49] the neutral $\mathrm{Fe^{II}}$ complexes have a distorted octahedral geometry with two axial pyridine ligands. Moreover, experimental ^{1}H and ^{19}F NMR spectra of **A** and **B** in $\mathrm{CDCl_3}$ or $\mathrm{CD_3CN}$ contained peaks consistent with diamagnetic species, indicating that the resting state of both complexes is a low-spin (singlet) state.[49] The irreversibility of the less negative CV wave associated with reduction of the metal complex is thought to arise from pyridine ligand dissociation, as well as the effects of pyridine diffusion and possibly pyridinium formation in the presence of acid. Furthermore, DFT calculations of pyridine ligand binding free energies indicate that the singly reduced species is more stable with one bound pyridine ligand than with two bound pyridine ligands (Table A.3). According to the DFT calculations, **A** and **B** have square pyramidal geometries with a single pyridine ligand in both the $\mathrm{Fe^I}$ and $\mathrm{Fe^0}$ states, consistent with a reversible CV peak.

The possible mechanisms for hydrogen evolution by **A** are depicted in Figure 2.3. The first reduction step associated with the peak at E_p = –0.71 V vs SCE in dichloromethane corresponds to the $[\mathrm{Fe^{II}py_2}]^0/[\mathrm{Fe^{I}py}]^-$ couple. The DFT calculations indicate that reduction of $[\mathrm{Fe^{II}py_2}]^0$ generates a species with a spin density of only –0.07 on the Fe center and 1.04 on the glyoxime ligands (i.e., summed over all atoms except Fe and the two pyridines), suggesting ligand non-innocence (Table A.2) In other words, the unpaired electron is localized on the glyoxime ligands rather than the Fe center. Thus, this reduction can be represented by $[\mathrm{Fe}^{\mathrm{II}}\mathrm{py}_2]^0/[\mathrm{Fe}^{\mathrm{II}}(\mathrm{gly})^{\bullet}\mathrm{py}_2]^{-}$, where gly represents the glyoxime ligands bound to the Fe center. Although these ligands are present in all structures, the "$(\mathrm{gly})^{\bullet}$" notation is only used when an unpaired electron on the glyoxime ligands is suggested by the calculated spin density. The estimated pyridine ligand binding free energies given in Table A.3 indicate that $[\mathrm{Fe}^{\mathrm{II}}(\mathrm{gly})^{\bullet}\mathrm{py}_2]^{-}$ undergoes rapid loss of pyridine with an equilibrium constant of $K_{\mathrm{eq}} \sim 10^7$ to form $[\mathrm{Fe}^{\mathrm{I}}\mathrm{py}]^{-}$. Pyridine dissociation occurs in conjunction with an intramolecular electron transfer from the glyoxime ligands to the iron center, which has a resulting spin density of 1.08 (Table A.2). This reduced complex, $[\mathrm{Fe}^{\mathrm{I}}\mathrm{py}]^{-}$, could be reduced again or could be protonated to form an $[\mathrm{Fe}^{\mathrm{III}}\mathrm{Hpy}]^0$ intermediate, followed by reduction to $[\mathrm{Fe}^{\mathrm{II}}\mathrm{Hpy}]^{-}$. Hydrogen evolution directly from the $[\mathrm{Fe}^{\mathrm{III}}\mathrm{Hpy}]^0$ intermediate can be ruled out because the experimental CV shown in Figure 2.2 indicates that the first reduction (i.e., the less negative peak) is not catalytic.

To identify the source of catalytic activity at $E_{1/2} = -0.94$ V vs SCE, we calculated the relative pK_a's of $[\mathrm{Fe}^{\mathrm{III}}\mathbf{H}\mathrm{py}]^0$ and $[\mathrm{Fe}^{\mathrm{II}}\mathbf{H}\mathrm{py}]^{-}$ for **A**, where the bold **H** denotes the proton removed in the deprotonation reaction. These relative pK_a values are depicted in Figure 2.4. The pK_a of $[\mathrm{Fe}^{\mathrm{II}}\mathbf{H}\mathrm{py}]^{-}$ is 19 units higher than that of $[\mathrm{Fe}^{\mathrm{III}}\mathbf{H}\mathrm{py}]^0$, indicating that protonation of $[\mathrm{Fe}^{\mathrm{I}}\mathrm{py}]^{-}$ to produce $[\mathrm{Fe}^{\mathrm{III}}\mathrm{Hpy}]^0$ is much less thermodynamically favorable than protonation of $[\mathrm{Fe}^{0}\mathrm{py}]^{2-}$ to produce $[\mathrm{Fe}^{\mathrm{II}}\mathrm{Hpy}]^{-}$. For this reason, the pathway to the $[\mathrm{Fe}^{\mathrm{III}}\mathrm{Hpy}]^0$ intermediate is unlikely (marked by a red "X" in Figure 2.3), and the system is presumed to follow the pathway through the $[\mathrm{Fe}^{0}\mathrm{py}]^{2-}$ intermediate. According to these calculations, the catalytic peak at $E_{1/2} = -0.94$ V vs SCE corresponds to the reduction of $[\mathrm{Fe}^{\mathrm{I}}\mathrm{py}]^{-}$ to $[\mathrm{Fe}^{0}\mathrm{py}]^{2-}$, followed by protonation of the Fe center to form

$[Fe^{II}Hpy]^{-}$, which then evolves molecular hydrogen in acidic solution. This proposed mechanism for **A** is consistent with the experimental CV, as the peak at E_p = –0.71 V vs SCE is not catalytic, whereas the peak at $E_{1/2}$ = –0.94 V vs SCE is catalytic.

The mechanism of hydrogen evolution by **B** is more complicated, owing to the possibility of ligand protonation at the O-H-O bridge, as illustrated by the possible pathways for **B** depicted in Figure 2.5. As for **A**, the first reduction step associated with the peak at E_p = –0.93 V vs SCE corresponds to the $[Fe^{II}py_2]^0/[Fe^{I}py]^{-}$ couple. As discussed above for **A**, the immediate product of the first reduction is the ligand-reduced species $[Fe^{II}(gly)^{\bullet}py_2]^{-}$, which has a spin density of 0.06 on the Fe center, followed by rapid pyridine ligand loss and intramolecular electron transfer to form $[Fe^{I}py]^{-}$ (Tables A.2 and A.3). The $[Fe^{I}py]^{-}$ intermediate could be reduced again, or it could be protonated at either the Fe center or the O-H-O bridge. Each of these intermediates also could follow multiple pathways, as illustrated in Figure 2.5. As shown in Figure 2.2, both peaks in the CV were found to be catalytic for **B**. Previously the first catalytic peak (i.e., the less negative peak) was proposed to be associated with protonation of the $[Fe^{I}py]^{-}$ intermediate to form a catalytically active $[Fe^{III}Hpy]^0$ intermediate.[49] However, our calculations suggest an alternative mechanistic interpretation of the experimental CVs.

To determine the assignments for the two peaks in the experimental CV, we calculated reduction potentials for the various possible reduction steps. The $[Fe^{II}py_2]^0/[Fe^{II}(gly)^{\bullet}py_2]^{-}$ reduction occurs at the CV peak with E_p = –0.93 V vs SCE, which was calculated as E^{o} = –0.92 V vs SCE, in good agreement with the experimental value. As discussed above, this reduction is followed by rapid pyridine ligand loss and intramolecular electron transfer, affording $[Fe^{I}py]^{-}$. As given in Table 2.2, the calculations imply that the peak at $E_{1/2} = -1.16$ V vs SCE corresponds to the reduction of $[\mathrm{Fe^{I}py}]^{-}$ to $[\mathrm{Fe^{0}py}]^{2-}$, analogous to **A**. To determine which other reduction steps might occur at the more negative catalytic peak, we calculated the reduction potentials for the other three steps labeled in Figure 2.5. The corresponding reduction potentials reported in Table 2.2 are significantly less negative than the calculated $E_{1/2} = -1.17$ V vs SCE for the $[\mathrm{Fe^{I}py}]^{-}/[\mathrm{Fe^{0}py}]^{2-}$ couple.

To identify the catalytic mechanisms associated with both peaks, we calculated the relative pK_a's of the possible intermediates (see Figure 2.4). The horizontal dotted line in Figure 2.4 indicates the pK_a of **A** $[\mathrm{Fe^{III}}\mathbf{H}\mathrm{py}]^{0}$, which was determined from the above analysis to be unprotonated under the relevant experimental conditions. Thus, all complexes below the dotted line in Figure 2.4 are assumed to remain unprotonated under those conditions, and ligand protonation is thermodynamically unfavorable for $[\mathrm{Fe^{II}py_2}]^{0}$. Figure 2.4 also indicates that protonation of the Fe center of $[\mathrm{Fe^{I}py}]^{-}$ to generate $[\mathrm{Fe^{III}Hpy}]^{0}$ (circled in green) is less thermodynamically favorable than ligand protonation of $[\mathrm{Fe^{I}py}]^{-}$ to generate $[\mathrm{Fe^{I}py\ldots H}]^{0}$ (circled in red). In particular, the free energy of $[\mathrm{Fe^{I}py\ldots H}]^{0}$ is 5.19 kcal/mol lower than that of $[\mathrm{Fe^{III}Hpy}]^{0}$. Finally, protonation of $[\mathrm{Fe^{I}py\ldots H}]^{0}$ at the Fe center to produce $[\mathrm{Fe^{III}Hpy\ldots H}]^{+}$ (circled in blue) is thermodynamically unfavorable because the pK_a is below the dotted line in Figure 2.4.

Mechanistic proposals based on these results are depicted in Figure 2.6. Black numbers denote the reduction potentials, red numbers indicate free energy differences for intramolecular proton transfer, and blue numbers indicate pK_a values relative to $[\mathrm{Fe^{I}}$ $\mathrm{py\ldots}\mathbf{H}]^{0}$. Ligand protonation associated with this reference is presumed to occur under these experimental conditions because of the anodic shift of the first CV peak upon addition of TFA. Thus, we assume that the ligand protonation reaction is an equilibrium step, as indicated by the double arrows in Figure 2.6. We also assume non-negligible populations of both protonated and unprotonated species, thereby leading to the two different reaction pathways corresponding to the two catalytic peaks in the experimental CV. Thus, the pK_a of $[\mathrm{Fe^{I}py\ldots}\mathbf{H}]^0$, which is assigned to zero, is presumed to be similar to the pK_a of TFA, and the protonation reactions associated with more negative pK_a values are expected to be thermodynamically unfavorable.

The proposed mechanism associated with the first catalytic peak is shown in light red in Figure 2.6. The first step involves reduction from $[\mathrm{Fe^{II}py_2}]^0$ to $[\mathrm{Fe^{II}(gly)^{\bullet}py_2}]^-$ at $E^{\circ} = -0.92$ V vs SCE, followed by rapid loss of an axial pyridine ligand and intramolecular electron transfer to form $[\mathrm{Fe^{I}py}]^-$. In the presence of TFA, $[\mathrm{Fe^{I}py}]^-$ undergoes ligand protonation to produce $[\mathrm{Fe^{I}py\ldots H}]^0$, which reduces spontaneously to $[\mathrm{Fe^{0}py\ldots H}]^-$ because the calculated standard reduction potential for this couple is -0.45 V vs SCE, a value less negative than that of the first catalytic peak. Intramolecular proton transfer (IPT) from the ligand to the $\mathrm{Fe^0}$ center within the $[\mathrm{Fe^{0}py\ldots H}]^-$ complex is thermodynamically favorable by 4.22 kcal/mol, producing $[\mathrm{Fe^{II}Hpy}]^-$, which subsequently evolves hydrogen. Figure 2.7 depicts the optimized structures for $[\mathrm{Fe^{0}py\ldots H}]^-$ and $[\mathrm{Fe^{II}Hpy}]^-$, illustrating the position of the proton before and after the possible IPT step. Alternatively, protonation of the metal center of $[\mathrm{Fe^{0}py\ldots H}]^-$ by acid to produce $[\mathrm{Fe^{II}Hpy\ldots H}]^0$ would enable hydrogen evolution via either self-elimination or further reaction with acid. This metal protonation by TFA is predicted to be thermodynamically possible on the basis of the calculated relative pK_a values. A kinetics analysis would be required to determine the relative probabilities of the two branches depicted in the later part of the light red pathway in Figure 2.6, but both branches result in an Fe^{II}-hydride species. Note that protonation of $[Fe^{I}py]^{-}$ at the Fe center to generate $[Fe^{III}Hpy]^{0}$ (shown in gray in Figure 2.6) is thermodynamically less favorable than protonation of this species at the ligand by 5.19 kcal/mol and therefore is unlikely to occur.

The proposed mechanism associated with the second catalytic peak is shown in light blue in Figure 2.6. Again the first step involves reduction from $[Fe^{II}py_2]^{0}$ to $[Fe^{II}(gly)^{\bullet}py_2]^{-}$ at $E^{o} = -0.92$ V vs SCE, followed by rapid axial pyridine ligand loss and intramolecular electron transfer to produce $[Fe^{I}py]^{-}$. Then $[Fe^{I}py]^{-}$ is reduced to $[Fe^{0}py]^{2-}$ at $E^{o} = -1.17$ V vs SCE, and protonation of the Fe center produces $[Fe^{II}Hpy]^{-}$, which subsequently evolves hydrogen. Note that protonation of $[Fe^{0}py]^{2-}$ at the Fe center is thermodynamically more favorable than protonation of this species at the ligand by 4.22 kcal/mol, but ligand protonation of $[Fe^{0}py]^{2-}$ to form $[Fe^{0}py...H]^{-}$ could occur as a minor pathway. Moreover, $[Fe^{II}Hpy]^{-}$ could possibly undergo ligand protonation to produce $[Fe^{II}Hpy\ldots H]^{0}$, which likely would evolve hydrogen via either self-elimination or reaction with acid. This ligand protonation of $[Fe^{II}Hpy]^{-}$ by TFA is predicted to be possible on the basis of the calculated relative pK_a values, although it may be slightly thermodynamically unfavorable.

To test the proposed mechanisms for **A** and **B**, we simulated the CVs with parameters that are consistent with the proposed mechanisms and compared them to experimental data. As shown in Table 2.2, the calculated reduction potential for the less negative peak of **A** is shifted positively relative to the experimental value. This discrepancy may be due to limitations in the DFT methodology, or it could arise from an inadequate treatment of the subsequent rapid pyridine loss, although **B** does not exhibit this discrepancy. As a result, the CV simulations for **A** utilized the experimental $E_{1/2}$ and E_p for these two reduction potentials, whereas the CV simulations for **B** utilized only the calculated standard reduction potentials for all couples. For **B**, we used the calculated reduction potentials, pK_a's, and IPT reaction free energies to estimate initial values for the various parameters. All of the reduction potentials, the equilibrium constant for pyridine dissociation from $[\mathrm{Fe^{II}py_2}]^0$, and the equilibrium constant for IPT between $[\mathrm{Fe^{I}py\ldots H}]^0$ and $[\mathrm{Fe^{III}Hpy}]^0$ were fixed to the values calculated with DFT, but the other parameters were refined to reproduce the experimental CVs. The equilibrium constants obtained by this fitting procedure are in agreement with the qualitative trends of the calculated pK_a values. All parameters used in the CV simulations are given in Tables A.8 and A.9.

The simulated CVs shown in Figure 2.8 are in qualitative agreement with the experimental CVs in Figure 2.2. For **A**, the magnitude and position of the first peak are insensitive to acid concentration, while the current associated with the second peak increases with increasing acid concentration. For the CV simulations of **B**, the positions of both peaks are in good agreement with those observed in the experimental CVs. Moreover, as in the experimental CVs, the current associated with both peaks increases with increasing acid concentration, and the second peak is greater for low acid concentrations while the first peak is greater for higher acid concentrations. Note that the CV simulations did not reproduce the experimentally observed slight anodic shift of the less negative peak for **B**, suggesting that additional processes may be involved under experimental conditions.

2.4. Conclusions

Our calculations provide evidence for catalytic pathways involving an Fe^0 intermediate that is protonated to generate an active Fe^{II}-hydride species. In **A**, the pathway involves two consecutive reduction steps from Fe^{II} to Fe^0, followed by protonation to generate the active Fe^{II}-hydride species. This mechanism is consistent with experimental CVs in which hydrogen production occurs only at the more negative peak, which is associated with the second reduction step. In **B**, two catalytic pathways can proceed in parallel due to protonation of the O-H-O bridge (i.e., the ligand) after reduction from Fe^{II} to Fe^I. If the pK_a of the ligand of the Fe^I species is similar to that of TFA, two parallel pathways are likely, as both protonated and unprotonated ligand populations will be present. The first pathway is associated with a ligand-protonated Fe^I species, which is spontaneously reduced to a ligand-protonated Fe^0 complex, followed by intramolecular proton transfer from the ligand to the metal center to generate the active Fe^{II}-hydride. This pathway results in catalysis at the less negative peak in the experimental CVs because the second reduction occurs at a potential less negative than the potential associated with this peak. The second pathway is identical with that described for **A** and results in catalysis at the peak associated with the second reduction step. The first pathway arises because of ligand protonation, which leads to a less negative reduction potential, but both pathways involve an Fe^0 intermediate that is protonated to form an active Fe^{II}-hydride.

CV simulations based on these proposed mechanisms reproduce the qualitative features of the experimental CVs. The parallel mechanisms proposed for **B** could be investigated further by varying the pK_a of the acid. According to theoretical predictions, acids with higher pK_a values will reduce the degree of ligand protonation, favoring catalysis at the more negative peak, whereas acids with lower pK_a values will enhance the degree of ligand protonation, favoring catalysis at the less negative peak. We suggest that these findings could be exploited in experiments where solution conditions would turn off one of the catalytic pathways. Similar tuning of the two pathways could be accomplished by varying the substituents on the ligands, possibly even favoring a third pathway involving an active $\mathrm{Fe^{III}}$-hydride instead of an $\mathrm{Fe^{II}}$-hydride. The ability to tune the catalytic pathways through acid strength or substituents on the ligand is important for designing more effective catalysts for energy conversion processes.

2.5. Figures

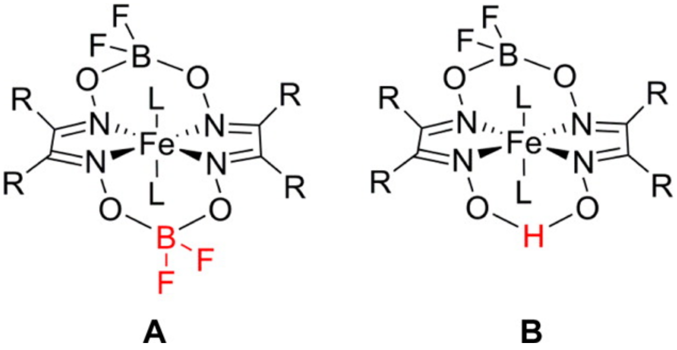

Figure 2.1. Fe-glyoxime electrocatalysts **A** = [(dAr^{F}gBF$_2$)$_2$Fe(py)$_2$] and **B** = [(dAr^{F}g$_2$H BF$_2$)Fe(py)$_2$], where L=pyridine and R=C_6F_5. Copyright 2016 American Chemical Society.

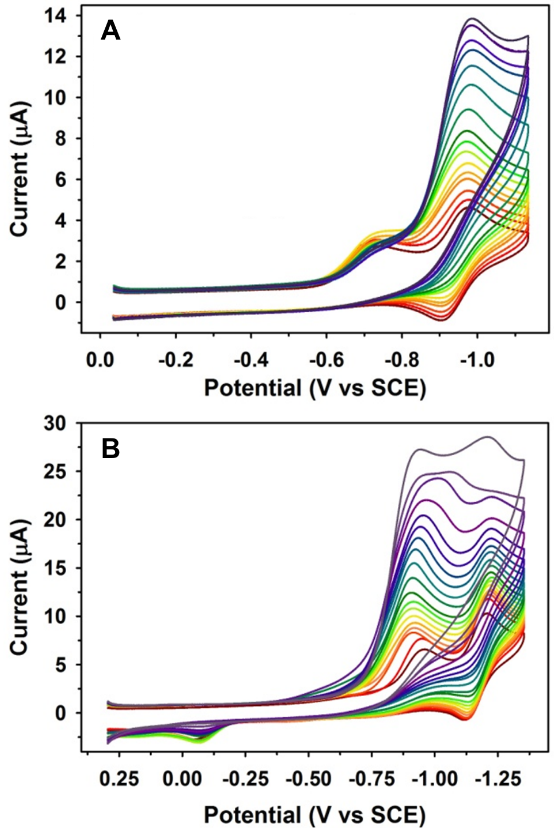

Figure 2.2. Experimental CVs at 100 mV/s for 0.5 mM: **A** and **B** in dichloromethane with TFA added in increasing concentrations from red (0 mM) to purple (50 mM for A, 170 mM for B). Adapted with permission from Ref [49]. Copyright 2012 American Chemical Society.

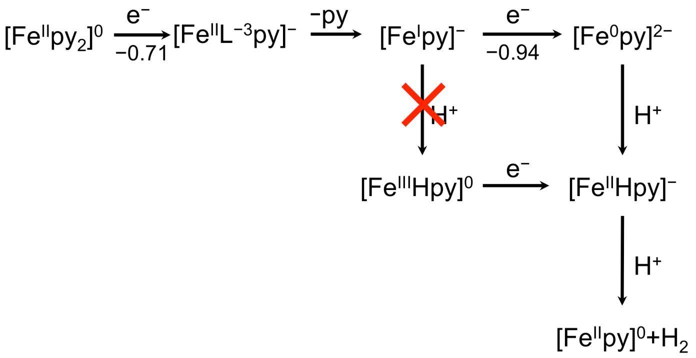

Figure 2.3. Possible mechanism for generating active metal-hydride species for **A**. The numbers under reduction steps correspond to E_p or $E_{1/2}$ in V vs SCE from the experimental CV in dichloromethane. As discussed in the text, the first step also involves pyridine ligand loss. Hydrogen evolution from $[\mathrm{Fe^{III}Hpy}]^0$ is ruled out on the basis of the experimental CV, which indicates that the less negative peak is not catalytic. The red X indicates a thermodynamically unfavorable protonation at the $\mathrm{Fe^I}$ center, as determined from DFT calculations. Copyright 2016 American Chemical Society.

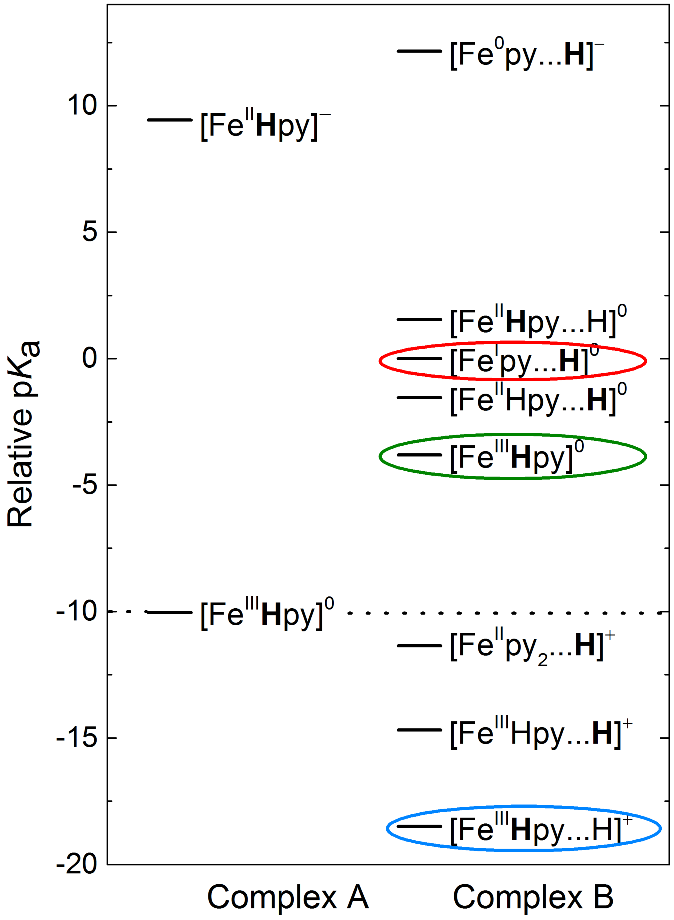

Figure 2.4. Calculated relative pK_a values for **A** (left) and **B** (right). Ligand protonation is denoted by …H, and metal protonation is denoted by a metal hydride, FeH. The bold **H** indicates the acidic proton removed in the calculations. All pK_a values are calculated relative to the pK_a of **B** [Fe^{I}py…**H**]^0, which is assigned a value of zero because the mechanistic analysis suggests that the pK_a of this species is similar to that of TFA. The dotted line is drawn at the pK_a of **A** [Fe^{III}**H**py]^0 because experiments indicate that this species is not protonated in the presence of TFA; thus, species with pK_a's below the dotted line are assumed to be unprotonated. The numerical values associated with this figure are provided in Table A.5. Copyright 2016 American Chemical Society.

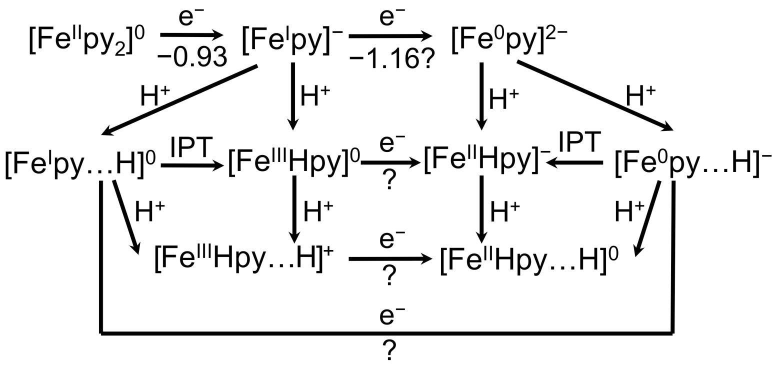

Figure 2.5. Possible mechanisms for generating active metal-hydride species for **B**. The numbers under reduction steps correspond to E_p or $E_{1/2}$ in V vs SCE from the experimental CV in dichloromethane. As discussed in the text, the first step also involves pyridine ligand loss. The question marks indicate reduction steps that could possibly occur at one of the experimentally observed peaks. IPT denotes intramolecular proton transfer. Copyright 2016 American Chemical Society.

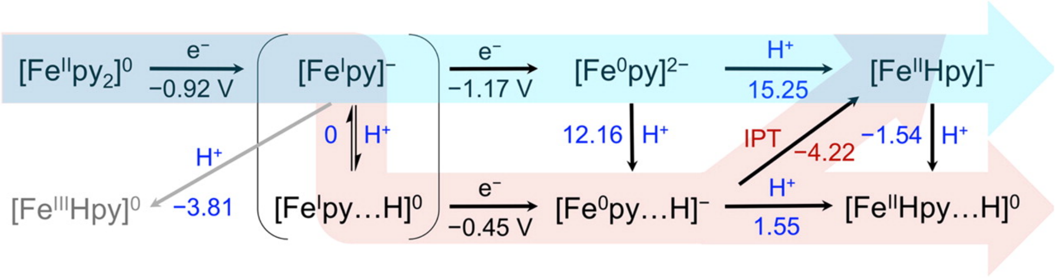

Figure 2.6. Proposed mechanisms for **B**. Black numbers indicate calculated standard reduction potentials vs SCE, red numbers indicate calculated free energies in kcal/mol, and blue numbers indicate pK_a's calculated relative to the pK_a of [Fe^{I}py…**H**]^0. As discussed in the text, the first step also involves pyridine ligand loss. The light red catalytic pathway is associated with the less negative peak, and the blue catalytic pathway is associated with the more negative peak in the experimental CVs depicted in Figure 2.2. Protonation of [Fe^{I}py]$^−$ at the Fe center to generate [Fe^{III}Hpy]^0 is thermodynamically less favorable than protonation of [Fe^{I}py]$^−$ at the ligand to generate [Fe^{I}py…H]^0 by 5.19 kcal/mol and therefore is unlikely to occur. The later part of the light red pathway could proceed via two possible branches, IPT or metal protonation: the IPT step is predicted to be thermodynamically favorable by −4.22 kcal/mol, and the pK_a associated with metal protonation is predicted to be in the vicinity of the pK_a of TFA. The last species in the blue pathway, [Fe^{II}Hpy]$^−$, could possibly undergo ligand protonation by TFA to produce [Fe^{II}Hpy…H]^0 according to the calculated relative pK_a. All pathways involve an active Fe^{II}-hydride intermediate. Copyright 2016 American Chemical Society.

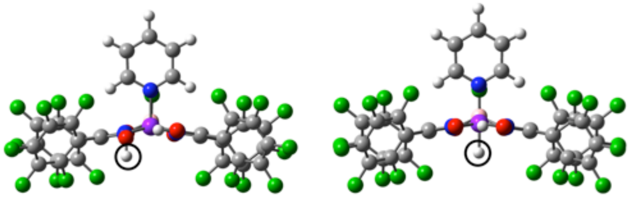

Figure 2.7. Optimized structures for $[Fe^{0}py\ldots H]^{-}$ and $[Fe^{II}Hpy]^{-}$ for **B**, illustrating the location of the proton before and after the IPT step shown in the light red mechanism of Figure 2.6. The proton may not be oriented ideally for the IPT step in these optimized geometries, but thermal fluctuations could provide flexibility for reorientation, or alternatively a water molecule could serve as a bridge. Copyright 2016 American Chemical Society.

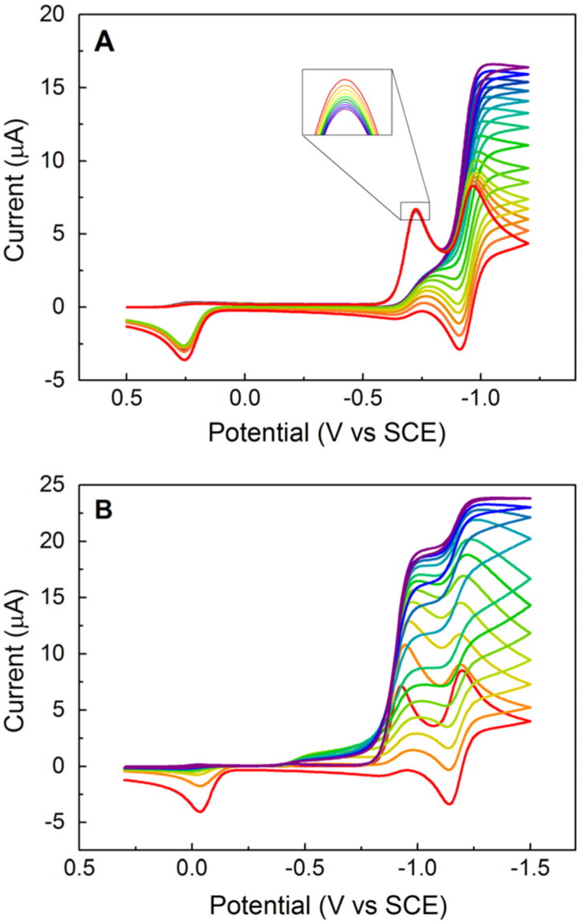

Figure 2.8. Simulated CVs at 100 mV/s for 0.5 mM **A** and **B** assuming the hydrogen evolution mechanisms depicted in Figures 2.3 and 2.6. Color gradation from red to blue indicates increasing acid concentration as TFA is added, ranging from 0.0 to 10 mM. The parameters used in the CV simulations of **A** and **B** are in Tables A.8 and A.9, respectively. Copyright 2016 American Chemical Society.

2.6. Tables

Table 2.1. Calculated bond lengths (angstroms) and angles (degrees)

	A		**B**	
Parameter	Expt. [a]	Calc.	Expt. [a]	Calc.
Fe-py(1)	2.03	2.00	2.00	2.00
Fe-py(2)	2.02	2.03	2.04	2.02
Fe-N(1)	1.89	1.88	1.88	1.89
Fe-N(2)	1.89	1.88	1.88	1.89
Fe-N(3)	1.88	1.89	1.88	1.89
Fe-N(4)	1.88	1.89	1.88	1.90
N(1)-Fe-N(2)	98.8	96.8	96.9	96.8
N(2)-Fe-N(3)	82.5	82.0	82.4	82.2
N(3)-Fe-N(4)	96.9	97.1	97.3	97.6
N(4)-Fe-N(1)	81.5	82.8	82.9	83.1
N(3)-N(4)-N(1)-Fe	−2.7	−3.3	−3.5	−2.6

[a] Ref [49].

Table 2.2. Calculated reduction potentials [a]

Complex	Ox	S_{ox}	Red	S_{red}	E^{o} (V)
A	$[\mathrm{Fe^{II}py_2}]^0$	0	$[\mathrm{Fe^{II}(gly)^{\bullet}py_2}]^-$	1/2	–0.62 (–0.71) [b]
	$[\mathrm{Fe^{II}py}]^0$	1	$[\mathrm{Fe^{I}py}]^-$	1/2	+0.29
	$[\mathrm{Fe^{I}py}]^-$	1/2	$[\mathrm{Fe^{0}py}]^{2-}$	0	*–0.94* (–0.94) [d]
	$[\mathrm{Fe^{III}Hpy}]^0$	1/2	$[\mathrm{Fe^{II}Hpy}]^-$	0	+0.21
B	$[\mathrm{Fe^{II}py_2}]^0$	0	$[\mathrm{Fe^{II}(gly)^{\bullet}py_2}]^-$	1/2	–0.92 (–0.93) [b]
	$[\mathrm{Fe^{II}py}]^0$	1	$[\mathrm{Fe^{I}py}]^-$	1/2	–0.05 (–0.06) [e]
	$[\mathrm{Fe^{I}py}]^-$	1/2	$[\mathrm{Fe^{0}py}]^{2-}$	0	–1.17 (–1.16) [c]
	$[\mathrm{Fe^{III}Hpy}]^0$	1/2	$[\mathrm{Fe^{II}Hpy}]^-$	0	–0.04
	$[\mathrm{Fe^{II}py\ldots H}]^+$	1	$[\mathrm{Fe^{I}py\ldots H}]^0$	1/2	+0.73
	$[\mathrm{Fe^{I}py\ldots H}]^0$	1/2	$[\mathrm{Fe^{0}py\ldots H}]^-$	0	–0.45
	$[\mathrm{Fe^{III}Hpy\ldots H}]^+$	1/2	$[\mathrm{Fe^{II}Hpy\ldots H}]^0$	0	+0.74

[a] Values given in volts vs SCE in dichloromethane. Experimental values are given in parentheses.

[b] Experimental value is E_{p} of the irreversible cathodic wave.

[c] Experimental value is $E_{1/2}$.

[d] The experimentally measured $E_{1/2}$ for the $[\mathrm{Fe^{I}py}]^-/[\mathrm{Fe^{0}py}]^{2-}$ couple of **A** was used as the reference for all values in this table and agrees by construction for this entry.

[e] Experimental value is E_{p} of the irreversible anodic wave.

2.7. References

1. Lewis, N. S.; Nocera, D. G., Powering the planet: Chemical challenges in solar energy utilization. *Proc. Natl. Acad. Sci. U.S.A.* **2006,** *103* (43), 15729-15735.
2. Savéant, J.-M., Molecular catalysis of electrochemical reactions. Mechanistic aspects. *Chem. Rev.* **2008,** *108* (7), 2348-2378.
3. Gust, D. M., T. A.; Moore, A. L., Solar fuels via artificial photosynthesis. *Acc. Chem. Res.* **2009,** *42*, 1890-1898.
4. Walter, M. G.; Warren, E. L.; McKone, J. R.; Boettcher, S. W.; Mi, Q.; Santori, E. A.; Lewis, N. S., Solar water splitting cells. *Chem. Rev.* **2010,** *110* (11), 6446-6473.
5. Du, P.; Eisenberg, R., Catalysts made of earth-abundant elements (Co, Ni, Fe) for water splitting: Recent progress and future challenges. *Energy Environ. Sci.* **2012,** *5*, 6012-6021.
6. Eckenhoff, W. T.; Eisenberg, R., Molecular systems for light driven hydrogen production. *Dalton Trans.* **2012,** *41*, 13004-13021.
7. DuBois, D. L., Development of molecular electrocatalysts for energy storage. *Inorg. Chem.* **2014,** *53*, 3935-39360.
8. Kaeffer, N.; Chavarot-Kerlidou, M.; Artero, V., Hydrogen evolution catalyzed by cobalt diimine-dioxime complexes. *Acc. Chem. Res.* **2015,** *48*, 1286-1295.
9. Queyriaux, N.; Jane, R. T.; Massin, J.; Artero, V.; Chavarot-Kerlidou, M., Recent developments in hydrogen evolving molecular cobalt (II)–polypyridyl catalysts. *Coord. Chem. Rev.* **2015**.
10. Siewert, I., Proton-coupled electron transfer reactions catalysed by 3*d* metal complexes. *Chem. Eur. J.* **2015,** *21* (43), 15078-15091.
11. Gjerde, H. B.; Espenson, J. H., Concurrent and competitive homolysis and elimination reactions of (α-phenylethyl)aquacobaloxime. *Organometallics* **1982,** *1*, 435-440.
12. Connolly, P.; Espenson, J. H., Cobalt-catalyzed evolution of molecular hydrogen. *Inorg. Chem.* **1986,** *25*, 2684-2688.
13. Razavet, M.; Artero, V.; Fontecave, M., Proton electroreduction catalyzed by cobaloximes: Functional models for hydrogenases. *Inorg. Chem.* **2005,** *44*, 4786-4795.
14. Hu, X.; Cossairt, B. M.; Brunschwig, B. S.; Lewis, N. S.; Peters, J. C., Electrocatalytic hydrogen evolution by cobalt difluoroboryl-diglyoximate complexes. *Chem. Commun.* **2005**, 4723-4725.
15. Pantani, O.; Anxolabéhère-Mallart, E.; Aukauloo, A.; Millet, P., Electroactivity of cobalt and nickel glyoximes with regard to the electro-reduction of protons into molecular hydrogen in acidic media. *Electrochem. Commun.* **2007,** *9*, 54-58.
16. Baffert, C.; Artero, V.; Fontecave, M., Cobaloximes as functional models for hydrogenases. 2. Proton electroreduction catalyzed by difluoroborylbis(dimethylgloximato)cobalt(II) complexes in organic media. *Inorg. Chem.* **2007,** *46*, 1817-1824.
17. Hu, X.; Brunschwig, B. S.; Peters, J. C., Electrocatalytic hydrogen evolution at low overpotentials by cobalt macrocyclic glyoxime and tatraimine complexes. *J. Am. Chem. Soc.* **2007,** *129*, 8988-8998.
18. Dempsey, J. L.; Brunschwig, B. S.; Winkler, J. R.; Gray, H. B., Hydrogen evolution catalyzed by cobaloximes. *Acc. Chem. Res.* **2009,** *42* (12), 1995-2004.

19. Jacques, P.-A.; Artero, V.; Pécaut, J.; Fontecave, M., Cobalt and nickel diimine-dioxime complexes as molecular electrocatalysts for hydrogen evolution with low overvoltages. *Proc. Natl. Acad. Sci. U.S.A.* **2009,** *106* (49), 20627-20632.

20. Dempsey, J. L.; Winkler, J. R.; Gray, H. B., Kinetics of electron transfer reactions of H_2-evolving cobalt diglyoxime catalysts. *J. Am. Chem. Soc.* **2010,** *132* (3), 1060-1065.

21. Berben, L. A.; Peters, J. C., Hydrogen evolution by cobalt tetraimine catalysts adsorbed on electrode surfaces. *Chem. Commun.* **2010,** *46* (3), 398-400.

22. Muckerman, J. T.; Fujita, E., Theoretical studies of the mechanism of catalytic hydrogen production by a cobaloxime. *Chem. Commun.* **2011,** *47*, 12456-12458.

23. McNamara, W. R.; Han, Z.; Alperin, P. J.; Brennessel, W. W.; Holland, P. L.; Eisenberg, R., A cobalt–dithiolene complex for the photocatalytic and electrocatalytic reduction of protons. *J. Am. Chem. Soc* **2011,** *133* (39), 15368-15371.

24. Solis, B. H.; Hammes-Schiffer, S., Theoretical analysis of mechanistic pathways for hydrogen evolution catalyzed by cobaloximes. *Inorg. Chem.* **2011,** *50*, 11252-11262.

25. Solis, B. H.; Hammes-Schiffer, S., Substitution effects on cobalt diglyoxime catalysts for hydrogen evolution. *J. Am. Chem. Soc.* **2011,** *133*, 19036-19039.

26. McNamara, W. R.; Han, Z.; Yin, C.-J. M.; Brennessel, W. W.; Holland, P. L.; Eisenberg, R., Cobalt-dithiolene complexes for the photocatalytic and electrocatalytic reduction of protons in aqueous solutions. *Proc. Natl. Acad. Sci. U.S.A.* **2012,** *109* (39), 15594-15599.

27. Solis, B. H.; Hammes-Schiffer, S., Computational study of anomalous reduction potentials for hydrogen evolution catalyzed by cobalt dithiolene complexes. *J. Am. Chem. Soc.* **2012,** *134* (37), 15253-15256.

28. Solis, B. H.; Yu, Y.; Hammes-Schiffer, S., Effects of ligand modification and protonation on metal oxime hydrogen evolution electrocatalysts. *Inorg. Chem.* **2013,** *52*, 6994-6999.

29. Wakerley, D. W.; Reisner, E., Development and understanding of cobaloxime activity through electrochemical molecular catalyst screening. *Phys. Chem. Chem. Phys.* **2014,** *16*, 5739-5746.

30. Yang, J. Y.; Chen, S.; Dougherty, W. G.; Kassel, W. S.; Bullock, R. M.; DuBois, D. L.; Raugei, S.; Rousseau, R.; Dupuis, M.; DuBois, M. R., Hydrogen oxidation catalysis by a nickel diphosphine complex with pendant tert-butyl amines. *Chem. Commun.* **2010,** *46* (45), 8618-8620.

31. Helm, M. L.; Stewart, M. P.; Bullock, R. M.; Rakowski DuBois, M.; DuBois, D. L., A synthetic nickel electrocatalyst with a turnover frequency above 100,000 s^{-1} for H_2 production. *Science* **2011,** *333* (6044), 863-866.

32. O'Hagen, M.; Shaw, W. J.; Raugei, S.; Chen, S.; Yang, J. Y.; Kilgore, U. J.; DuBois, D. L.; Bullock, R. M., Moving protons with pendant amines: Proton mobility in a nickel catalyst for oxidation of hydrogen. *J. Am. Chem. Soc.* **2011,** *133*, 14301-14312.

33. Horvath, S.; Fernandez, L. E.; Soudackov, A. V.; Hammes-Schiffer, S., Insights into proton-coupled electron transfer mechanisms of electrocatalytic H_2 oxidation and production. *Proc. Natl. Acad. Sci. U.S.A.* **2012,** *109* (30), 15663-15668.

34. Raugei, S.; Chen, S.; Ho, M.-H.; Ginovska-Pangovska, B.; Rousseau, R. J.; Dupuis, M.; DuBois, D. L.; Bullock, R. M., The role of pendant amines in the breaking and forming of molecular hydrogen catalyzed by nickel complexes. *Chem. Eur. J.* **2012,** *18*, 6493-6506.

35. Wiese, S.; Kilgore, U. J.; Ho, M.-H.; Raugei, S.; DuBois, D. L.; Bullock, R. M.; Helm, M. L., Hydrogen production using nickel electrocatalysts with pendant amines: Ligand effects on rates and overpotentials. *ACS Catal.* **2013,** *3*, 2527-2535.

36. Stewart, M. P.; Ho, M.-H.; Wiese, S.; Lindstrom, M. L.; Thogerson, C. E.; Raugei, S.; Bullock, R. M.; Helm, M. L., High catalytic rates for hydrogen production using nickel electrocatalysts with seven-membered cyclic diphosphine ligands containing one pendant amine. *J. Am. Chem. Soc.* **2013,** *135* (6033-6046).

37. Chen, S.; Ho, M.-H.; Bullock, R. M.; DuBois, D. L.; Dupuis, M.; Rousseau, R.; Raugei, S., Computing free energy landscapes: Application to Ni-based electrocatalysts with pendant amines for H_2 production and oxidation. *ACS Catal.* **2014,** *4*, 229-242.

38. Thompson, D. W.; Stynes, D. V., Synthesis, electrochemistry, and kinetic investigations of low-spin ferrous bis (difluoroboryl) bis (dioximate) complexes. *Inorg. Chem.* **1990,** *29* (19), 3815-3822.

39. Bhugun, I.; Lexa, D.; Savéant, J.-M., Homogeneous catalysis of electrochemical hydrogen evolution by iron(0) porphyrins. *J. Am. Chem. Soc.* **1996,** *118* (16), 3982-3983.

40. Darensbourg, M. Y.; Lyon, E. J.; Smee, J. J., The bio-organometallic chemistry of active site iron in hydrogenases. *Coord. Chem. Rev.* **2000,** *206*, 533-561.

41. Georgakaki, I. P.; Thomson, L. M.; Lyon, E. J.; Hall, M. B.; Darensbourg, M. Y., Fundamental properties of small molecule models of Fe-only hydrogenase: computations relative to the definition of an entatic state in the active site. *Coord. Chem. Rev.* **2003,** *238*, 255-266.

42. Tye, J. W.; Darensbourg, M. Y.; Hall, M. B., Correlation between computed gas-phase and experimentally determined solution-phase infrared spectra: Models of the iron-iron hydrogenase enzyme active site. *J. Comput. Chem.* **2006,** *27* (12), 1454-1462.

43. Felton, G. A. N.; Glass, R. S.; Lichtenberger, D. L.; Evans, D. H., Iron-only hydrogenase mimics. Thermodynamic aspects of the use of electrochemistry to evaluate catalytic efficiency for hydrogen generation. *Inorg. Chem.* **2006,** *45* (23), 9181-9184.

44. Olsen, M. T.; Justice, A. K.; Gloaguen, F.; Rauchfuss, T. B.; Wilson, S. R., New nitrosyl derivatives of diiron dithiolates related to the active site of the [FeFe]-hydrogenases. *Inorg. Chem.* **2008,** *47* (24), 11816-11824.

45. Felton, G. A.; Mebi, C. A.; Petro, B. J.; Vannucci, A. K.; Evans, D. H.; Glass, R. S.; Lichtenberger, D. L., Review of electrochemical studies of complexes containing the Fe_2S_2 core characteristic of [FeFe]-hydrogenases including catalysis by these complexes of the reduction of acids to form dihydrogen. *J. Organomet. Chem.* **2009,** *694* (17), 2681-2699.

46. Tard, C.; Pickett, C. J., Structural and functional analogues of the active sites of the [Fe]-, [NiFe]-, and [FeFe]-hydrogenases. *Chem. Rev.* **2009,** *109* (6), 2245-2274.

47. Kaur-Ghumaan, S. S., L.; Lomoth, R.; Stein, M.; Ott, S. , Catalytic hydrogen evolution from mononuclear iron(II) carbonyl complexes as minimal functional models of the [FeFe] hydrogenase active site. *Angew. Chem. Int. Ed.* **2010,** *49*, 8033–8036.

48. Royer, A. M.; Salomone-Stagni, M.; Rauchfuss, T. B.; Meyer-Klaucke, W., Iron acyl thiolato carbonyls: structural models for the active site of the [Fe]-hydrogenase (Hmd). *J. Am. Chem. Soc.* **2010,** *132* (47), 16997-17003.

49. Rose, M. J.; Gray, H. B.; Winkler, J. R., Hydrogen generation catalyzed by fluorinated diglyoxime-iron complexes at low overpotentials. *J. Am. Chem. Soc.* **2012,** *134*, 8310-8313.

50. Wang, J.; Li, C.; Zhou, Q.; Wang, W.; Hou, Y.; Zhang, B.; Wang, X., Enhanced photocatalytic hydrogen production by introducing the carboxylic acid group into cobaloxime catalysts. *Dalton Trans.* **2015,** *44* (40), 17704-17711.

51. Solis, B. H.; Hammes-Schiffer, S., Proton-coupled electron transfer in molecular electrocatalysis: Theoretical methods and design principles. *Inorg. Chem.* **2014,** *53* (13), 6427-6443.

52. Perdew, J. P., Density-functional approximation for the correlation energy of the inhomogeneous electron gas. *Phys. Rev. B* **1986,** *33* (12), 8822-8824.

53. Becke, A. D., Density-functional exchange-energy approximation with correct asymptotic-behavior. *Phys. Rev. A* **1988,** *38*, 3098-3100.

54. Hehre, W. J.; Ditchfield, R.; Pople, J. A., Self-consistent molecular orbital methods. XII. Further extensions of gaussian-type basis sets for use in molecular orbital studies of organic molecules. *J. Chem. Phys.* **1972,** *56* (5), 2257-2261.

55. Barone, V.; Cossi, M., Quantum calculation of molecular energies and energy gradients in solution by a conductor solvent model. *J. Phys. Chem. A* **1998,** *102*, 1995-2001.

56. Cossi, M.; Rega, N.; Scalmani, G.; Barone, V., Energies, structures, and electronic properties of molecules in solution with the C-PCM solvation model. *J. Comput. Chem.* **2003,** *24* (6), 669-681.

57. Bondi, A., van der Waals volume and radii. *J. Phys. Chem.* **1964,** *68* (3), 441.

58. Floris, F.; Tomasi, J., Evaluation of the dispersion contribution to the solvation energy - a simple computational model in the continuum approximation. *J. Comput. Chem.* **1989,** *10* (5), 616-627.

59. Floris, F. M.; Tomasi, J.; Ahuir, J. L. P., Dispersion and repulsion contributions to the solvation energy: Refinements to a simple computational model in the continuum approximation. *J. Comput. Chem.* **1991,** *12* (7), 784-791.

60. Pierotti, R. A., A scaled particle theory of aqueous and nonaqueous solutions. *Chem. Rev.* **1976,** *76* (6), 717-726.

61. Frisch, M. J.; Trucks, G. W.; Schlegel, H. B.; Scuseria, G. E.; Robb, M. A.; Cheeseman, J. R.; Scalmani, G.; Barone, V.; Mennucci, B.; Petersson, G. A.; Nakatsuji, H.; Caricato, M.; Li, X.; Hratchian, H. P.; Izmaylov, A. F.; Bloino, J.; Zheng, G.; Sonnenberg, J. L.; Hada, M.; Ehara, M.; Toyota, K.; Fukuda, R.; Hasegawa, J.; Ishida, M.; Nakajima, T.; Honda, Y.; Kitao, O.; Nakai, H.; Vreven, T.; J. A. Montgomery, J.; Peralta, J. E.; Ogliaro, F.; Bearpark, M.; Heyd, J. J.; Brothers, E.; Kudin, K. N.; Staroverov, V. N.; Kobayashi, R.; Normand, J.; Raghavachari, K.; Rendell, A.; Burant, J. C.; Iyengar, S. S.; Tomasi, J.; Cossi, M.; Rega, N.; Millam, J. M.; Klene, M.; Knox, J. E.; Cross, J. B.; Bakken, V.; Adamo, C.; Jaramillo, J.; Gomperts, R.; Stratmann, R. E.; Yazyev, O.; Austin, A. J.; Cammi, R.; Pomelli, C.; Ochterski, J. W.; Martin, R. L.; Morokuma, K.; Zakrzewski, V. G.; Voth, G. A.; Salvador, P.; Dannenberg, J. J.; Dapprich, S.; Daniels, A. D.; Farkas, Ö.; Foresman, J. B.; Ortiz, J. V.; Cioslowski, J.; Fox, D. J. *Gaussian 09, Revision C.1*, Gaussian, Inc.: Wallingford CT, 2009.

62. Qi, X.-J.; Fu, Y.; Liu, L.; Guo, Q.-X., Ab initio calculations of thermodynamic hydricities of transition-metal hydrides in acetonitrile. *Organometallics* **2007,** *26*, 4197-4203.

CHAPTER 3: Characterization of NiFe oxyhydroxide Electrocatalysts by Integrated Electronic Structure Calculations and Spectroelectrochemistry[§]

3.1. Introduction

The photoelectrochemical conversion of water into O_2 and H_2 is a major focus of energy storage and conversion efforts,[1-4] with significant attention directed toward development of efficient catalysts for water oxidation and reduction. Such catalysts should operate at low overpotential, exhibit high selectivity, and be composed of earth-abundant materials. Commercial electrolyzers typically use transition-metal-oxide electrocatalysts for the oxygen evolution reaction (OER),[5-6] and nickel, nickel-iron, and other mixed-metal oxides are especially effective under alkaline conditions.[7-8] In spite of the importance and potential future impact of these materials, many features of their catalytic mechanism are poorly understood.

Nickel oxyhydroxide has long been associated with OER electrocatalysis;[9-10] however, much of the activity in this material has been shown to arise from the presence of Fe impurities.[7, 11] This conclusion complements extensive independent studies demonstrating the effectiveness of NiFe-based oxide and oxyhydroxide materials as OER electrocatalysts,[12-14] including a survey of nearly 3500 mixed-metal-oxide compositions, which drew attention to the high electrocatalytic activity of materials containing Ni, Fe, and a third metal (e.g., Ba, Sr, Ca, or Cr).[15] Such observations account for the extensive interest in understanding the

---

[§] Reproduced with permission from:
Goldsmith, Z. K.; Harshan, A. K.; Gerken, J. B.; Vörös, M.; Galli, G.; Stahl, S. S.; Hammes-Schiffer, S. *Proc. Natl. Acad. Sci. U.S.A.* **2017,** *114* (12), 3050-3055.
Copyright 2017 National Academy of Sciences

structural and mechanistic principles underlying the high activity of Ni/Fe-based electrocatalysts.

A recent combined experimental and computational study investigated Ni-, Fe-, and various NiFe-oxyhydroxide-based electrocatalysts in an effort to probe the redox behavior and electrocatalytic mechanism of these catalysts.[16] Operando X-ray absorption spectroscopy and density functional theory calculations with the Hubbard *U* correction (DFT+*U*) implicated the presence of Fe^{3+} sites within NiFe oxyhydroxide as the active site for O–O bond formation.[17] The formation or catalytic role of Fe^{4+} or other high-valent Fe species was disfavored based on the experimental and computational data. A subsequent operando Mössbauer spectroscopic study, however, showed that significant quantities of Fe^{4+} are generated in NiFe-oxyhydroxide catalysts during electrocatalytic water oxidation,[18] and the accessibility of Fe^{4+} was supported by an independent computational study of such materials.[19] These different, and sometimes conflicting, observations highlight the need for an improved understanding of complex materials of this type, ideally drawing upon synergistic contributions from experimental and computational approaches.

Herein, we report a theoretical and spectroelectrochemical study of Ni and 25% Fe-doped Ni oxyhydroxide electrocatalysts. Cyclic voltammetry and hybrid DFT calculations were used to determine the redox potentials for proton-coupled oxidation of the film and assign relevant metal oxidation states at different applied potentials, including those contributing to catalytic water oxidation. The optoelectronic properties of the pure Ni and Fe-doped catalysts obtained from experiment and computation provide an atomistic description of the dominant states at the valence and conduction band edges. Collectively, the results offer unprecedented insights into the influence of iron dopants on the redox properties and electronic structure of Ni oxyhydroxide electrocatalysts.

3.2. Materials and Methods

All calculations were carried out using planewave based density functional theory (DFT) with Quantum-ESPRESSO.[20] Core electrons were described using recently developed optimally tuned norm-conserving psuedopotentials.[21-22] A planewave cutoff energy of 80 Ry was used in describing the wavefunctions in all calculations, and the Brillouin zone was sampled using a 4×4 k-point Monkhorst-Pack grid for the in-slab dimensions. All geometry optimizations were carried out using the PBE functional[23] with Hubbard *U* corrections[17, 24] of 6.6 eV and 3.5 eV for Ni and Fe, respectively. We adopted Hubbard *U* values from the literature, where they were computed using linear response theory.[25] However, there are several means of choosing the optimal value of *U*, and it has been shown that, for example, different oxidation states of the same transition metal ion may favor different optimal *U* values.[26-27]

Thus, to ensure the robustness of our results, we also performed single point energy calculations with the global hybrid functional PBE0.[28-29] A similar strategy was used by Zaffran and Toroker recently.[30] The use of PBE0 is further motivated by recent calculations suggesting that the mixing fraction of exact exchange in global hybrid functionals should be chosen to be the inverse of the dielectric constant.[31-33] The high-frequency dielectric constant was computed to be ~3.5 for bulk $Ni(OH)_2$,[34] suggesting a fraction of exact exchange of 0.29, comparable to of the fraction of 0.25 for PBE0. More importantly, as shown below, PBE0 is necessary to open a band gap for many of the active catalyst redox states. Furthermore, we also find that PBE0 gives redox potentials that are in better agreement with experiments than those computed at the PBE+*U* level of theory. To reduce the computational cost of the PBE0 calculations, we optimized the geometries at the PBE+*U* level of theory and only performed single-point PBE0 calculations. Test calculations relaxing $Ni_4O_8H_n$ slabs at the PBE0 level of theory indicated that the PBE+*U* and PBE0 geometries differ by only 0.05 Å for metal--O bonds and 0.01 Å for O--H bonds, as shown in Table B.1.

A single layer of NiFe oxyhydroxide was used in each of the computations as electronically representative of the real system, as shown in Figure 3.1. The layer-layer interactions do not qualitatively affect the electronic structure (Figure B.1), and *in situ* the layers are intercalated by solvent and ions, further attenuating interactions between layers.[35] The unit cell for the Ni-only systems contained 4 Ni, 8 O, and 0-8 H. In the doped systems, one of the Ni sites was replaced by Fe (25% doping), and an analogous series of H stoichiometries were studied.

3.3. Results and Discussion

3.3.1. Electrochemical behavior of NiFe oxyhydroxide in situ

The present study focuses on a comparison of pure Ni and 25% Fe-doped Ni oxyhydroxide electrocatalysts. In order to perform experimental studies, thin films of $Ni(OH)_2$ or Fe-doped $Ni(OH)_2$ were prepared via electrodeposition, as elaborated in the Supporting Information (Appendix B). Cyclic voltammograms (CVs) of the resulting materials reveal differences in voltammetric responses (Figure 3.1), consistent with previous observations.[7, 11-12, 36-37] The pure Ni material exhibits an isolated $Ni^{2+/3+}$ redox feature in the CV, with a midpoint potential of 0.53 V vs. NHE, and a small redox feature (peak potential ~0.76 V) at the foot of the large irreversible wave corresponding to the catalytic OER, which has an onset potential of ~0.72 V. Introduction of iron into the oxide is known to increase the $Ni^{2+/3+}$ potential and decrease the onset potential for catalysis.[7, 11-12, 36-37] With the 25% Fe-doped material, the two features are fully merged, and only a small shoulder is evident at the foot of the catalytic wave.

The NiFe oxyhydroxide unit cell used in the calculations is depicted in Figure 3.2 and is representative of two-dimensional, periodic, single layers of the oxyhydroxide material separated by vacuum. The interlayer hydrogen-bonding interactions, which have been explored previously,[38] do not qualitatively change the electronic structure properties of interest herein (cf. Fig. B.1). Solvent molecules and ions, which are known to intercalate between layers of the film, should further attenuate layer-layer interactions[35] and have only a minor influence on the electronic structure of the material. The system with 25% Fe-doping was modeled by replacing one Ni site in the unit cell with Fe. Geometries of different redox and protonation states of the layers were optimized at the DFT+*U* level of theory,[17, 24] followed by a single point energy calculation with the hybrid functional PBE0[28-29] (see Appendix B for details). The proton-coupled oxidation, or net dehydrogenation, of the oxyhydroxide materials was modeled by systematically removing H atoms from the layers. The Ni-only materials studied herein are denoted $Ni_4O_8H_n$, where $n = 0 – 8$. Representative examples for $n = 8$ and 0 correspond to $Ni(OH)_2$ and NiO_2, respectively. Similarly, the different redox and protonation states of the 25% Fe-doped materials are denoted $Ni_3Fe_1O_8H_n$ ($n = 0 – 8$). At each value of *n,* the lowest-energy hydrogen configuration found was used in our analyses. The experimentally studied materials have a mixture of hydrogen configurations and Fe site positions that may lead to heterogeneities in oxidation and spin states that are not accessible via periodic calculations based on a small unit cell.

The computed proton-coupled redox potentials for the various reactions are given in Table 3.1. All of the reported potentials in Table 3.1 are calculated relative to the experimentally determined $Ni^{2+/3+}$ potential for the Ni-only $Ni_4O_8H_n$ system (i.e., $n = 8$ to 4) because only the computed relative potentials are expected to be quantitatively reliable. Specifically, the redox potentials are calculated from the expression

$$E^{\mathrm{o}} = -\frac{\Delta U^{\mathrm{o}}}{nF} + \frac{\Delta U^{\mathrm{o}}_{\mathrm{ref}}}{n'F} + E^{\mathrm{o}}_{\mathrm{ref}} = -\frac{\Delta U^{\mathrm{o}}}{nF} + E_{\mathrm{corr}} \tag{3-1}$$

where F is the Faraday constant, ΔU^{o} is the electronic energy change associated with $\mathrm{MO}_x\mathrm{H}_{y-n} \rightarrow \mathrm{MO}_x\mathrm{H}_y$ (the reaction of interest), $\Delta U^{\mathrm{o}}_{\mathrm{ref}}$ is the electronic energy change associated with $\mathrm{MO}_x\mathrm{H}_{y'-n'} \rightarrow \mathrm{MO}_x\mathrm{H}_{y'}$ (the reference reaction), and $E^{\mathrm{o}}_{\mathrm{ref}}$ is the experimentally determined reduction potential for the reference reaction. The correction factor $E_{\mathrm{corr}} = E^{\mathrm{o}}_{\mathrm{ref}} + \frac{\Delta U^{\mathrm{o}}_{\mathrm{ref}}}{n'F}$ is the difference between the experimental and calculated reduction potentials for the reference reaction. This procedure is based on a thermodynamic scheme that eliminates the energy of the H_2 molecules and ensures cancellation of the majority of the translational, rotational, and vibrational entropic contributions. More details about this procedure are provided in Appendix B. The aqueous solvent environment and displacement of protons by intercalated cations are not considered explicitly but are assumed to exert an approximately similar effect on all species. As a result, these effects approximately cancel in the referencing scheme, which involves the calculation of only relative potentials. Recent data suggest that solvated ions could have a kinetic influence,[39-40] but kinetic issues are not addressed in these calculations.

Our results indicate the importance of utilizing hybrid functionals for these types of systems. The relative redox potentials obtained from PBE+U calculations are systematically lower than those obtained from both PBE0 calculations and the CV experiments (see Table B.4). The PBE+*U* method, as implemented with a single value of *U* for each metal, does not provide reliable redox thermodynamic properties for this material, most likely because multiple oxidation states of the same metals are present.[26-27, 38, 41] Although computationally expensive, the use of the hybrid PBE0 functional avoids the parameterization necessary for the quantitatively reliable implementation of the PBE+*U* method for this type of system. The use of PBE0 is further motivated by recent calculations suggesting that the mixing fraction of exact exchange in global hybrid functionals should be chosen to be the inverse of the dielectric constant.[31-33] The high-frequency dielectric constant was computed to be ~3.5 for bulk $Ni(OH)_2$,[34] suggesting a fraction of exact exchange of 0.29, comparable to of the fraction of 0.25 for PBE0.

The two redox processes observed experimentally in the Ni-only oxyhydroxide material (Figure 3.1, black trace) are consistent with the computed potentials in Table 3.1. The quasi-reversible feature in the experimental CV centered at 0.53 V vs. NHE is attributed to complete oxidation of Ni^{2+} to Ni^{3+}, corresponding to $4H^+/4e^-$ oxidation of the $Ni_4O_8H_8$ unit cell (i.e., one electron per nickel), leading to the reference of $8H \rightarrow 4H + 2\ H_2$ used in Table 3.1. However, literature data[42-43] also provide evidence that this feature could correspond to $6H^+/6e^-$ oxidation of the $Ni_4O_8H_8$ unit cell (i.e., 1.5 electrons per nickel), which would suggest a reference of $8H \rightarrow 2H + 3\ H_2$. Given this uncertainty, the proton-coupled redox potentials were also calculated with the reference reaction corresponding to $8H \rightarrow 2H + 3\ H_2$, as given in Table B.5. Because this different reference simply shifts all redox potentials downward by 0.06 V, the qualitative trends and conclusions do not change with the use of a different reference. It is further noted that these calculations provide only thermodynamic information and do not address kinetic complexity, such as that evident in the relatively large splitting between the anodic and cathodic peaks in the CV (cf. Figure 3.1). As indicated by Table 3.1, the proton-coupled oxidations of the layer corresponding to 8H → 6H + H_2 and 6H → 4H + H_2 are predicted to occur at nearly the same potential. The next redox event observed experimentally is the onset of catalytic current, together with the small redox feature at the foot of the wave. The computations suggest these features correlate with further oxidation of the film (4H → 2H + H_2), computed to occur at 0.73 V (Table 3.1).

Calculations on the $Ni_3Fe_1O_8H_n$ system predict that Fe will be in the Fe^{3+} state at open-circuit, corresponding to $n = 7$ (i.e., 7H). Specifically, the $Fe^{2+/3+}$ redox potential (8H → 7H + 0.5 H_2) was computed to be –0.72 V, which is lower than that accessible experimentally. The first (and only) experimentally observed redox event is associated with the onset of catalytic current (Figure 3.1, red trace), and the calculations suggest that multiple proton-coupled oxidations are viable at the observed potential. Accessible states range from $n = 6$ to $n = 2$, with calculated potentials spanning 0.52 to 0.63 V (cf. Table 3.1). The metal-ion oxidation states and electronic structure features of these catalyst states will be elaborated below.

3.3.2. Ni and Fe oxidation states upon proton-coupled oxidation

The determination of oxidation states is notoriously challenging, particularly in periodic calculations. We utilized the site-specific magnetizations, namely the difference in spin up and spin down densities localized on Ni and Fe, as signatures of different oxidation states. Magnetizations have also been used recently to analyze the three-dimensional periodic solid *b*-NiOOH.[19] While other quantitative methods for inferring integer metal oxidation states in the solid state have been developed,[44-45] the use of site-specific magnetizations provides a clear qualitative picture for this system. To validate this approach, we carried out additional calculations with maximally-localized Wannier functions[44] which provide results in agreement with those inferred from site-specific magnetizations (see Appendix B). Furthermore, as shown in Table B.6, the metal-oxygen bond lengths correlate with the computed formal oxidation states.

The following discussion presents a systematic analysis of the computed oxidation states as a function of the H stoichiometry and thereby connects them to the proton-coupled redox potentials described above. For Ni, the 2+, 3+, and 4+ oxidation states correspond to two, one, and zero unpaired electrons, respectively, localized on a given Ni atom. Fe oxidation states from 2+ to 5+ were observed in the studied range of H stoichiometries. The PBE0 calculations suggest that the ground state for each Fe species is high spin, in accordance with available experimental data for Fe^{3+}.[18] The calculations indicate that Fe^{4+} is also high spin, which has not been resolved experimentally, but may arise from constraints and environment imposed by the extended lattice. Mn^{3+}, which is isoelectronic to Fe^{4+}, in the analogous NiMn layered double hydroxide has been found to be high spin.[46] The computed magnetizations and corresponding oxidation states for each metal site in the unit cell of the periodic system are depicted in Figure 3.3. While NiO_2 and Fe^{5+}-containing systems were investigated computationally and are represented in Figure 3.3, neither is accessible under experimental conditions owing to their high potentials.

For the $Ni_4O_8H_n$ material shown in Figure 3.3a, sequential proton-coupled oxidations of the layer result in oxidations of the Ni sites from entirely Ni^{2+} in $Ni_4O_8H_8$ to entirely Ni^{4+} in $Ni_4O_8H_0$. In the intermediate case of $Ni_4O_8H_4$, there are four magnetically equivalent Ni^{3+} sites. In the systems defined by $n = 6$ and $n = 2$ (6H and 2H), a coexistence of different Ni oxidation states is observed. In $Ni_4O_8H_2$, which is expected to be catalytically active, magnetizations characteristic of Ni^{4+} and Ni^{3+} are observed for two sites each. As expected, the deprotonation of an oxygen is accompanied by oxidation of one of the metal centers bonded to that oxygen.

The same analysis of site-specific magnetizations for the Fe-doped systems is depicted in Figure 3.3b. As noted above, the open-circuit $Ni_3Fe_1O_8H_7$ state has three Ni^{2+} and one Fe^{3+} sites in the unit cell. Upon proton-coupled oxidation, Fe is oxidized to Fe^{4+} before any of the Ni^{2+} sites are oxidized. Furthermore, Fe^{4+} is observed in stoichiometries from n = 6 to n = 2 (6H to 2H), the same range of compositions that can be present under catalytic conditions based on the calculated redox potentials in Table 3.1.

This observation is in accordance with the operando Mössbauer spectroscopic identification of Fe^{4+}.[18] At the Fe-doped oxyhydroxide stoichiometry, $Ni_3Fe_1O_8H_4$, the Fe^{4+} site exists in conjunction with one Ni^{2+} site and two Ni^{3+} sites, in contrast to the uniformly 3+ oxidation states in the pure Ni oxyhydroxide. This observation indicates charge transfer occurring from Fe to Ni in the working catalyst, which is further elucidated in the electronic structure analysis below.

3.3.3. Optoelectronic properties of NiFe oxyhydroxide

Thin films of $Ni(OH)_2$ or Fe-doped $Ni(OH)_2$ were prepared on transparent FTO (fluorine-doped tin oxide) electrodes in order to analyze the catalyst via spectroelectrochemistry. UV-visible spectra were acquired while holding the catalyst-coated electrode at different applied potentials (Figure 3.4, see the Supporting Information for details). A prominent spectroscopic feature corresponding to the band edge absorption develops for both the Ni and NiFe catalysts upon increasing the potential (Figures. 3.4b and 3.4d). The absorption at 2.5 eV, depicted as a function of applied potential in Figures. 3.4a and 3.4c (filled circles; right y-axis), illustrates that the optical changes are directly correlated with the redox changes in the catalyst.

The pure Ni and Fe-doped materials exhibit qualitatively different optoelectronic behavior. For the $Ni(OH)_2$ material, the film darkens as NiOOH is formed, starting at ~0.53 V (Figure 3.4a, b), and then further darkens as the potential is raised to the onset of catalysis. Within the catalytic wave, the absorption spectrum is largely independent of potential. Although the calculations suggest that higher redox states should be accessible in the potential range evaluated, rapid water oxidation under these conditions will result in these states not having significant population and/or lifetime. In the 25% Fe-doped material, negligible absorbance changes are evident until the onset of OER activity, corresponding to the first redox feature evident in the CV (Fig. 4c, d). The band edge absorption energy is similar to that of the pure Ni film, beginning at 1.5 ± 0.1 eV. Once again, negligible absorbance changes are observed as the potential is increased into the catalytic wave because higher oxidation states of the catalyst are not attained, owing to rapid water oxidation from such states.[47] These observations, in combination with the computed metal-ion redox potentials described above, are consistent with the presence of significant quantities of Fe^{4+} in the steady-state catalyst.[18]

To understand the trends in the measured optical gaps, we compared experimental results to the computed fundamental band gaps for each film, as obtained from the differences of the eigenvalues of the valence band maximum (VBM) and the conduction band minimum (CBM) calculated with PBE0 for the pure Ni and Fe-doped systems (Table B.7). The band gaps computed with PBE+*U* are almost vanishing for the catalytically relevant states (Figs. B.2-B.3), and thus the use of the PBE0 functional is essential to reasonably describe these band gaps. Similar observations were reported for bulk Ni oxyhydroxides.[30, 38] The calculated band gaps of both the pure Ni and 25% Fe-doped systems decrease upon proton-coupled oxidation, as observed via spectroelectrochemistry. The observation that pure Ni and Fe-doped thin films have similar absorption onsets is consistent with the similarity in the computed band gaps for these two systems. The calculated fundamental gaps are on the order of ~1 eV higher than the corresponding optical gaps measured experimentally; however, this discrepancy is not unexpected as the computed values do not include the exciton binding energy, which for NiO is on the order of ~1 eV.[48]

3.3.4. Electronic structure of NiFe oxyhydroxide and the effects of Fe doping

To elucidate the effect of Fe in the doped oxyhydroxide system, we analyzed the electronic structure of both the Ni and NiFe materials around the Fermi level. The atomic projected density of states (PDOS) for two layered materials, $Ni_4O_8H_2$ and $Ni_3Fe_1O_8H_4$, are shown in Figs. 5a and 5e, respectively. Further breakdowns of the PDOS in Figure 3.5. (b-d, f-h) illustrate the electronic structure associated with specific metal atoms and oxidation states and differentiate between bridging hydroxide and oxide ligand states (i.e., states associated with protonated and deprotonated oxygen atoms).

In $Ni_4O_8H_2$, the Ni^{3+} electronic states at the valence band maximum (VBM) are closer to the Fermi level than are the Ni^{4+} states, and states associated with both Ni^{3+} and Ni^{4+} contribute to the conduction band minimum (CBM) (in Figure 3.5d). Additionally, oxide ligand states are more prevalent than hydroxide states in the CBM composition (Figure 3.5c). The PDOS plots associated with oxides bound to Ni atoms in different oxidation states are similar (Figure 3.5d). This similarity is not surprising given that in the figure O--Ni^{3+} refers to states associated with O atoms bound to two Ni^{3+} sites and one Ni^{4+} site, while O--Ni^{4+} refers to states associated with O atoms bound to two Ni^{4+} sites and one Ni^{3+} site.

The corresponding analysis of the Fe-doped Ni-oxyhydroxide ($Ni_3Fe_1O_8H_4$) reveals important differences. Figure 3.5f demonstrates that electronic states associated with Ni^{2+} dominate the VBM, while those associated with the dopant Fe^{4+} dominate the CBM. This Fe-to-Ni charge transfer character is evident in states comprising both the VBM and the CBM. As observed for the Ni-only catalyst, oxide ligand states are more prevalent than hydroxide states in the CBM (Figure 3.5g). The oxide states in the NiFe material, however, exhibit a distinct metal-coordination dependence. In Figure 3.5h, O--Ni refers to states of O atoms not bound to Fe, while O--Fe^{4+} refers to states of O atoms bound to one Fe site and two Ni sites. States associated with Fe^{4+}-ligated oxides are energetically lower than those associated with oxides ligated to only Ni and thus dominate the CBM.

3.4. Conclusions

We have used electronic structure methods and spectroelectrochemistry to characterize the pure Ni and Fe-doped oxyhydroxide OER electrocatalysts. In the Ni-only material, the onset of the OER catalytic current occurs at potentials that generate Ni^{4+}, whereas in the 25% Fe-doped system, a number of redox states, which all contain Fe^{4+}, are thermodynamically accessible at catalytic potentials. The observed dependence of the optical properties on the potential directly corresponds to these predicted changes in the redox states. The electronic structure of the Ni-only and Fe-doped materials reveals that the conduction band minimum is dominated by hybrid Ni-oxide states in the pure Ni system and by Fe-oxide states in the Fe-doped material.

These results have clear implications for the catalytic OER mechanism. For example, water oxidation is commonly proposed to involve nucleophilic attack of water on a high-valent metal oxide species, and the results described herein show that the NiOOH lattice enables facile oxidation of Fe^{3+} to Fe^{4+}. The oxidation to Fe^{4+} may be facilitated by the superior electronic conductivity of the mixed-metal system relative to pure Fe oxyhydroxides.[49-50] Catalytically active sites are likely to be present at edge, corner, or defect sites. Based on the electronic structure results obtained here for the bulk, it is reasonable to extrapolate that Fe-oxide motifs at such sites will exhibit electrophilicity suitable to mediate water oxidation. However, the metal oxidation and spin states at defect sites could differ from those at regular lattice sites. The present results provide an excellent foundation for future efforts to probe this hypothesis.

3.5. Figures

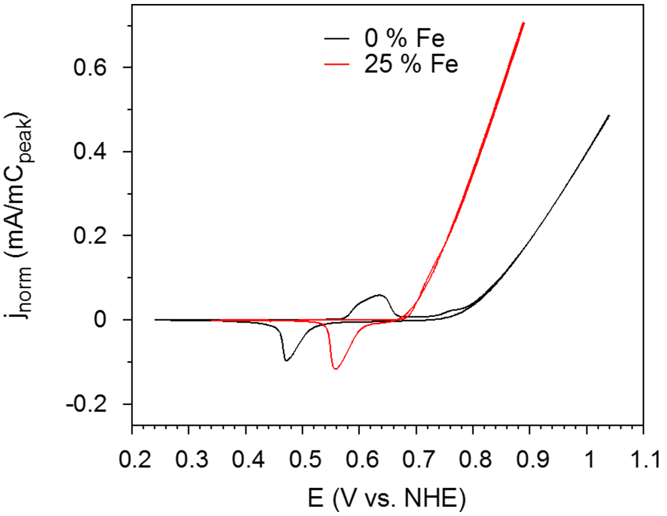

Figure 3.1. Cyclic voltammograms of $Ni_4O_8H_n$ (black trace) and $Ni_3Fe_1O_8H_n$ (red) films on FTO (fluorine-doped tin oxide) electrodes in 1 M KOH at 5 mV/s. Current densities are normalized to the peak area of the cathodic peak. Data for intermediate Fe loadings are given in Fig. B9. Copyright 2017 National Academy of Sciences.

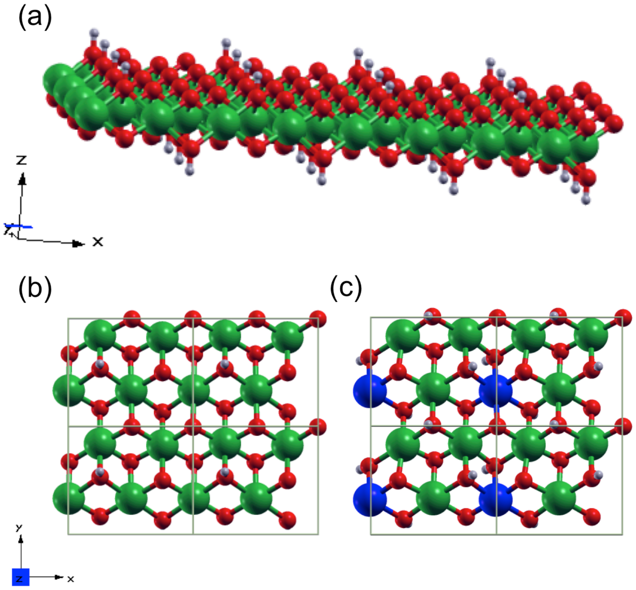

Figure 3.2. Single-layer NiFe oxyhydroxide, composed of Ni (green), O (red), H (gray), and Fe (blue) for (a) the undoped Ni oxyhydroxide, $Ni_4O_8H_2$ (side view); (b) viewed from above the surface; (c) the NiFe oxyhydroxide doped 25% with Fe, $Ni_3Fe_1O_8H_4$, viewed from above the surface. Parts (b) and (c) depict the unit cell that is periodically replicated in two dimensions for all calculations, with varying numbers of hydrogens. Copyright 2017 National Academy of Sciences.

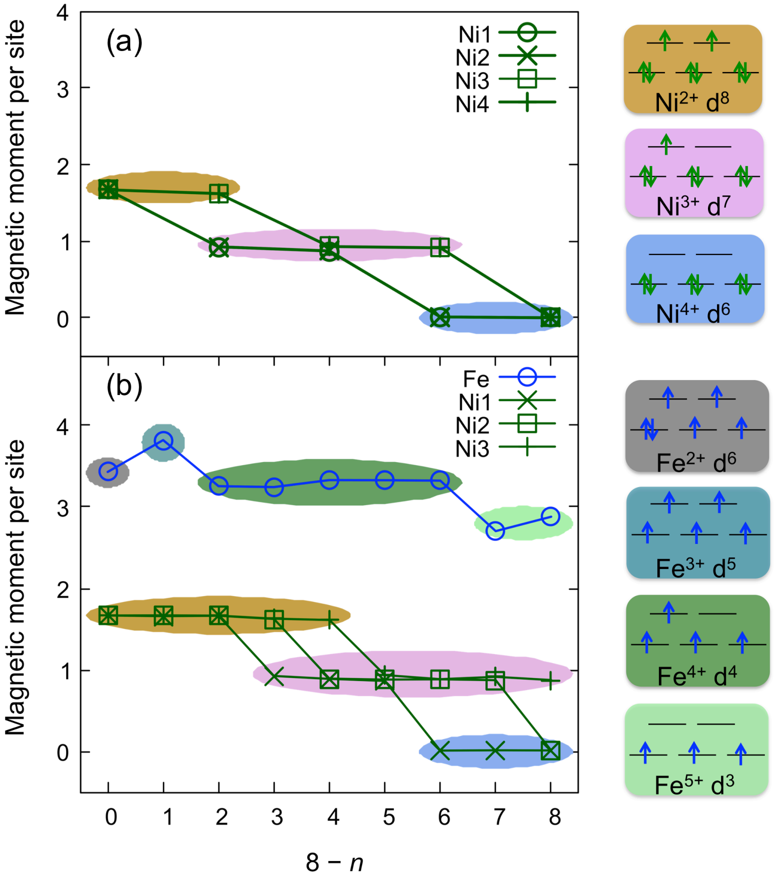

Figure 3.3. Calculated magnetic moments of each metal center in the unit cell vs. 8 − *n* for (a) pure $Ni_4O_8H_n$ and (b) Fe-doped $Ni_3Fe_1O_8H_n$. The radii over which the spin densities were integrated were determined by Quantum-ESPRESSO. Oxidation states of each metal center are color-coded as follows: Ni^{2+} (gold), Ni^{3+} (pink), Ni^{4+} (blue), Fe^{2+} (gray), Fe^{3+} (teal), Fe^{4+} (dark green), Fe^{5+} (light green). Accompanying electronic structure diagrams are idealized and neglect possible quasi-Jahn-Teller distortions. Copyright 2017 National Academy of Sciences.

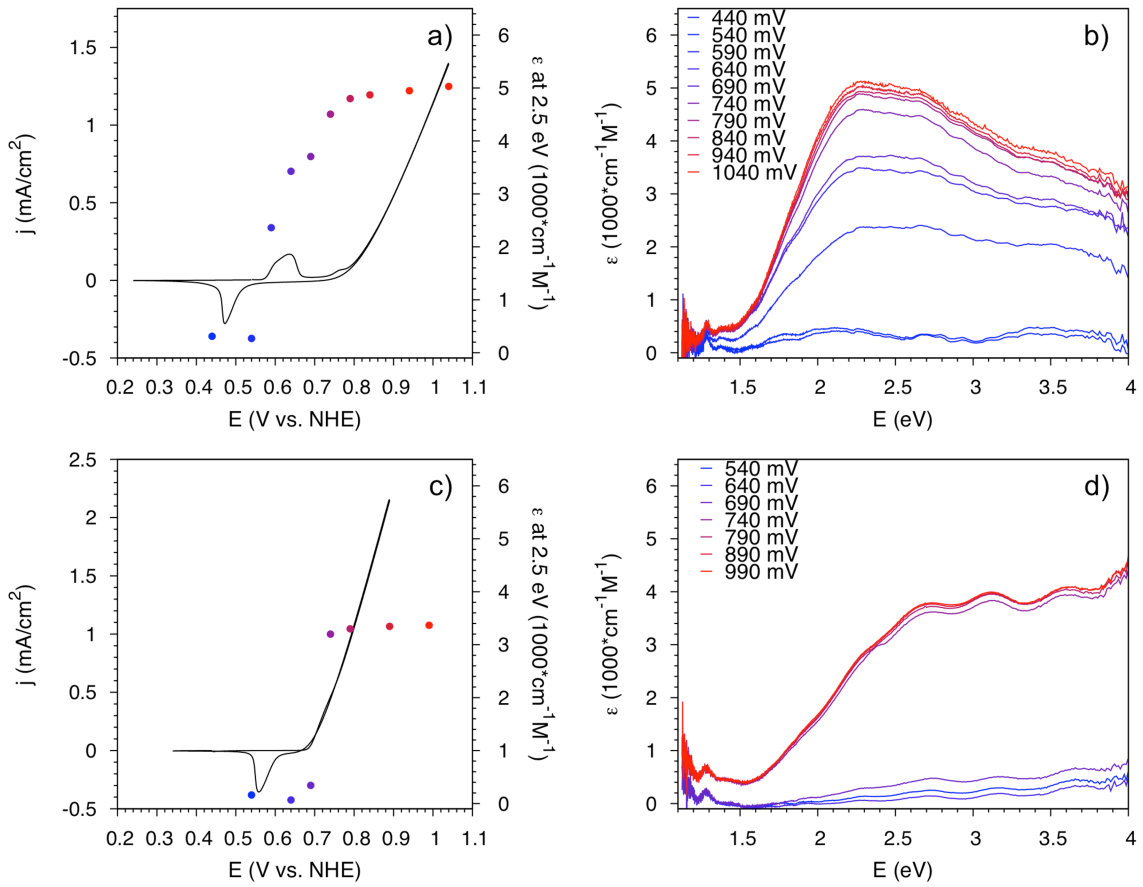

Figure 3.4. Cyclic voltammograms (left) and UV/vis spectra (right) of the (a) and (b) pure Ni and (c) and (d) 25 % Fe films. Data points in the CVs correspond to the absorbance at 2.5 eV with the same color coding as in the spectra. The UV/vis spectra were obtained at steady-state during constant-potential electrocatalysis. Spectroelectrochemistry for intermediate loadings of Fe is shown in Fig. B.10. Copyright 2017 National Academy of Sciences.

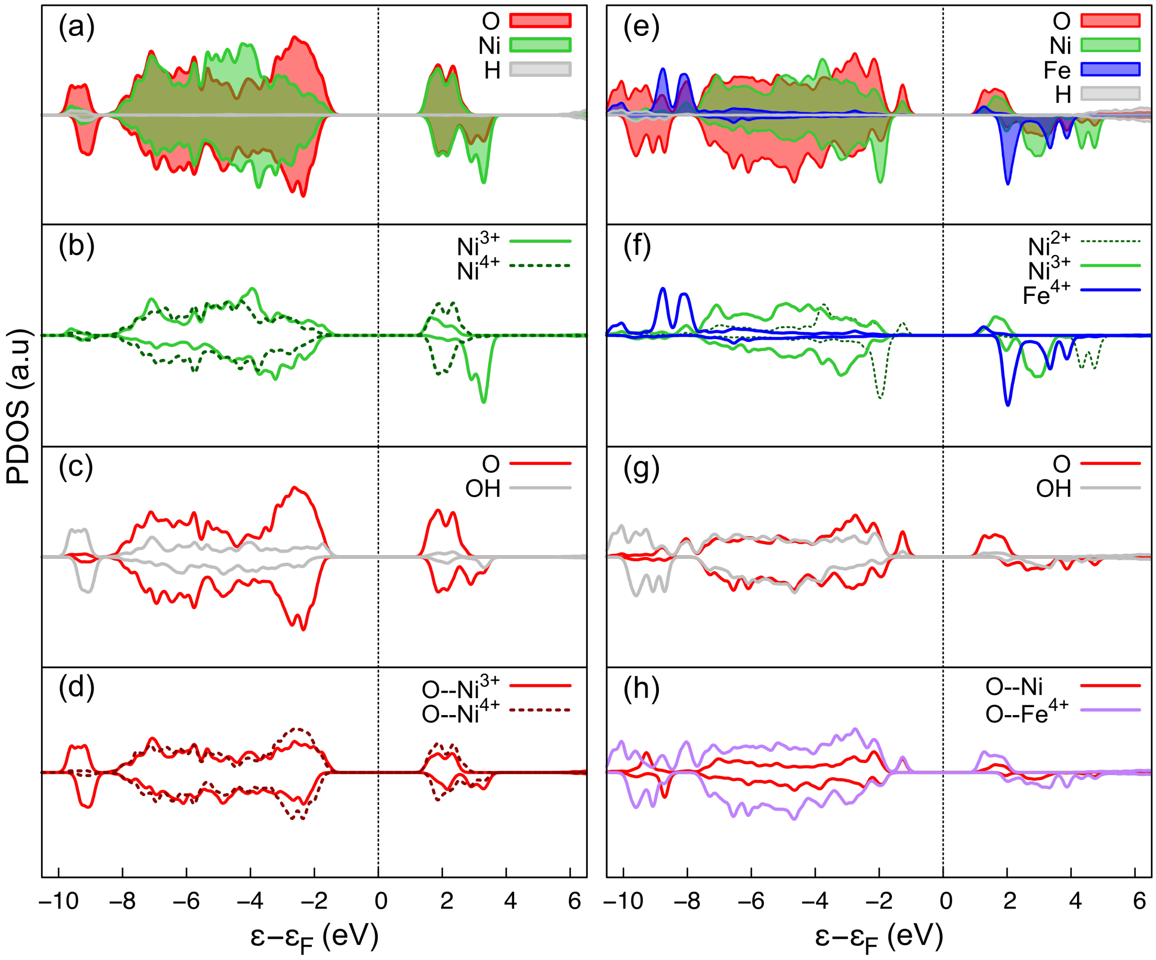

Figure 3.5. PDOS analysis of catalytically active species for (a)-(d) pure $Ni_4O_8H_2$ and (e)-(h) doped $Ni_3Fe_1O_8H_4$. In these plots, the α electronic density is positive (up), and the β electronic density is negative (down). In (c) and (g), O and OH refer to oxide and hydroxide ligand states, respectively. Copyright 2017 National Academy of Sciences.

3.6. Table

Table 3.1. Proton-coupled redox potentials (V vs. NHE) for pure $Ni_4O_8H_n$ and 25% Fe-doped $Ni_3Fe_1O_8H_n$ calculated with PBE0 [a, b]

$Ni_4O_8H_n$			$Ni_3Fe_1O_8H_n$		
Reactant	Products	*E*	Reactant	Products	*E*
8H	6H + H_2	0.52	8H	7H + 0.5 H_2	−0.72
	4H + 2 H_2	0.53 [c]	7H	6H + 0.5 H_2	0.60
	2H + 3 H_2	0.59		5H + 1 H_2	0.52
6H	4H + H_2	0.54		4H + 1.5 H_2	0.55
4H	2H + H_2	0.73		3H + 2 H_2	0.63
2H	0H + H_2	0.92		2H + 2.5 H_2	0.60
				1H + 3 H_2	0.69
				0H + 3.5 H_2	0.73

[a] In the reactant and products, *n*H denotes the stoichiometry of the film.

[b] Plots of the relative formation free energies versus potential for both the pure Ni and the Fe-doped systems are given in Fig. B.2 to facilitate the determination of the most stable stoichiometries at pH 14.

[c] This potential is set equal to the experimental value at pH 14, and all other reported potentials are calculated relative to this value. The analogous table using the 8H → 2H + 3 H_2 reaction as the reference is given as Table B.5, shifting all potentials downward by 0.06 V.

3.7. References

1. Dau, H.; Limberg, C.; Reier, T.; Risch, M.; Roggan, S.; Strasser, P., The mechanism of water oxidation: From electrolysis via homogeneous to biological catalysis. *ChemCatChem* **2010,** *2* (7), 724-761.
2. Walter, M. G.; Warren, E. L.; McKone, J. R.; Boettcher, S. W.; Mi, Q.; Santori, E. A.; Lewis, N. S., Solar water splitting cells. *Chem. Rev.* **2010,** *110* (11), 6446-6473.
3. Singh, A. S., L., Water oxidation catalysts based on abundant 1st row transition metals. *Coord. Chem. Rev.* **2013,** *257*, 2607-2622.
4. Galán-Mascarós, J. R., Water oxidation at electrodes modified with earth abundant transition-metal catalysts. *ChemElectroChem* **2015,** *2* (1), 37-50.
5. Hall, D., Alkaline water electrolysis anode materials. *J. Electrochem. Soc.* **1985,** *132* (2), 41C-48C.
6. Trasatti, S., Physical electrochemistry of ceramic oxides. *Electrochim. Acta* **1991,** *36* (2), 225-241.
7. Corrigan, D. A., The catalysis of the oxygen evolution reaction by iron impurities in thin film nickel oxide electrodes. *J. Electrochem. Soc.* **1987,** *134* (2), 377-384.
8. Park, S.; Shao, Y.; Liu, J.; Wang, Y., Oxygen electrocatalysts for water electrolyzers and reversible fuel cells: Status and perspective. *Energy Environ. Sci.* **2012,** *5* (11), 9331-9344.
9. Miles, M. H., Evaluation of electrocatalysts for water electrolysis in alkaline solutions. *J. Electroanal. Chem.* **1975,** *60* (1), 89-96.
10. Lyons, M. E.; Brandon, M. P., The oxygen evolution reaction on passive oxide covered transition metal electrodes in aqueous alkaline solution. Part 1-Nickel. *Int. J. Electrochem. Sci* **2008,** *3*, 1386-1424.
11. Trotochaud, L.; Young, S. L.; Ranney, J. K.; Boettcher, S. W., Nickel-iron oxyhydroxide oxygen-evolution electrocatalysts: the role of intentional and incidental iron incorporation. *J. Am. Chem. Soc* **2014,** *136* (18), 6744-53.
12. Louie, M. W.; Bell, A. T., An investigation of thin-film Ni–Fe oxide catalysts for the electrochemical evolution of oxygen. *J. Am. Chem. Soc.* **2013,** *135* (33), 12329-37.
13. Li, Y.-F.; Selloni, A., Mechanism and activity of water oxidation on selected surfaces of pure and Fe-doped NiO_x. *ACS Catal.* **2014,** *4* (4), 1148-1153.
14. Dionigi, F.; Strasser, P., NiFe-based (oxy)hydroxide catalysts for oxygen evolution reaction in non-acidic electrolytes. *Adv. Energy Mater.* **2016,** *6*, 1600621.
15. Gerken, J. B.; Shaner, S. E.; Massé, R. C.; Porubsky, N. J.; Stahl, S. S., A survey of diverse earth abundant oxygen evolution electrocatalysts showing enhanced activity from Ni–Fe oxides containing a third metal. *Energy Environ. Sci.* **2014,** *7* (7), 2376-2382.
16. Friebel, D.; Louie, M. W.; Bajdich, M.; Sanwald, K. E.; Cai, Y.; Wise, A. M.; Cheng, M. J.; Sokaras, D.; Weng, T. C.; Alonso-Mori, R.; Davis, R. C.; Bargar, J. R.; Norskov, J. K.; Nilsson, A.; Bell, A. T., Identification of highly active Fe sites in (Ni,Fe)OOH for electrocatalytic water splitting. *J. Am. Chem. Soc.* **2015,** *137* (3), 1305-13.
17. Anisimov, V. I.; Zaanen, J.; Andersen, O. K., Band theory and Mott insulators: Hubbard *U* instead of Stoner *I*. *Phys. Rev. B.* **1991,** *44* (3), 943.
18. Chen, J. Y.; Dang, L.; Liang, H.; Bi, W.; Gerken, J. B.; Jin, S.; Alp, E. E.; Stahl, S. S., Operando analysis of NiFe and Fe oxyhydroxide electrocatalysts for water oxidation: Detection of Fe^{4+} by Mossbauer spectroscopy. *J. Am. Chem. Soc* **2015,** *137* (48), 15090-3.

19. Conesa, J. C., Electronic structure of the (undoped and Fe-doped) NiOOH O_2 evolution electrocatalyst. *J. Phys. Chem. C* **2016,** *120* (34), 18999-19010.

20. Giannozzi, P.; Baroni, S.; Bonini, N.; Calandra, M.; Car, R.; Cavazzoni, C.; Ceresoli, D.; Chiarotti, G. L.; Cococcioni, M.; Dabo, I., QUANTUM ESPRESSO: A modular and open-source software project for quantum simulations of materials. *J. Phys. Condens. Matter* **2009,** *21* (39), 395502.

21. Hamann, D. R.; Schlüter, M.; Chiang, C., Norm-conserving pseudopotentials. *Phys. Rev. Lett.* **1979,** *43* (20), 1494-1497.

22. Schlipf, M.; Gygi, F., Optimization algorithm for the generation of ONCV pseudopotentials. *Comput. Phys. Commun.* **2015,** *196*, 36-44.

23. Perdew, J. P.; Burke, K.; Ernzerhof, M., Generalized gradient approximation made simple. *Phys. Rev. Lett.* **1996,** *77* (18), 3865-3868.

24. Anisimov, V. I.; Aryasetiawan, F.; Lichtenstein, A., First-principles calculations of the electronic structure and spectra of strongly correlated systems: the LDA+*U* method. *J. Phys. Condens. Matter* **1997,** *9* (4), 767.

25. Cococcioni, M.; de Gironcoli, S., Linear response approach to the calculation of the effective interaction parameters in the LDA+*U* method. *Phys. Rev. B* **2005,** *71* (3), 035105.

26. Kulik, H. J.; Cococcioni, M.; Scherlis, D. A.; Marzari, N., Density functional theory in transition-metal chemistry: A self-consistent Hubbard *U* approach. *Phys. Rev. Lett.* **2006,** *97* (10), 103001.

27. Chen, J.; Wu, X.; Selloni, A., Electronic structure and bonding properties of cobalt oxide in the spinel structure. *Phys. Rev. B* **2011,** *83* (24), 245204.

28. Perdew, J. P.; Ernzerhof, M.; Burke, K., Rationale for mixing exact exchange with density functional approximations. *J. Chem. Phys.* **1996,** *105* (22), 9982-9985.

29. Adamo, C.; Barone, V., Toward reliable density functional methods without adjustable parameters: The PBE0 model. *J. Chem. Phys.* **1999,** *110* (13), 6158-6170.

30. Zaffran, J.; Caspary Toroker, M., Benchmarking density functional theory based methods to model NiOOH material properties: Hubbard and van der Waals corrections vs hybrid functionals. *J. Chem. Theory Comput.* **2016,** *12* (8), 3807-12.

31. Skone, J. H.; Govoni, M.; Galli, G., Self-consistent hybrid functional for condensed systems. *Phys. Rev. B* **2014,** *89* (19).

32. Brawand, N. P.; Vörös, M.; Govoni, M.; Galli, G., Generalization of dielectric-dependent hybrid functionals to finite systems. *Phys. Rev. X* **2016,** *6* (4), 041002.

33. Skone, J. H.; Govoni, M.; Galli, G., Nonempirical range-separated hybrid functionals for solids and molecules. *Phys. Rev. B* **2016,** *93* (23), 235106.

34. Hermet, P.; Gourrier, L.; Bantignies, J. L.; Ravot, D.; Michel, T.; Deabate, S.; Boulet, P.; Henn, F., Dielectric, magnetic, and phonon properties of nickel hydroxide. *Phys. Rev. B* **2011,** *84* (23), 235211.

35. Tessier, C.; Haumesser, P.; Bernard, P.; Delmas, C., The structure of $Ni(OH)_2$: From the ideal material to the electrochemically active one. *J. Electrochem. Soc.* **1999,** *146* (6), 2059-2067.

36. Trotochaud, L.; Ranney, J. K.; Williams, K. N.; Boettcher, S. W., Solution-cast metal oxide thin film electrocatalysts for oxygen evolution. *J. Am. Chem. Soc.* **2012,** *134* (41), 17253-17261.

37. Chen, J. Y.; Miller, J. T.; Gerken, J. B.; Stahl, S. S., Inverse spinel $NiFeAlO_4$ as a highly active oxygen evolution electrocatalyst: Promotion of activity by a redox-inert metal ion. *Energy. Environ Sci.* **2014,** *7* (4), 1382-1386.

38. Tkalych, A. J.; Yu, K.; Carter, E. A., Structural and Electronic Features of β-$Ni(OH)_2$ and β-NiOOH from First Principles. *J. Phys. Chem. C* **2015,** *119* (43), 24315-24322.

39. Hunter, B. M.; Blakemore, J. D.; Deimund, M.; Gray, H. B.; Winkler, J. R.; Müller, A. M., Highly active mixed-metal nanosheet water oxidation catalysts made by pulsed-laser ablation in liquids. *J. Am. Chem. Soc.* **2014,** *136* (38), 13118-13121.

40. Hunter, B. M.; Hieringer, W.; Winkler, J. R.; Gray, H. B.; Müller, A. M., Effect of interlayer anions on [NiFe]-LDH nanosheet water oxidation activity. *Energy Environ. Sci.* **2016,** *9*, 1734-1743.

41. Kulik, H. J.; Marzari, N., Accurate potential energy surfaces with a DFT+*U*(R) approach. *J. Chem. Phys.* **2011,** *135* (19), 194105.

42. Merrill, M.; Worsley, M.; Wittstock, A.; Biener, J.; Stadermann, M., Determination of the "NiOOH" charge and discharge mechanisms at ideal activity. *J. Electroanal. Chem* **2014,** *717–718*, 177-188.

43. Smith, R. D. L.; Berlinguette, C. P., Accounting for the dynamic oxidative behavior of nickel anodes. *J. Am. Chem. Soc.* **2016,** *138* (5), 1561-1567.

44. Sit, P. H.; Car, R.; Cohen, M. H.; Selloni, A., Simple, unambiguous theoretical approach to oxidation state determination via first-principles calculations. *Inorg. Chem.* **2011,** *50* (20), 10259-67.

45. Jiang, L.; Levchenko, S. V.; Rappe, A. M., Rigorous definition of oxidation states of ions in solids. *Phys. Rev. Lett.* **2012,** *108*, 166403.

46. Giovannelli, F.; Zaghrioui, M.; Autret-Lambert, C.; Delorme, F.; Seron, A.; Chartier, T.; Pignon, B., Magnetic properties of Ni(II)–Mn(III) LDHs. *Mater. Chem. Phys.* **2012,** *137* (1), 55-60.

47. Görlin, M.; Chernev, P.; Ferreira de Araújo, J.; Reier, T.; Dresp, S.; Paul, B.; Krähnert, R.; Dau, H.; Strasser, P., Oxygen evolution reaction dynamics, faradaic charge efficiency, and the active metal redox states of Ni-Fe oxide water splitting electrocatalysts. *J. Am. Chem. Soc* **2016,** *138*, 5603-5614.

48. Rödl, C.; Bechstedt, F., Optical and energy-loss spectra of the antiferromagnetic transition metal oxides MnO, FeO, CoO, and NiO including quasiparticle and excitonic effects. *Phys. Rev. B.* **2012,** *86* (23), 235122.

49. Burke, M. S.; Enman, L. J.; Batchellor, A. S.; Zou, S.; Boettcher, S. W., Oxygen evolution reaction electrocatalysis on transition metal oxides and (oxy)hydroxides: Activity trends and design principles. *Chem. Mater.* **2015,** *27*, 7549-7558.

50. Zou, S.; Burke, M. S.; Kast, M. G.; Fan, J.; Danilovic, N.; Boettcher, S. W., Fe (oxy)hydroxide oxygen evolution reaction electrocatalysis: intrinsic activity and the roles of electrical conductivity, substrate, and dissolution. *Chem. Mater.* **2015,** *27* (23), 8011-8020.

CHAPTER 4: Dependence of Vibronic Coupling on Molecular Geometry and Environment: Bridging Hydrogen Atom Transfer and Electron-Proton Transfer[§]

4.1. Introduction

Proton-coupled electron transfer (PCET) reactions encompass a broad spectrum of mechanisms.[1-6] For example, such reactions may be sequential or concerted, depending on the existence of a stable intermediate. If a stable intermediate is observed, then the reaction is clearly sequential, but detection of the intermediate may depend on the experimental apparatus. Thus, the absence of an observable intermediate does not definitively imply a concerted reaction. In some cases, the reaction can be determined to be concerted if the products of single electron transfer (ET) and single proton transfer (PT) are much less thermodynamically favorable than the product of the concerted mechanism. This information can often be obtained from the pK_a's and reduction potentials. This chapter will focus on PCET reactions that have been determined to be concerted through such an analysis.

Concerted PCET reactions may be further broken down into hydrogen atom transfer (HAT) and electron-proton transfer (EPT).[7] Traditionally, HAT reactions are characterized by the electron and proton transferring between the same donor and acceptor and hence do not involve a significant change in the electronic charge distribution. In contrast, EPT reactions are characterized by the electron and proton transferring between different donors and acceptors and thus result in a significant change

---

[§] Reproduced with permission from:
Harshan, A. K.; Yu, T.; Soudackov, A. V.; Hammes-Schiffer, S. *J. Am. Chem. Soc* **2015,** *137* (42), 13545-13555. Copyright 2015 American Chemical Society

in the electronic charge distribution. According to these traditional definitions, the donor and acceptor could be an atom, a molecular orbital, or a chemical bond, although such definitions are not rigorous because the quantum mechanical electron and proton tend to be delocalized, and the molecular orbital or chemical bond analysis depends on the representation and level of theory. To provide a more quantitative and well-defined distinction, previously HAT and EPT reactions were shown to be associated with electronically adiabatic and nonadiabatic proton transfer, respectively.[8-9] The distinction between HAT and EPT by the degree of electron-proton nonadiabaticity is consistent with the traditional characterizations mentioned above because the nonadiabatic coupling along the proton transfer coordinate reflects the change in electronic charge distribution as the proton transfers. Thus, a significant change in charge distribution is associated with the electronically nonadiabatic EPT reaction but not with the electronically adiabatic HAT reaction.

Several diagnostics have been devised for distinguishing between HAT and EPT reactions in terms of electron-proton nonadiabaticity.[8-10] A semiclassical formalism developed by Georgievskii and Stuchebrukhov[11] can be used to calculate an effective proton tunneling time τ_p and an electronic transition time τ_e, as well as an adiabaticity parameter that is defined to be the ratio of these two quantities, $p = \tau_p/\tau_e$. The reaction is electronically adiabatic if $p >> 1$ because the electrons respond instantaneously to the proton motion, and the system remains on the electronic ground state. The reaction is electronically nonadiabatic if $p << 1$ because the electrons are unable to respond instantaneously to the proton motion, and excited electronic states are involved. Another diagnostic of electron-proton nonadiabaticity is the magnitude of the first-derivative nonadiabatic coupling between the ground and first excited electronic states along the proton coordinate. A related diagnostic is the magnitude of the change in the electronic charge distribution along the proton coordinate, as reflected by the dipole moment or partial charges.

These diagnostics have been applied to several molecular systems and, more recently, to an enzymatic system. The prototypical examples are the benzyl-toluene and phenoxyl-phenol self-exchange reactions. The former has been shown to be electronically adiabatic (HAT), while the latter has been shown to be electronically nonadiabatic (EPT) according to the diagnostics for electron-proton nonadiabaticity.[8-9] These systems, as well as related systems, have also been studied with other theoretical methods.[12-15] More recently, the PCET reaction catalyzed by the soybean lipoxygenase (SLO) enzyme was shown to be electronically nonadiabatic (EPT) by applying these diagnostics to a gas phase model system.[16] All of these systems were shown to be *vibronically* nonadiabatic in that the overall vibronic coupling is small compared to the thermal energy $k_B T$, thereby validating the use of a golden rule rate constant expression. This vibronic nonadiabaticity is related to the response of the solvent or protein environment to the electron-proton subsystem and is determined by different criteria that have been discussed elsewhere.[17] Theoretical calculations based on the nonadiabatic treatment of the SLO enzyme have reproduced the experimentally observed hydrogen/deuterium kinetic isotope effect of ~80 in the wild-type enzyme and up to ~500 in mutant enzymes.[18-23]

The nonadiabatic PCET rate constant expressions rely on the Condon approximation for the vibronic coupling.[3, 24-25] In nonadiabatic electron transfer theory, the Condon approximation is based on the assumption that the electronic coupling is independent of the nuclear configuration.[26-29] For vibronically nonadiabatic PCET reactions, the Condon approximation is based on the assumption that the vibronic coupling is independent of the nuclear configuration, including both the molecular geometry of the PCET solute complex and the solvent or protein environment. An exception is that the dependence of the vibronic coupling on the proton donor-acceptor distance is included explicitly in the nonadiabatic PCET rate constant expressions.[25] For situations in which the Condon approximation breaks down, a given PCET system could span the electronically adiabatic and nonadiabatic regimes. For both electron transfer and PCET systems, these two regimes may be spanned as the donor-acceptor distances are varied, but the dependence of the coupling and the degree of nonadiabaticity on other geometrical coordinates, as well as the environmental configuration, is less obvious.

In this chapter, we examine the dependence of the magnitude of the vibronic coupling and the degree of electron-proton nonadiabaticity on the molecular geometry and on the solvent or protein configuration. The dependence on molecular geometry is investigated for the phenoxyl-phenol self-exchange system because two transition states corresponding to either an open or a stacked geometry have been identified for this type of system.[13] In particular, for the related benzyl-toluene system, transition states have been optimized with either an open geometry[12] or a stacked geometry,[13] and the stacked geometry was found to be lower in energy by 4.0 kcal/mol at the level of theory used in Ref. [13]. The present study focuses on the phenoxyl-phenol system, which also exhibits both types of transition state geometries. The open geometry of the phenoxyl-phenol system has already been shown to be electronically nonadiabatic,[8-9] but herein we also study the stacked geometry. These calculations test the validity of the Condon approximation for PCET vibronic couplings in solution and proteins. The results have significant implications for applications to PCET in chemical and biological processes.

4.2. Theory and Computational Methods

4.2.1. General theory

The semiclassical formalism for calculating the effective proton tunneling time and electronic transition time is described in detail elsewhere.[8, 11] In this section, we only provide the expressions that are used to calculate the quantities necessary to determine the adiabaticity parameter and the semiclassical vibronic coupling and their physical meaning.

The effective proton tunneling time through this region of width dx is

$$\tau_p = \frac{V^{\mathrm{el}}}{|\Delta F| v_t} \tag{4-1}$$

where v_t is the tunneling velocity of the proton, given by

$$v_t = \sqrt{\frac{2(V_{\mathrm{c}} - E)}{m_{\mathrm{p}}}} \tag{4-2}$$

V_c is the energy at which the potential energy curves cross, m_{p} is the proton mass, and E is the tunneling energy, which is defined as the energy of the degenerate proton vibrational levels in the reactant and product potential wells. The effective electronic transition time between two states separated by V^{el} is given by

$$\tau_e = \frac{\hbar}{V^{\mathrm{el}}} \tag{4-3}$$

which is in the form of time-energy uncertainty relation. Then the adiabaticity parameter p is defined as the ratio of the proton tunneling time and the electronic transition time:

$$p = \frac{\tau_{\mathrm{p}}}{\tau_{\mathrm{e}}} \tag{4-4}$$

The vibronic coupling can be calculated in several different ways, including a full basis set Hamiltonian matrix diagonalization or a semiclassical approach, which have been shown to provide numerically equivalent results for these types of systems.[9] For systems that are known to be in the electronically adiabatic or nonadiabatic regime, expressions derived in these limits can be utilized. Specifically, the vibronic coupling in the electronically adiabatic regime, denoted $V^{(\mathrm{ad})}$, is half the tunneling splitting associated with the ground electronic state. The vibronic coupling in the electronically nonadiabatic regime, denoted $V^{(\mathrm{nad})}$, is given by the following expression:

$$V^{(\mathrm{nad})} = V^{\mathrm{el}} S \tag{4-5}$$

where S is the overlap integral between the proton vibrational wavefunctions calculated for the reactant and product diabatic potentials. In principle, this overlap can be calculated for any pair of reactant and product proton vibrational wavefunctions, but in this chapter we calculate it for only the ground proton vibrational states.

The semiclassical coupling spans the electronically adiabatic and nonadiabatic regimes and is expressed as

$$V^{(\mathrm{sc})} = \kappa V^{(\mathrm{ad})} \tag{4-6}$$

where

$$\kappa = \sqrt{2\pi p}\,\frac{e^{p \ln p - p}}{\Gamma(p+1)} \tag{4-7}$$

Here $\Gamma(x)$ is the gamma function, and p is the adiabaticity parameter defined above. The derivation of these equations is given in Ref. [11]. We calculated the vibronic coupling with all of these methods for the phenoxyl-phenol system to enable a comparison.

The diabatic proton potential energy curves can be calculated in two different ways. For relatively small molecular systems, the adiabatic proton potential energy curves associated with the ground and first excited adiabatic electronic states can be calculated along the proton coordinate with the complete active space self-consistent field (CASSCF) method.[30-31] Subsequently, a diabatization procedure that is exact for two states along a single coordinate (i.e., the nonadiabatic coupling between the two states is identically zero along this coordinate)[9, 32] can be used to generate the diabatic proton potential energy curves from these adiabatic electronic states, as well as the nonadiabatic coupling between them.[9] Alternatively, constrained density functional theory-configuration interaction (CDFT-CI)[33-35] can be used to generate the diabatic proton potential energy curves and the corresponding electronic couplings. In CDFT-CI, the coupling between the two constrained states is approximated as the off-diagonal Hamiltonian matrix element between the two Slater determinants comprised of the Kohn-Sham orbitals for the constrained states.[33, 35] We applied both the CASSCF and CDFT-CI methods to the phenoxyl-phenol molecular system and showed that these two methods lead to qualitatively similar results. The other two diagnostics for electron-proton nonadiabaticity are the nonadiabatic coupling and the change in electronic charge distribution along the proton coordinate. We calculated the nonadiabatic coupling between the lowest two adiabatic electronic states along the one-dimensional proton coordinate with the CASSCF method. This scalar coupling is defined as

$$d_{12}(r_{\mathrm{p}}) = \left\langle \Psi_1^{\mathrm{el}}(\mathbf{r}_{\mathrm{e}};r_{\mathrm{p}}) \,|\, \partial \Psi_2^{\mathrm{el}}(\mathbf{r}_{\mathrm{e}};r_{\mathrm{p}}) \big/ \partial r_{\mathrm{p}} \right\rangle \tag{4-8}$$

where $\Psi_1^{\mathrm{el}}(\mathbf{r}_{\mathrm{e}};r_{\mathrm{p}})$ and $\Psi_2^{\mathrm{el}}(\mathbf{r}_{\mathrm{e}};r_{\mathrm{p}})$ are the ground and first excited adiabatic electronic states, respectively, along the proton coordinate r_{p}. In addition, the dipole moment of the ground electronic state as the proton moves along the proton donor-acceptor axis was calculated using CASSCF.

4.2.2. Computational details

For the phenoxyl-phenol calculations, two different transition state structures, denoted the "open" and "stacked" geometries, were optimized with density functional theory (DFT) at the M06-2X/6-311+G** level of theory in the gas phase using Gaussian09.[36] These structures are depicted in Figure 4.1. At this level of theory, the stacked transition state structure is 4.1 kcal/mol lower in energy than the open transition state structure. For each structure, the adiabatic proton potential energy curves associated with the ground and first excited adiabatic electronic states were obtained by calculating the state-averaged CASSCF energies in the gas phase as the transferring proton was moved along a grid spanning the proton donor-acceptor axis with all other atoms fixed. On the basis of careful analysis of the active spaces over the range of proton coordinates, CAS(3,6) calculations state-averaged over two states were performed for the open structure, and CAS(7,8) calculations state-averaged over four states were performed for the stacked structure to ensure that the active space was conserved along the proton transfer coordinate. Note that these structures are not transition states at the CASSCF level but are useful symmetric structures for the analysis described below.

Additional types of calculations were performed for comparison to these CASSCF results. The effects of dynamic correlation were investigated by performing second-order perturbation theory CASSCF (CASPT2) calculations and comparing the results with those obtained from the CASSCF calculations. The CASSCF energies and first-derivative nonadiabatic couplings reported in the Chapter 4 were performed with MolPro,[37] but the comparison of CASSCF and CASPT2 results provided in the (Appendix C) Information was performed with MolCas.[38-40] In addition, CDFT-CI calculations with the wB97X functional[41] were performed using QChem[42] to obtain the diabatic proton potential energy curves for comparison to the CASSCF results. For the CDFT-CI calculations, the spin density was constrained to be zero on the phenol (left side) and unity on the phenoxyl (right side) fragment for the reactant diabatic state and the reverse for the product diabatic state. The 6-31G** basis set was used for the CASSCF and CDFT-CI calculations. Note that the M062X functional was used for the geometry optimizations because it includes dispersion effects, whereas the wB97X functional was used for calculating the diabatic states and couplings with CDFT-CI because it includes long-range corrections, which are important for describing charge transfer states. A previous benchmarking study[16] illustrated that CDFT-CI calculations with the wB97X functional resulted in similar diabatic states and couplings as those obtained with the CASSCF method for the phenoxyl-phenol system.

The adiabatic electronic states obtained from the CASSCF calculations were diabatized using the method described in previous work.[9] The proton vibrational wavefunctions for each diabatic proton potential energy curve were calculated using the Fourier Grid Hamiltonian (FGH) method.[43] The double adiabatic states defined as products of diabatic electronic states and associated proton vibrational states were used as a basis set to construct a Hamiltonian matrix. Diagonalization of this full basis set Hamiltonian matrix provides the vibronic eigenfunctions and eigenvalues. The vibronic coupling calculated from this full basis set Hamiltonian diagonalization, denoted $V^{(\mathrm{full})}$, is half the energy difference between the two lowest-energy vibronic states. This vibronic coupling was compared to the vibronic coupling calculated with the semiclassical approach, and to the vibronic couplings calculated in the adiabatic and nonadiabatic limits.

4.3. Results

The open and stacked transition state geometries of the phenoxyl-phenol system are depicted in Figure 4.1. The proton donor-acceptor O–O distance is 2.4 Å in both optimized structures. The O–H–O angle is 180° for the open and 166° for the stacked geometry. These structural properties indicate the presence of a reasonably strong hydrogen bond in both geometries. The vibrational mode associated with the transition state imaginary frequency corresponds to proton transfer between the two oxygen atoms for both geometries. Previous studies indicated that the self-exchange reaction for the open geometry of the phenoxyl-phenol system corresponds to the EPT mechanism and is electronically nonadiabatic, while the self-exchange reaction for the open geometry of the benzyl-toluene system corresponds to the HAT mechanism and is electronically adiabatic.[8, 12] For the benzyl-toluene system, a stacked transition state geometry has been found to be lower in energy than the open geometry of this system.[13]

Figure 4.2 depicts the two highest-energy occupied electronic molecular orbitals (MOs) for both the open and stacked geometries of the phenoxyl-phenol system, where the lower MO is doubly occupied and the higher MO is singly occupied. For the open geometry, the PT interface region of these MOs is dominated by 2*p* orbitals perpendicular to the proton donor-acceptor axis with a p-bonding interaction in the doubly occupied MO. In contrast, for the stacked geometry, the PT interface region of these MOs is dominated by atomic orbitals oriented along the proton donor-acceptor axis with a s-bonding interaction in the doubly occupied MO. The character of the MOs in the PT interface region for the stacked geometry is similar to that observed for the benzyl-toluene system, which was previously determined to be electronically adiabatic. Another significant difference between the MOs for the open and stacked geometries is that the doubly occupied MO for the stacked geometry exhibits a π-stacking interaction between the two aromatic rings. As depicted in Figure 4.2, the doubly occupied and singly occupied MOs exhibit bonding and antibonding interactions, respectively, between the aromatic ring orbitals, resulting in a net bonding interaction between the ring moieties for the stacked geometry. This π-stacking interaction increases the electronic coupling, thereby decreasing the electronic transition time relative to the effective proton tunneling time. This analysis suggests that the stacked geometry of the phenoxyl-phenol system may be associated with electronically adiabatic HAT, in contrast to the previously studied open geometry of this system, which was determined to be associated with electronically nonadiabatic EPT.

The CASSCF and CDFT-CI proton potential energy curves for both the open and stacked geometries of the phenoxyl-phenol system are depicted Figure 4.3. For each geometry, the CASSCF and CDFT-CI proton potential energy curves are qualitatively similar, thereby supporting the use of the CDFT-CI method with the ωB97X functional for other PCET systems, including the SLO system discussed below. Additional CASSCF calculations that included four adiabatic electronic states were also performed, but the second and third excited states were found to be much higher in energy than the first excited state (Figure C.1), providing validation for the use of a two-state model. Moreover, the adiabatic proton potential energy curves were also calculated with CASPT2 to examine the effects of dynamical correlation, and the CASSCF and CASPT2 curves were found to be similar (Figure C.2).

Figure 4.3 depicts both the adiabatic (black dashed lines) and diabatic (blue and red solid lines) proton potential energy curves. These curves are qualitatively different for the open and stacked geometries. In particular, the splitting between the ground and first excited adiabatic states is much greater for the stacked geometry. Moreover, the adiabatic and diabatic proton potential energy curves are virtually indistinguishable except in the crossing region for the open geometry but differ significantly for the entire range of proton coordinates for the stacked geometry. These differences are consistent with electronically nonadiabatic self-exchange for the open geometry but electronically adiabatic self-exchange for the stacked geometry.

The degree of electron-proton nonadiabaticity was quantified within the semiclassical formalism by calculating the effective proton tunneling time τ_p and the electronic transition time τ_e, as well as the adiabaticity parameter p, which is the ratio of these two quantities. The values of these parameters are given in Table 4.1. For the open structure, the effective proton tunneling time is much smaller than the electronic transition time, with $p << 1$, indicating that the reaction is electronically nonadiabatic. For the stacked structure, the effective proton tunneling time is larger than the electronic transition time, with $p > 1$, indicating that the reaction is predominantly electronically adiabatic. As discussed below, however, the proton tunneling time and electronic transition time are similar for the stacked structure, with a ratio of $p = 1.4$, so the self-exchange reaction for this geometry can be viewed as being in the intermediate regime between electronically adiabatic and nonadiabatic.

Table 4.1. also provides the vibronic couplings calculated with the full basis set diagonalization method, the semiclassical approach, and the methods that are valid in the adiabatic and nonadiabatic regimes. For both geometries, the full basis set diagonalization and semiclassical couplings are similar to each other because both of these approaches are valid in the adiabatic and nonadiabatic limits as well as the intermediate regime. Thus, the coupling calculated with these two approaches will be denoted the "general" coupling. For the open geometry, the nonadiabatic coupling agrees well with the general coupling, whereas for the stacked geometry, the adiabatic coupling agrees better with the general coupling. These calculations provide further evidence that the open and stacked geometries correspond to electronically nonadiabatic and predominantly electronically adiabatic reactions, respectively.

Figure 4.4 depicts the first-derivative nonadiabatic coupling vector and the dipole moment vector projected along the proton donor-acceptor axis as the proton moves from the donor to the acceptor. The open geometry exhibits a substantial peak in the nonadiabatic coupling and a drastic change in the dipole moment as the proton moves across the midpoint of the proton donor-acceptor axis, whereas the stacked geometry does not exhibit any significant nonadiabatic coupling and only relatively minor and more gradual changes in dipole moment as the proton moves along this axis.

Furthermore, the electrostatic potential maps shown in Figure 4.5. exhibit significant electronic charge transfer between the two aromatic rings as the proton transfers for the open geometry and a much smaller degree of electronic charge transfer between the two rings as the proton transfers for the stacked geometry. In addition, the spin densities depicted in Figure 4.6 illustrate that the unpaired spin density shifts from one ring to the other as the proton transfers in the open geometry but remains delocalized over both rings during proton transfer for the stacked geometry. These observations are consistent with electronically nonadiabatic behavior for the open geometry, corresponding to an EPT mechanism, and predominantly electronically adiabatic behavior for the stacked geometry, corresponding closer to an HAT mechanism.

We emphasize that the stacked geometry does exhibit a small amount of electronic charge redistribution between the two aromatic rings during proton transfer, as indicated by the changes in dipole moment and electrostatic potential, and therefore is not a pure HAT reaction. In other words, the self-exchange reaction for the stacked geometry is not fully electronically adiabatic, as also indicated by the adiabaticity parameter, which is greater than unity but not as large as was observed for the open geometry of the benzyl-toluene system, which is considered to be a pure HAT reaction. The adiabaticity parameter is 1.4 for the stacked geometry of the phenoxyl-phenol system and 3.5 for the open geometry of the benzyl-toluene system.[8] (For further comparison, calculations on the stacked geometry of the benzyl-toluene system[13] are provided in the Supporting Information, indicating an adiabaticity parameter of 10.0.) On the basis of this analysis, we classify the stacked geometry of the phenoxyl-phenol system as a predominantly electronically adiabatic reaction that can be described as an HAT mechanism with a small amount of EPT character. Consequently, the stacked geometry represents an example of a system that is in the intermediate regime between electronically adiabatic and nonadiabatic, or between HAT and EPT, although it is closer toward the electronically adiabatic HAT limit.

Thus, all of these analyses indicate that the open and stacked geometries of the phenoxyl-phenol system are in different regimes. Specifically, the open geometry is electronically nonadiabatic, corresponding to an EPT reaction, while the stacked geometry is in the intermediate regime but predominantly electronically adiabatic, corresponding to an HAT reaction. As given in Table 4.1, the electronic coupling is significantly greater for the stacked geometry than for the open geometry because of the π-stacking interaction between the rings, as indicated by the MOs in Figure 4.2. This stacking interaction decreases the electronic transition time to the extent that the electrons are able to respond instantaneously to the proton motion, thereby leading to an electronically adiabatic proton transfer that remains on the electronic ground state. This reaction involves only a small amount of electronic charge redistribution between the rings, supporting the designation of a primarily HAT mechanism for this geometry. In contrast, the open geometry involves a significant shift in electronic charge distribution from one ring to the other, and these rings are further apart with weaker interactions, supporting the designation of EPT for this geometry. These calculations illustrate that a single molecular system can span the electronically adiabatic and nonadiabatic limits as it explores configurational space via thermal fluctuations. Moreover, at certain geometries the reaction may lie in the intermediate regime between the electronically adiabatic and nonadiabatic limits and therefore can no longer be designated as either HAT or EPT.

4.4. Conclusions

In this chapter, we tested the Condon approximation for PCET vibronic couplings, which strongly impact the rate constants. Calculations of the vibronic coupling for the phenoxyl-phenol self-exchange reaction illustrate that the open geometry is electronically nonadiabatic, while the stacked geometry is in the intermediate regime but is predominantly electronically adiabatic. The electronic coupling is significantly greater for the stacked geometry than for the open geometry because of the π-stacking bonding interaction between the rings in the stacked geometry. Moreover, the self-exchange reaction involves substantially more electronic charge redistribution in the open geometry than in the stacked geometry. On the basis of this analysis, the reaction is identified as EPT in the open geometry and primarily HAT, with a small amount of EPT character, in the stacked geometry. These calculations demonstrate a breakdown in the Condon approximation in that the vibronic coupling depends strongly on the geometry of the PCET complex. This geometric dependence is not simply a dependence on the donor-acceptor distance, which is a well-known phenomenon, but rather is a more interesting dependence on the intramolecular angle between the planes of two aromatic rings. Thus, these calculations suggest that the Condon could be invalid for the solute nuclear coordinates, particularly intramolecular coordinates that influence the π-stacking interactions for systems with aromatic rings. Moreover, a single molecular system can span the electronically adiabatic and nonadiabatic limits through thermal fluctuations that lead to conformational changes. The form of the vibronic coupling is different in these two regimes, as well as in the intermediate regime. The mechanistic interpretation is also different in these two regimes, resulting in the possibility that a single system can exhibit both HAT and EPT character. Thus, simulations of PCET reactions, calculations of PCET rate constants, and mechanistic interpretations should account for the possibility of spanning both regimes, as well as the potential breakdown of the Condon approximation, for certain types of systems.

4.5. Figures

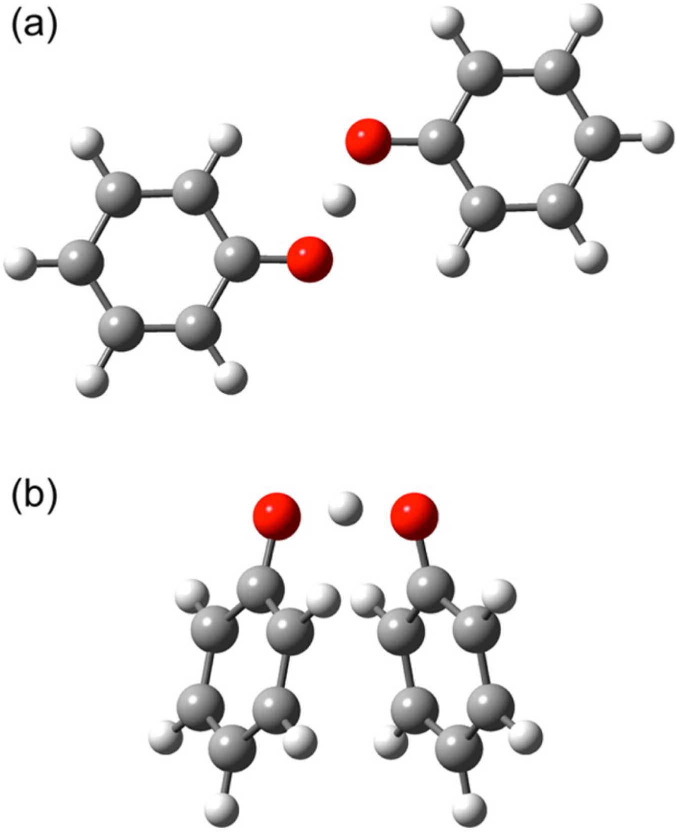

Figure 4.1. Open (a) and stacked (b) transition state structures for the self-exchange phenoxyl-phenol reaction calculated at the DFT/M06-2X/6-311+G** level of theory. The proton is transferring between the two red oxygen atoms.

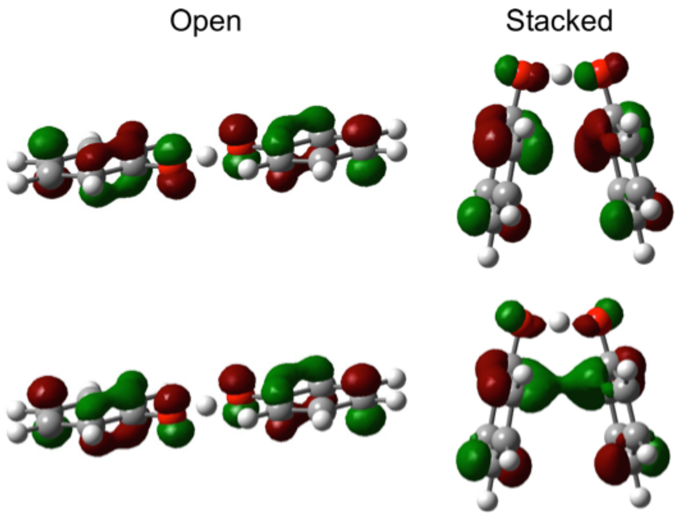

Figure 4.2. Highest occupied molecular orbitals for the open (left) and stacked (right) geometries for the dominant configuration obtained from the CASSCF calculations. The lower MO is doubly occupied, and the higher MO is singly occupied. Copyright 2015 American Chemical Society.

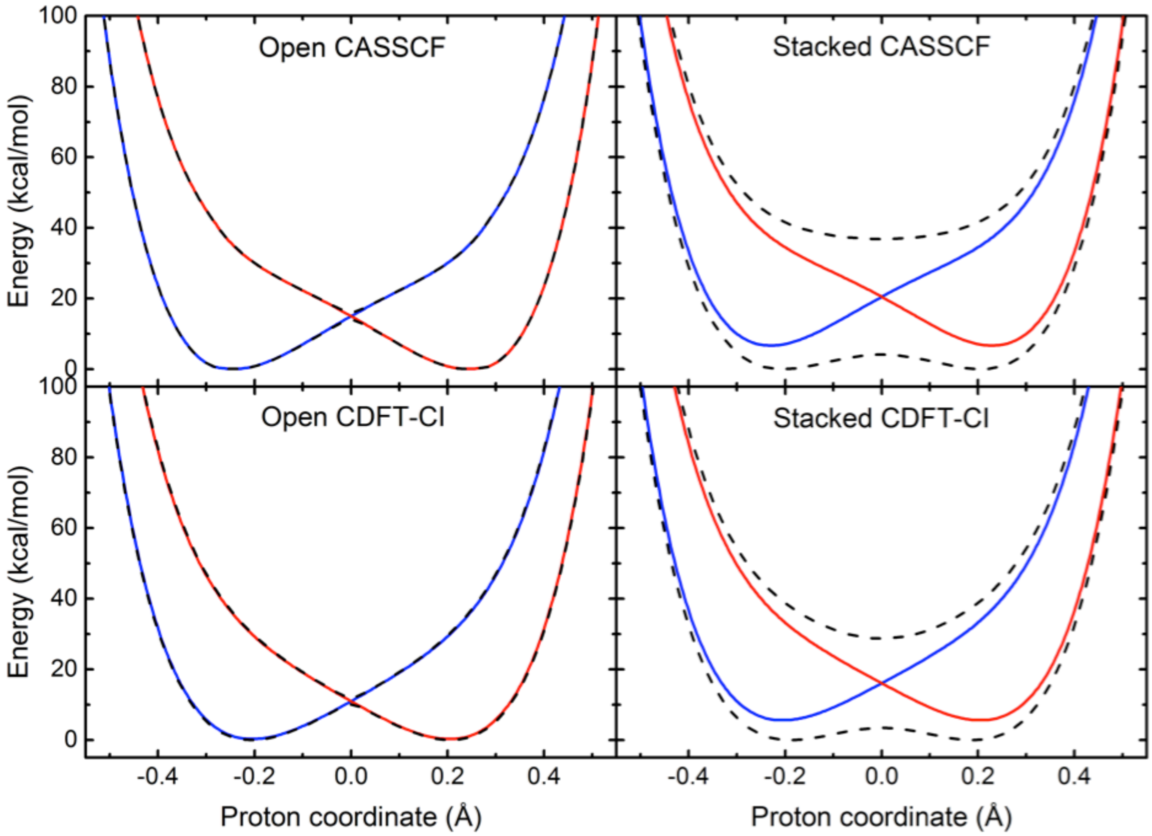

Figure 4.3. Adiabatic (black dashed lines) and diabatic (blue and red solid lines) proton potential energy curves for the open (left panels) and stacked (right panels) geometries of the phenoxyl-phenol system obtained using the CASSCF/6-31G** (upper panels) and CDFT-CI/ωB97X/6-31G** (lower panels) methods. Copyright 2015 American Chemical Society.

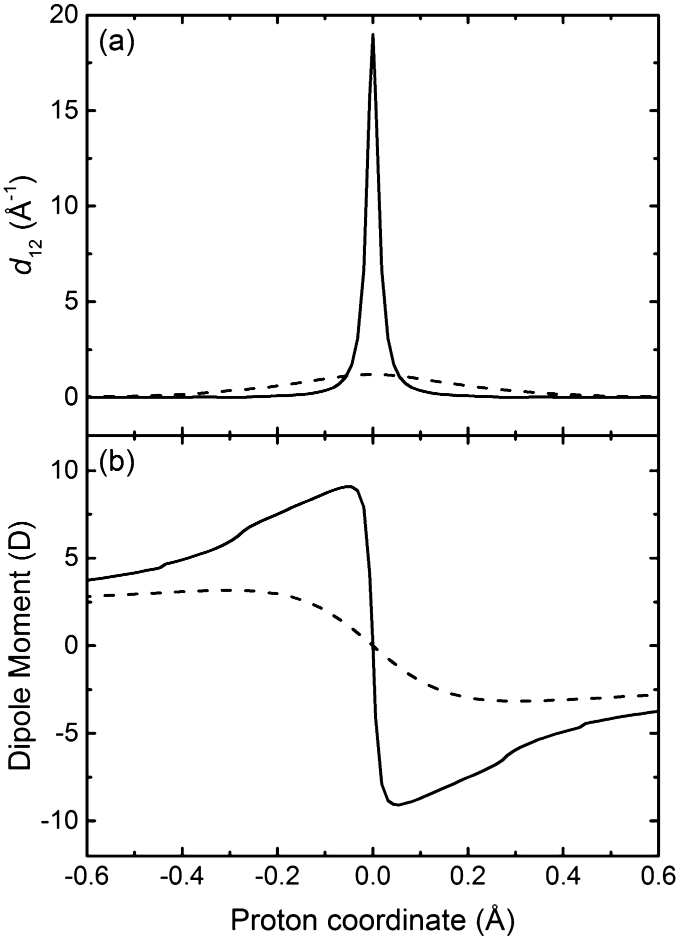

Figure 4.4. (a) Component of the first-order nonadiabatic coupling vector, as defined in Eq. 4-8, between the CASSCF/6-31G** ground and first excited adiabatic electronic states as the proton moves along the proton donor-acceptor axis for the open (solid) and stacked (dashed) geometries of the phenoxyl-phenol system. (b) Component of the dipole moment vector as the proton moves along the proton donor-acceptor axis for the CASSCF/6-31G** ground adiabatic electronic state for the open (solid) and stacked (dashed) geometries of the phenoxyl-phenol system. Copyright 2015 American Chemical Society.

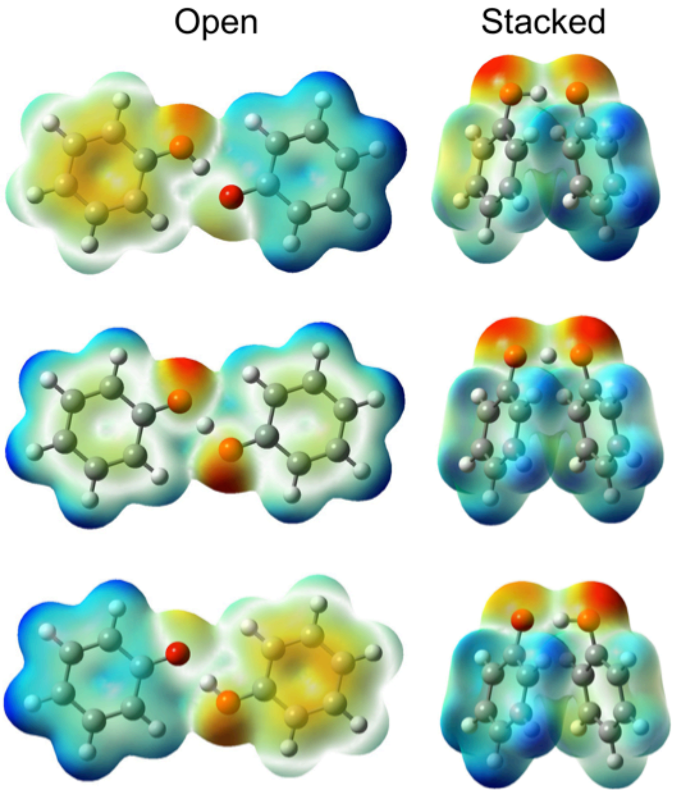

Figure 4.5. Electrostatic potential maps for the ground adiabatic electronic states generated with DFT/ωB97X/6-31G** for the reactant (top), transition state (middle), and product (bottom) positions of the transferring hydrogen for the open (left) and stacked (right) geometries of the phenoxyl-phenol system. The density isosurface value is 0.005, and negatively and positively charged regions are indicated by red and blue coloring, respectively. Copyright 2015 American Chemical Society.

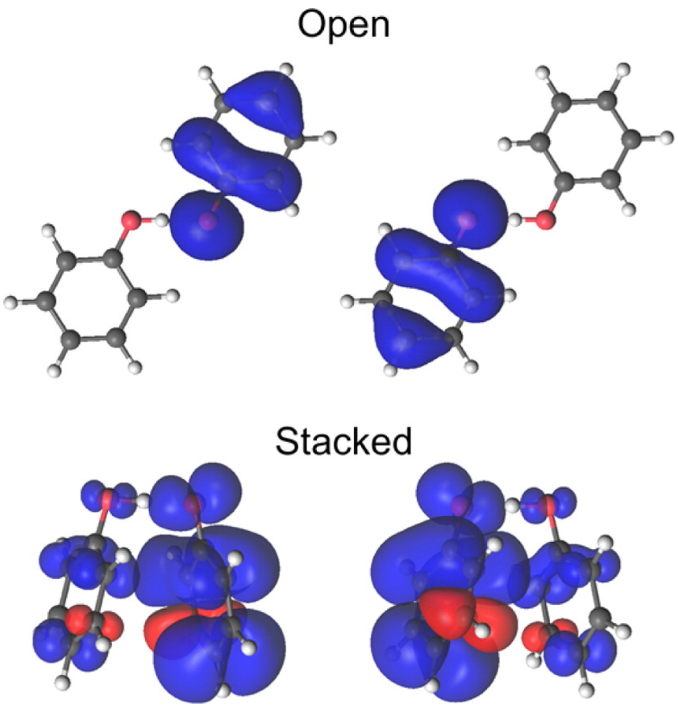

Figure 4.6. Spin densities after spin projection for the open (top) and stacked (bottom) geometries of the phenoxyl-phenol system obtained from unrestricted DFT/ωB97X/6-31G** calculations for the reactant (left) and product (right) positions of the transferring hydrogen. Copyright 2015 American Chemical Society.

4.6. Table

Table 4.1. Electronic coupling, semiclassical parameters, and vibronic couplings calculated with various methods for open and stacked geometries of phenoxyl-phenol system

Geometry	V^{el} (cm^{-1})	τ_{p} (fs)	τ_{e} (fs)	$p = \tau_{\text{p}}/\tau_{\text{e}}$
Open	375	0.076	14.12	0.00535
Stacked	5735	1.272	0.926	1.374
Geometry	$V^{\text{(full)}}$ (cm^{-1})	$V^{\text{(sc)}}$ (cm^{-1})	$V^{\text{(ad)}}$ (cm^{-1})	$V^{\text{(na)}\,a}$ (cm^{-1})
Open	8.57	9.05	50.86	8.55 (8.74)
Stacked	263	260	276	203 (205)

[a] The first value for $V^{\text{(na)}}$ is the matrix element of the product of $V^{\text{el}}(r_{\text{p}})$ and the ground reactant and product proton vibrational wavefunctions, and the value in parentheses is obtained from Eq. 4-2 with V^{el} calculated at $r_{\text{p}} = 0$ (i.e., the product of V^{el} and the overlap integral between the ground reactant and product proton vibrational wavefunctions). The similarity between these two values indicates that V^{el} does not depend strongly on r_{p}.

4.7. References

1. Cukier, R.; Nocera, D. G., Proton-coupled electron transfer. *Ann. Rev. Phys. Chem.* **1998,** *49*, 337-369.
2. Huynh, M. H. V.; Meyer, T. J., Proton-coupled electron transfer. *Chem. Rev.* **2007,** *107* (11), 5004-5064.
3. Hammes-Schiffer, S.; Soudackov, A. V., Proton-coupled electron transfer in solution, proteins, and electrochemistry. *J. Phys. Chem. B* **2008,** *112* (45), 14108-14123.
4. Hammes-Schiffer, S.; Stuchebrukhov, A. A., Theory of coupled electron and proton transfer reactions. *Chem. Rev.* **2010,** *110* (12), 6939-6960.
5. Warren, J. J.; Tronic, T. A.; Mayer, J. M., Thermochemistry of proton-coupled electron transfer reagents and its implications. *Chem. Rev.* **2010,** *110*, 6961-7001.
6. Hammes-Schiffer, S., Proton-coupled electron transfer: classification scheme and guide to theoretical methods. *Energy Environ. Sci.* **2012,** *5* (7), 7696-7703.
7. Hunter, B. M.; Hieringer, W.; Winkler, J. R.; Gray, H. B.; Müller, A. M., Effect of interlayer anions on [NiFe]-LDH nanosheet water oxidation activity. *Energy Environ. Sci.* **2016,** *9*, 1734-1743.
8. Skone, J. H.; Soudackov, A. V.; Hammes-Schiffer, S., Calculation of vibronic couplings for phenoxyl/phenol and benzyl/toluene self-exchange reactions: implications for proton-coupled electron transfer mechanisms. *J. Am. Chem. Soc* **2006,** *128* (51), 16655-16663.
9. Sirjoosingh, A.; Hammes-Schiffer, S., Proton-coupled electron transfer versus hydrogen atom transfer: generation of charge-localized diabatic states. *J. Phys. Chem. A* **2011,** *115* (11), 2367-2377.
10. Sirjoosingh, A.; Hammes-Schiffer, S., Diabatization schemes for generating charge-localized electron-proton vibronic states in proton-coupled electron transfer systems. *J. Chem. Theory Comput.* **2011,** *7* (9), 2831-2841.
11. Georgievskii, Y.; Stuchebrukhov, A. A., Concerted electron and proton transfer: Transition from nonadiabatic to adiabatic proton tunneling. *J. Chem. Phys.* **2000,** *113*, 10438-10450.
12. Mayer, J. M.; Hrovat, D. A.; Thomas, J. L.; Borden, W. T., Proton-coupled electron transfer versus hydrogen atom transfer in benzyl/toluene, methoxyl/methanol, and phenoxyl/phenol self-exchange reactions. *J. Am. Chem. Soc* **2002,** *124* (37), 11142-11147.
13. DiLabio, G. A.; Johnson, E. R., Lone pair−π and π−π interactions play an important role in proton-coupled electron transfer reactions. *J. Am. Chem. Soc* **2007,** *129* (19), 6199-6203.
14. Tishchenko, O.; Truhlar, D. G.; Ceulemans, A.; Nguyen, M. T., A unified perspective on the hydrogen atom transfer and proton-coupled electron transfer mechanisms in terms of topographic features of the ground and excited potential energy surfaces as exemplified by the reaction between phenol and radicals. *J. Am. Chem. Soc.* **2008,** *130* (22), 7000-7010.
15. Cembran, A.; Provorse, M. R.; Wang, C. W.; Wu, W.; Gao, J. L., The third timension of a more O'Ferrall-Jencks diagram for hydrogen atom transfer in the isoelectronic hydrogen exchange reactions of $(PhX)_2H^{\cdot}$ with X = O, NH, and CH_2. *J. Chem. Theory Comput.* **2012,** *8* (11), 4347-4358.

16. Soudackov, A. V.; Hammes-Schiffer, S., Probing nonadiabaticity in the proton-coupled electron transfer reaction catalyzed by soybean lipoxygenase. *J. Phys. Chem. Lett.* **2014,** *5* (18), 3274-3278.

17. Barzykin, A. V.; Frantsuzov, P. A.; Seki, K.; Tachiya, M., Solvent effects in nonadiabatic electron-transfer reactions: Theoretical aspects. *Adv. Chem. Phys.* **2002,** *123*, 511-616.

18. Knapp, M. J.; Rickert, K.; Klinman, J. P., Temperature-dependent isotope effects in soybean lipoxygenase-1: Correlating hydrogen tunneling with protein dynamics. *J. Am. Chem. Soc* **2002,** *124* (15), 3865-3874.

19. Hatcher, E.; Soudackov, A. V.; Hammes-Schiffer, S., Proton-coupled electron transfer in soybean lipoxygenase. *J. Am. Chem. Soc* **2004,** *126* (18), 5763-5775.

20. Hatcher, E.; Soudackov, A. V.; Hammes-Schiffer, S., Proton-coupled electron transfer in soybean lipoxygenase: Dynamical behavior and temperature dependence of kinetic isotope effects. *J. Am. Chem. Soc* **2007,** *129* (1), 187-196.

21. Meyer, M. P.; Tomchick, D. R.; Klinman, J. P., Enzyme structure and dynamics affect hydrogen tunneling: The impact of a remote side chain (1553) in soybean lipoxygenase-1. *Proc. Natl. Acad. Sci. U.S.A.* **2008,** *105* (4), 1146-1151.

22. Edwards, S. J.; Soudackov, A. V.; Hammes-Schiffer, S., Impact of distal mutation on hydrogen transfer interface and substrate conformation in soybean lipoxygenase. *J. Phys. Chem. B* **2010,** *114* (19), 6653-6660.

23. Hu, S. S.; Sharma, S. C.; Scouras, A. D.; Soudackov, A. V.; Carr, C. A. M.; Hammes-Schiffer, S.; Alber, T.; Klinman, J. P., Extremely elevated room-temperature kinetic isotope effects quantify the critical role of barrier width in enzymatic C-H activation. *J. Am. Chem. Soc* **2014,** *136* (23), 8157-8160.

24. Soudackov, A.; Hammes-Schiffer, S., Derivation of rate expressions for nonadiabatic proton-coupled electron transfer reactions in solution. *J. Chem. Phys.* **2000,** *113* (6), 2385-2396.

25. Soudackov, A.; Hatcher, E.; Hammes-Schiffer, S., Quantum and dynamical effects of proton donor-acceptor vibrational motion in nonadiabatic proton-coupled electron transfer reactions. *J. Chem. Phys.* **2005,** *122* (1), 014505.

26. Beratan, D. N.; Hopfield, J. J., Failure of the Born-Oppenheimer and Franck-Condon approximations for long-distance electron-transfer rate calculations. *J. Chem. Phys.* **1984,** *81* (12), 5753-5759.

27. Cave, R. J.; Newton, M. D., Calculation of electronic coupling matrix elements for ground and excited state electron transfer reactions: Comparison of the generalized Mulliken-Hush and block diagonalization methods. *J. Chem. Phys.* **1997,** *106* (22), 9213-9226.

28. Toutounji, M. M.; Ratner, M. A., Testing the condon approximation for electron transfer via the Mulliken-Hush model. *J. Phys. Chem. A* **2000,** *104* (37), 8566-8569.

29. Newton, M. D., Electronic coupling in electron transfer and the influence of nuclear modes: theoretical and computational probes. *Theor. Chem. Acc.* **2003,** *110* (5), 307-321.

30. Werner, H. J.; Knowles, P. J., A 2nd order multiconfiguration SCF procedure with optimum convergence. *J. Chem. Phys.* **1985,** *82* (11), 5053-5063.

31. Knowles, P. J.; Werner, H. J., An efficient 2nd-order MCSCF method for long configuration expansions. *Chem. Phys. Lett.* **1985,** *115* (3), 259-267.

32. Baer, M., Adiabatic and diabatic representations for atom-molecule collisions: Treatment of collinear arrangement. *Chem. Phys. Lett.* **1975,** *35* (1), 112-118.

33. Wu, Q.; Van Voorhis, T., Constrained density functional theory and its application in long-range electron transfer. *J. Chem. Theor. Comp.* **2006,** *2* (3), 765-774.

34. Wu, Q.; Van Voorhis, T., Direct calculation of electron transfer parameters through constrained density functional theory. *J. Phys. Chem. A* **2006,** *110* (29), 9212-9218.

35. Wu, Q.; Cheng, C. L.; Van Voorhis, T., Configuration interaction based on constrained density functional theory: A multireference method. *J. Chem. Phys.* **2007,** *127* (16).

36. Frisch, M. J.; Trucks, G. W.; Schlegel, H. B.; Scuseria, G. E.; Robb, M. A.; Cheeseman, J. R.; Scalmani, G.; Barone, V.; Mennucci, B.; Petersson, G. A.; Nakatsuji, H.; Caricato, M.; Li, X.; Hratchian, H. P.; Izmaylov, A. F.; Bloino, J.; Zheng, G.; Sonnenberg, J. L.; Hada, M.; Ehara, M.; Toyota, K.; Fukuda, R.; Hasegawa, J.; Ishida, M.; Nakajima, T.; Honda, Y.; Kitao, O.; Nakai, H.; Vreven, T.; J. A. Montgomery, J.; Peralta, J. E.; Ogliaro, F.; Bearpark, M.; Heyd, J. J.; Brothers, E.; Kudin, K. N.; Staroverov, V. N.; Kobayashi, R.; Normand, J.; Raghavachari, K.; Rendell, A.; Burant, J. C.; Iyengar, S. S.; Tomasi, J.; Cossi, M.; Rega, N.; Millam, J. M.; Klene, M.; Knox, J. E.; Cross, J. B.; Bakken, V.; Adamo, C.; Jaramillo, J.; Gomperts, R.; Stratmann, R. E.; Yazyev, O.; Austin, A. J.; Cammi, R.; Pomelli, C.; Ochterski, J. W.; Martin, R. L.; Morokuma, K.; Zakrzewski, V. G.; Voth, G. A.; Salvador, P.; Dannenberg, J. J.; Dapprich, S.; Daniels, A. D.; Farkas, Ö.; Foresman, J. B.; Ortiz, J. V.; Cioslowski, J.; Fox, D. J. *Gaussian 09, Revision C.1*, Gaussian, Inc.: Wallingford CT, 2009.

37. Werner, H.-J. K., P. J.; Knizia, G.; Manby, F. R.; Schütz, M.; Celani, P.; Korona, T.; Lindh, R.; Mitrushenkov, A.; Rauhut, G.; Shamasundar, K. R.; Adler, T. B.; Amos, R. D.; Bernhardsson, A.; Berning, A.; Cooper, D. L.; Deegan, M. J. O.; Dobbyn, A.; Eckert, J. F.; Goll, E.; Hampel, C.; Hesselmann, A.; Hetzer, G.; Hrenar, T.; Jansen, G.; Köppl, C.; Liu, Y.; A. Lloyd, W. R.; Mata, A.; May, A.; McNicholas, J. S. J.; Meyer, W.; Mura, M. E.; Nicklass, A.; O'Neill, D. P.; Palmieri, P.; Peng, D.; Pflüger, K.; Pitzer, R.; Reiher, M.; Shiozaki, T.; Stoll, H.; Stone, A. J.; Tarroni, R.; Thorsteinsson, T.; Wang, M. *MOLPRO*, version 2010.1; see http://www.molpro.net.

38. Aquilante, F.; De Vico, L.; Ferre, N.; Ghigo, G.; Malmqvist, P. A.; Neogrady, P.; Pedersen, T. B.; Pitonak, M.; Reiher, M.; Roos, B. O.; Serrano-Andres, L.; Urban, M.; Veryazov, V.; Lindh, R., Software news and update MOLCAS 7: The next generation. *J. Comput. Chem.* **2010,** *31* (1), 224-247.

39. Karlstrom, G.; Lindh, R.; Malmqvist, P. A.; Roos, B. O.; Ryde, U.; Veryazov, V.; Widmark, P. O.; Cossi, M.; Schimmelpfennig, B.; Neogrady, P.; Seijo, L., MOLCAS: a program package for computational chemistry. *Comp Mater Sci* **2003,** *28* (2), 222-239.

40. Veryazov, V.; Widmark, P. O.; Serrano-Andres, L.; Lindh, R.; Roos, B. O., MOLCAS as a development platform for quantum chemistry software. *Int. J. Quantum Chem.* **2004,** *100* (4), 626-635.

41. Chai, J. D.; Head-Gordon, M., Systematic optimization of long-range corrected hybrid density functionals. *J. Chem. Phys.* **2008,** *128* (8).

42. Shao, Y.; Molnar, L. F.; Jung, Y.; Kussmann, J.; Ochsenfeld, C.; Brown, S. T.; Gilbert, A. T. B.; Slipchenko, L. V.; Levchenko, S. V.; O Neill, D. P.; DiStasio Jr, R. A.; Lochan, R. C.; Wang, T.; Beran, G. J. O.; Besley, N. A.; Herbert, J. M.; Yeh Lin, C.; Van

Voorhis, T.; Hung Chien, S.; Sodt, A.; Steele, R. P.; Rassolov, V. A.; Maslen, P. E.; Korambath, P. P.; Adamson, R. D.; Austin, B.; Baker, J.; Byrd, E. F. C.; Dachsel, H.; Doerksen, R. J.; Dreuw, A.; Dunietz, B. D.; Dutoi, A. D.; Furlani, T. R.; Gwaltney, S. R.; Heyden, A.; Hirata, S.; Hsu, C.-P.; Kedziora, G.; Khalliulin, R. Z.; Klunzinger, P.; Lee, A. M.; Lee, M. S.; Liang, W.; Lotan, I.; Nair, N.; Peters, B.; Proynov, E. I.; Pieniazek, P. A.; Min Rhee, Y.; Ritchie, J.; Rosta, E.; David Sherrill, C.; Simmonett, A. C.; Subotnik, J. E.; Lee Woodcock III, H.; Zhang, W.; Bell, A. T.; Chakraborty, A. K.; Chipman, D. M.; Keil, F. J.; Warshel, A.; Hehre, W. J.; Schaefer III, H. F.; Kong, J.; Krylov, A. I.; Gill, P. M. W.; Head-Gordon, M., Advances in methods and algorithms in a modern quantum chemistry program package. *Phys. Chem. Chem. Phys.* **2006,** *8* (27), 3172-3191.

43. Marston, C. C.; Balint-kurti, G. G., The fourier grid hamiltonian method for bound-state eigenvalues and eigenfunctions. *J. Chem. Phys.* **1989,** *91* (6), 3571-3576.

CHAPTER 5: Concerted Proton-Coupled Electron Transfer Mechanism in the Reaction of the Cumyloxyl Radical with Hydroquinone[§]

5.1. Introduction

Benzoquinone/hydroquinone systems play an important role in various chemical and biological charge transfer processes, especially in catalysis.[1-2] The electron or proton withdrawing nature of the substituents on the quinone systems can have significant effects on these processes. For the study detailed in this chapter, our experimental collaborators generated CumO$^\bullet$ radical by laser flash photolysis (LFP) and studied its reactions with 1,4-hydroquinone (**1**-H_2) and 2-(1-piperidinylmethyl)-1,4-hydroquinone (**2**-H_2). The viability of the EPT process can be tuned by modifying the simple hydroquinone structure, **1**-H_2, as exemplified by (**2**-H_2). Time-resolved spectroscopic studies illustrated that the intermediates formed in CumO$^\bullet$ reacting with **1**-H_2 and **2**-H_2 are significantly different, as also reflected in the rate constants and kinetic isotope effects (KIEs) for the two reactions. These results suggest that the proton abstraction by the piperidine ring causes the CumO$^\bullet$/hydroquionone reaction to turn into a concerted E2PT process, where the transfer of one electron is accompanied by two proton transfers occurring simultaneously. Interestingly, the KIE is ~2.8 for 1-H_2 and ~1.0 for 2-H_2, which were characterized experimentally to undergo EPT and E2PT processes, respectively. In this chapter, these two systems are studied using DFT methods, and their

---

[§] Manuscript in preparation, as a collaboration between Harshan, A. K.; Huynh, M. T.; Soudackov, A.; Bietti, M.; and Hammes-Schiffer, S.

rates and KIEs are calculated using vibronically nonadiabatic PCET rate constant expressions. A comparison between these two systems provides a better understanding of the experimental observations.

5.2. Methodology

The expressions for vibronically nonadiabatic PCET rate constants have been derived previously.[3-4] These rate constants depend strongly on the proton donor-acceptor distance, R. For these types of applications, the total PCET rate constant is calculated by a thermal averaging procedure, where the rate constant is calculated for a series of R values, each rate constant is multiplied by the probability of sampling that value of R, and this product is integrated over all relevant R values.

The expression to calculate rate constant k at a fixed donor-acceptor distance R is given below

$$k(R) = \sum_{\mu,\nu} P_\mu \frac{[V^{\mathrm{el}} S_{\mu\nu}(R)]^2}{\hbar} \sqrt{\frac{\pi}{k_B T \lambda}} \exp\left(-\frac{\Delta G^{\ddagger}_{\mu\nu}(R)}{k_B T} \right) \tag{5-1}$$

Here, P_μ is the Boltzmann population of the reactant proton vibrational state μ, V^{el} is the electronic coupling, $S_{\mu\nu}$ is the overlap integral between state μ of the reactant and state ν of the product, k_{B} is the Boltzmann constant, T is temperature, $\Delta G^{\ddagger}_{\mu\nu}$ is the free energy barrier for the pair of states μ (reactant) and ν (product), and λ is the total reorganization energy. The total rate constant is calculated by multiplying the probability distribution function, $P(R)$, and the rate constant $k(R)$, and then integrating over R.

$$k^{\mathrm{EPT}} = \int P(R) k(R) \, dR \tag{5-2}$$

For these types of E2PT systems, the dominant proton donor-acceptor mode is assumed to correspond to the symmetrical combination of the two proton donor-acceptor distances, $R1$ and $R2$. Thus, the thermal averaging procedure is performed over a single dimension corresponding to the simultaneous change in both $R1$ and $R2$ relative to their equilibrium values.

For both systems, the reactant and product structures corresponding to EPT for **1**-H_2 and E2PT for **2**-H_2 were optimized with DFT using the B3LYP functional and 6-31++G** basis set in acetonitrile solvent. The solvent effects were incorporated using the C-PCM model[5] with Bondi radii[6] including dispersion, repulsion[7] interactions, and cavity formation.[8] For **2**-H_2, no minimum corresponding to the EPT product (i.e., with the proton transferred to $CumO^{\bullet}$ in the absence of the intramolecular proton transfer) or with the intramolecular proton transferred in the absence of the intermolecular proton transfer" was found at this level of theory, suggesting a concerted E2PT mechanism. Several different reactant and product geometry minima were found for the **2**-H_2 system, and the lowest-energy geometries were used for this study. The reactant and product geometries used in this study are shown in Figure 5.2. The driving force for these reactions was computed as the difference in free energies at the reactant and product equilibrium geometries, which included zero-point energies, entropic contributions, and solvation free energies.

The total reorganization energy is defined as the sum of the inner and outer sphere reorganization energies. The outer-sphere (solvent) reorganization energy was calculated using the frequency-resolved cavity model (FRCM).[9-10] The fixed charge densities of the reactant and product states were represented by collections of partial atomic charges obtained with the CHELPG method.[11] Specifically, these charges were computed for the reactant and product equilibrium geometries.

The inner-sphere reorganization energy was calculated using the four-point method extended to PCET reactions:[12]

$$\lambda_\mathrm{i} = \tfrac{1}{2}\left(E([\mathrm{DH}\ldots\mathrm{A}^\bullet]_\mathrm{prod}) - E([\mathrm{DH}\ldots\mathrm{A}^\bullet]_\mathrm{reac}) + E([\mathrm{D}^\bullet\ldots\mathrm{HA}]_\mathrm{reac}) - E([\mathrm{D}^\bullet\ldots\mathrm{HA}]_\mathrm{prod})\right) \quad (5\text{-}3)$$

In the above expression, D denotes donor, A denotes acceptor, and H denotes the transferring proton(s). The terms inside the square brackets refer to the state: $[\mathrm{DH}\ldots\mathrm{A}^\bullet]$ is the reactant state and $[\mathrm{D}^\bullet\ldots\mathrm{HA}]$ is the product state, as defined by the position of the transferring H, which dictates the localization of the transferring electron. The subscripts refer to the geometry at which the energy is calculated, where "reac" is the equilibrium reactant geometry and "prod" is the equilibrium product geometry. Thus, $[\mathrm{DH}\ldots\mathrm{A}^\bullet]_\mathrm{reac}$ and $[\mathrm{D}^\bullet\ldots\mathrm{HA}]_\mathrm{prod}$ are the energies of the reactant and product at their equilibrium geometries. $[\mathrm{DH}\ldots\mathrm{A}^\bullet]_\mathrm{prod}$ ($[\mathrm{D}^\bullet\ldots\mathrm{HA}]_\mathrm{reac}$) is the energy associated with the product (reactant) equilibrium geometry for all atoms except the transferring H, which is optimized on the donor (acceptor) to localize the electron and proton on the donor (acceptor). To ensure that the proton remains on the donor or acceptor, these optimizations and energies were computed for the two separated fragments of the hydrogen-bonded complex. The equilibrium reactant and product geometries were optimized in solution, but the optimization of the H and the calculation of these energies were performed in the gas phase, and the energies correspond to only the electronic energy without any additional corrections.

The calculation of vibronically nonadiabatic PCET rate constants also requires the proton potential energy curves and associated proton vibrational wavefunctions and energy levels for the reactant and product diabatic electronic states. As mentioned above, these rate constants must be computed at different values of the proton donor-acceptor distance R for EPT reactions. The general procedure for obtaining the proton potential energy curves for EPT reactions is as follows:

1. In the reactant equilibrium geometry, define R_{eq} as the proton donor-acceptor distance (i.e., the distance between the two oxygen atoms between which the proton is transferred).
2. Starting with the reactant equilibrium geometry, perform constrained geometry optimizations in solution for a series of evenly spaced R values (i.e., freeze the donor and acceptor oxygen atoms during the optimization, ensuring that the transferring H remains on its donor).
3. Follow the same procedure for the product state.
4. For each R value, superimpose the proton donor and acceptor and then average the Cartesian coordinates for all atoms to obtain an average geometry. For each of these average geometries, optimize the H on the donor and then on the acceptor in solution, H_r and H_p, and define the proton transfer coordinate to be the axis connecting these two positions.
5. For each R value, obtain the diabatic proton potential energy curves by performing constrained DFT (CDFT) calculations at uniform intervals along the proton transfer coordinate for the average geometry. In the CDFT calculations, the spin is localized on the donor or acceptor molecule to generate the reactant or product diabatic state energy.

The overall rate constant was obtained using the thermal averaging procedure in Eq. 5-2, where the rate constant is calculated for a series of different values of R weighted by the probability distribution function $P(R)$. In this case, $P(R)$ was not assumed to be Gaussian but rather was calculated as $P(R) = \exp(-U(R)/k_B T)$, where $U(R)$ is the energy of the reactant geometry for distance R generated from the constrained optimizations described in Step 2 (Figure 5.3)

The E2PT system has two proton transfer reactions and therefore two proton donor-acceptor distances, $R1$ and $R2$. As mentioned above, $R1$ and $R2$ are changed simultaneously by the same increment δR, and in the constrained geometry optimizations both proton donor-acceptor distances are constrained. In this case, In this case, the constrained geometry optimizations were performed for only the reactant state because it was not possible to generate average geometries in a consistent manner. Thus, for each reactant geometry corresponding to a set of $R1$ and $R2$ values, a two-dimensional proton potential energy surface was generated following a procedure analogous to that described for the EPT system. The two proton coordinates correspond to one proton transferring intermolecularly between the two oxygen atoms, analogous to the EPT system, and one proton transferring intramolecularly from the oxygen to the nitrogen. In this case, P(R) was assumed to be Gaussian with the form

$$P(R) = \frac{\exp[-k_{\mathrm{eff}}(R-\overline{R})^2/2k_B T]}{\int_{-\infty}^{\infty}\exp[-k_{\mathrm{eff}}(R-\overline{R})^2/2k_B T]dR} \tag{5-4}$$

Here, $\overline{R} = \overline{R1} + \overline{R2}$ = 2.79 + 2.64 = 5.43 Å is associated with the equilibrium ′donor-acceptor distances for the reactant, and k_{eff} = 0.01 au (hartrees.bohr^{-2}) is the effective force constant, which obtained by projecting the normal modes of the molecule in the reactant state onto $R1$ and $R2$ using the procedure described in Ref. [12-13]

After the proton potential energy surfaces were calculated and spline-interpolated for each proton donor-acceptor distance or pair of distances, the proton vibrational wavefunctions were computed numerically. The resulting proton vibrational wavefunctions were used to calculate the overlap integrals and energy levels in the vibronically nonadiabatic rate constant expression.

5.3. Results

5.3.1. EPT system

The parameters for the EPT system are given in Table 5.1. Note that this reaction is highly exoergic, and therefore excited proton vibrational states contribute significantly to the PCET rate constant. Table 5.2 provides an analysis of the contributions to the PCET rate constant at the dominant proton donor-acceptor distance, which is 2.60 Å for H and 2.58 Å for D. Note that the dominant proton donor-acceptor distance is typically shorter than the equilibrium distance because the overlap increases significantly as the distance decreases. Figure 5.4 depicts the proton potential energy curves calculated for the reactant and product diabatic states for each proton donor-acceptor distance. Figure 5.5 depicts the proton vibrational wavefunctions associated with the pairs of reactant/product vibronic states with the greatest contributions to the rate constant at the dominant proton donor-acceptor distances for hydrogen and deuterium. The contributions from excited proton vibrational states are associated with relatively large overlap integrals, therefore leading to a moderate KIE of 2.5 that is in good agreement with the experimental value of 2.81. Finally, an analysis of the dependence of the KIE on the total reorganization energy and the driving force is given in Figure 5.6

5.3.2. E2PT system

The parameters for the E2PT system are given in Table 5.3. This reaction is also highly exoergic, and therefore excited proton vibrational states contribute significantly to the E2PT rate constant. Table 5.4 provides an analysis of the contributions to the PCET rate constant at the dominant proton donor-acceptor distances. Figures 5.7 and 5.8 depict the two-dimensional proton vibrational wavefunctions associated with the dominant pairs of reactant/product vibronic states at the dominant proton donor-acceptor distances for H and D, respectively. The dominant contributions to the E2PT rate constant arise from even more highly excited states than for the EPT system. These excited two-dimensional proton vibrational states are associated with somewhat larger overlap integrals, therefore leading to a lower KIE for E2PT than for EPT. Specifically, the calculated KIE decreases to 1.7, which is lower than the KIE for the EPT system but is somewhat higher than the experimentally measured value. Given that these parameters were obtained by approaches that are only qualitatively accurate, it is meaningful to examine the dependence of the KIE on the total reorganization energy and the driving force, as in Figure 5.9. Altering these parameters by a few kcal/mol leads to good agreement with the experimental value of 1.0. Decreasing the value of k_{eff} was also found to lower the KIE (Figure 5.10) This study is an illustration that the KIE can be unity even when proton transfer occurs. The explanation for this KIE of unity is the dominant contributions from excited proton vibrational states to the PCET rate constant, and these contributions are dominant mainly because of the exoergicity (i.e., negative driving force) of the overall PCET reaction.

5.4. Figures

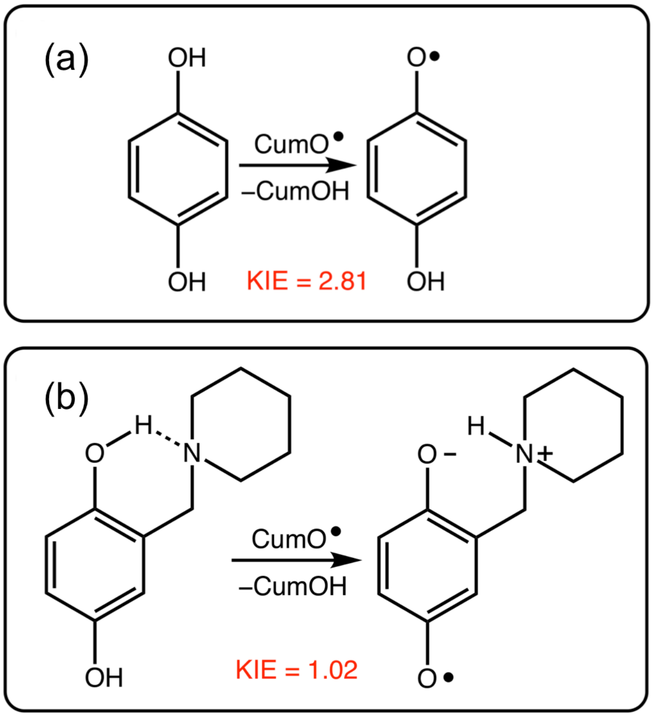

Figure 5.1. (a) **1**-H_2, EPT system and (b) **2**-H_2, E2PT system. These systems transfer an electron and a proton to a hydrogen-bonded CumO$^{\bullet}$ species, where **1**-H_2 undergoes EPT and **2**-H_2 undergoes E2PT involving intramolecular proton transfer as well as intermolecular proton transfer.

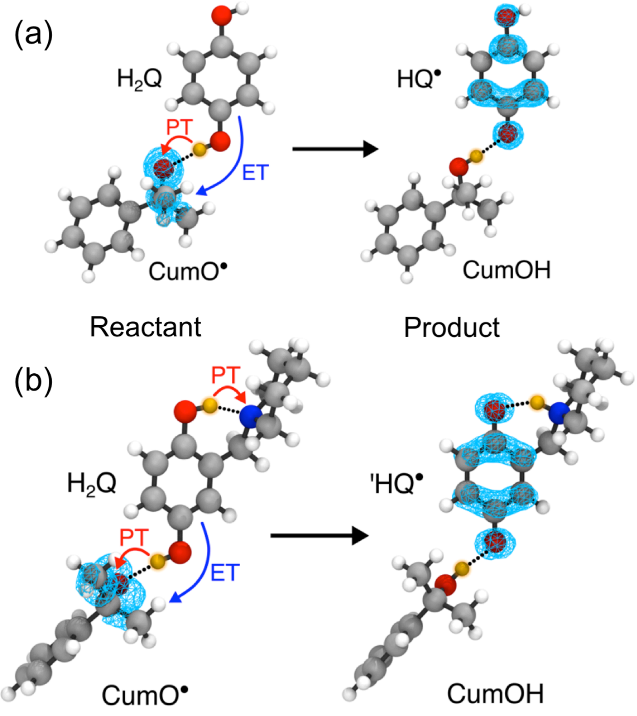

Figure 5.2. (a) **1**-H_2 reactant and product, (b) **2**-H_2 reactant and product.

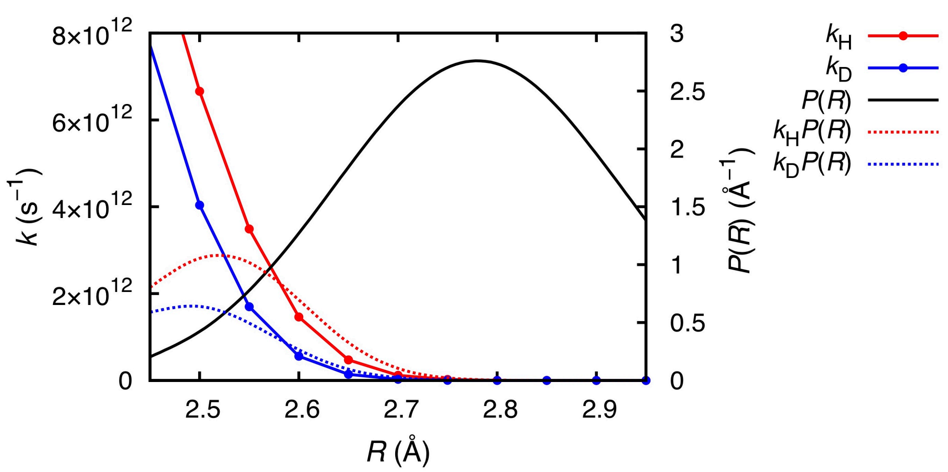

Figure 5.3. Rate constants for H and D, *P*(*R*), and the scaled product of these quantities versus *R* for the EPT system. This plot shows that values of R greater than around 2.8 Å do not contribute to the PCET rate constant.

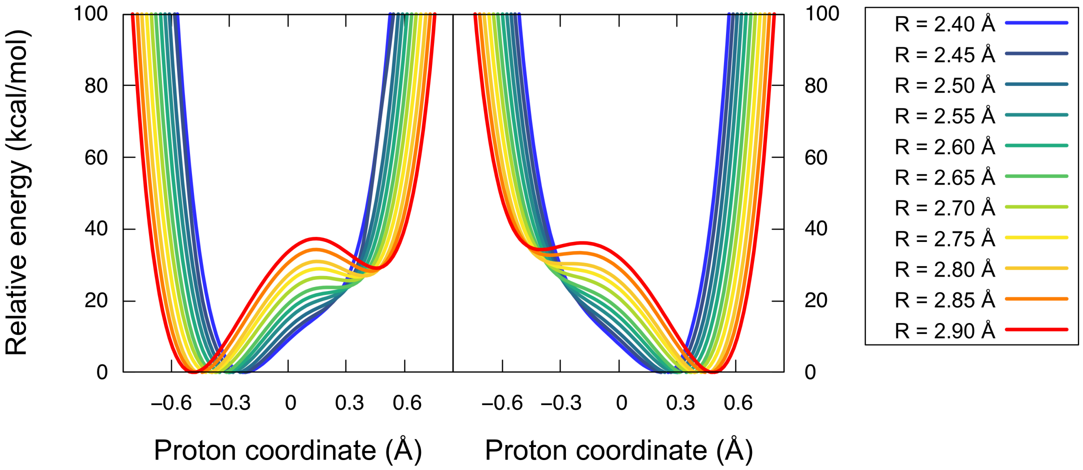

Figure 5.4. Proton potential energy curves for the reactant (left) and product (right) diabatic states. The proton coordinate at 0 Å corresponds to the proton positioned at the midpoint of the proton donor and acceptor. The minima for all curves are individually set to zero energy.

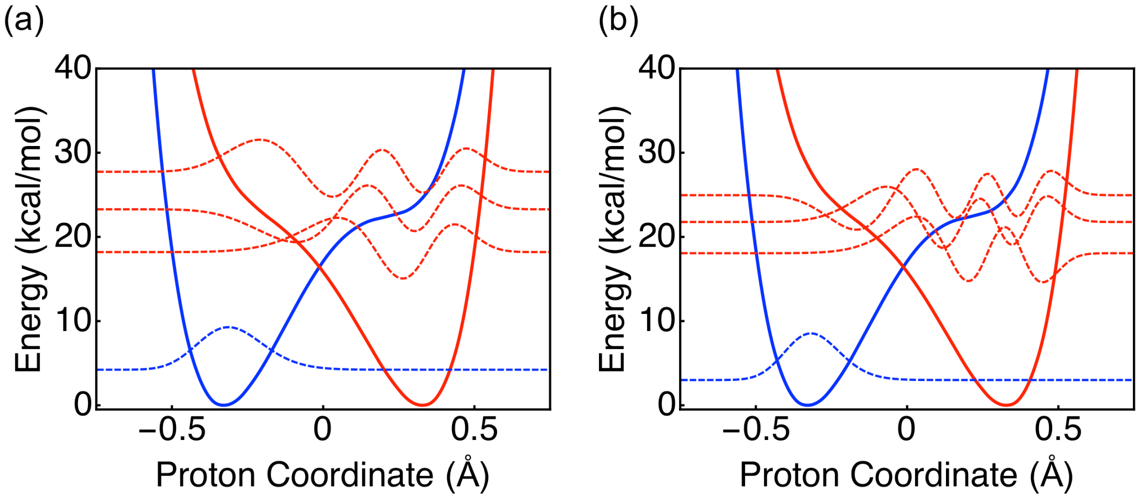

Figure 5.5. (a) H wavefunctions at dominant *R* and (b) D wavefunctions at dominant *R*. The thick red and blue curves represent the reactant and product diabatic state proton potentials, respectively. Note that the product potential and the associated proton vibrational wavefunctions and energy levels are shifted upward in energy by $-\Delta G^{o}$ = 24.56 kcal/mol.

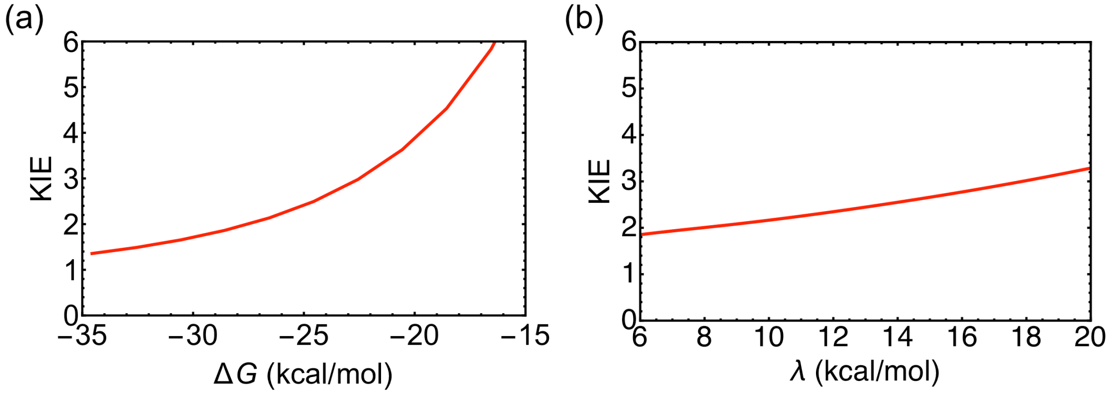

Figure 5.6. KIE versus (a) the reaction free energy ΔG^{o} with λ = 13.49 kcal/mol and (b) the total reorganization energy λ with ΔG^{o} = –24.56 for the EPT system, **1**-H_2.

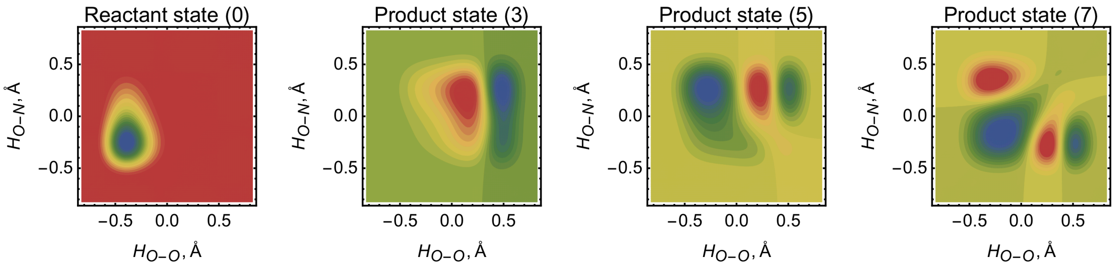

Figure 5.7. Hydrogen vibrational wavefunctions for reactant and product which have maximum contributions to the overall rate constant for H transfer at dominant donor-acceptor distance, $R_{\text{O–O}}$ = 2.74 Å and $R_{\text{O–N}}$ = 2.69 Å for the E2PT system, **2**-H_2. X and Y axes represent proton coordinate between O–O and O–N bonds, respectively. 0 on either axis means the transferring proton is at the midpoint between the two atoms.

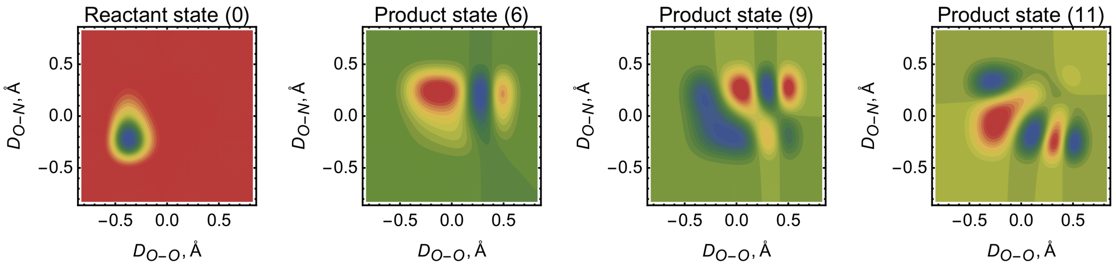

Figure 5.8. Deuterium vibrational wavefunctions for reactant and product which have maximum contributions to the overall rate constant for D transfer at dominant donor-acceptor distance, $R_{O–O}$ = 2.69 Å and $R_{O–N}$ = 2.64 Å for the E2PT system, **2**-H_2. X and Y axes represent proton coordinate between O–O and O–N bonds, respectively. 0 on either axis means the transferring proton is at the midpoint between the two atoms.

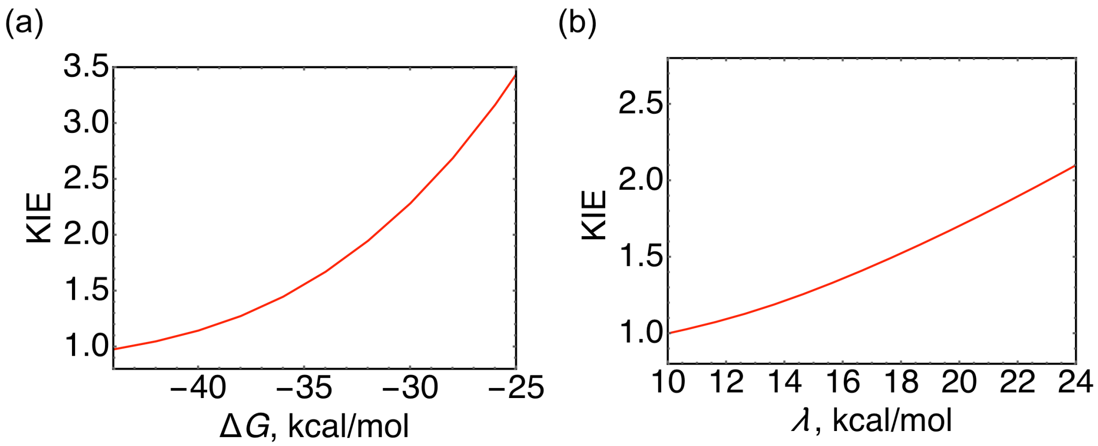

Figure 5.9. KIE versus (a) the reaction free energy ΔG^{o} with λ = 19.65 kcal/mol and (b) the total reorganization energy λ with ΔG^{o} = –33.94 kcal/mol for the E2PT system, **2**-H_2. k_{eff} = 0.01 a.u.

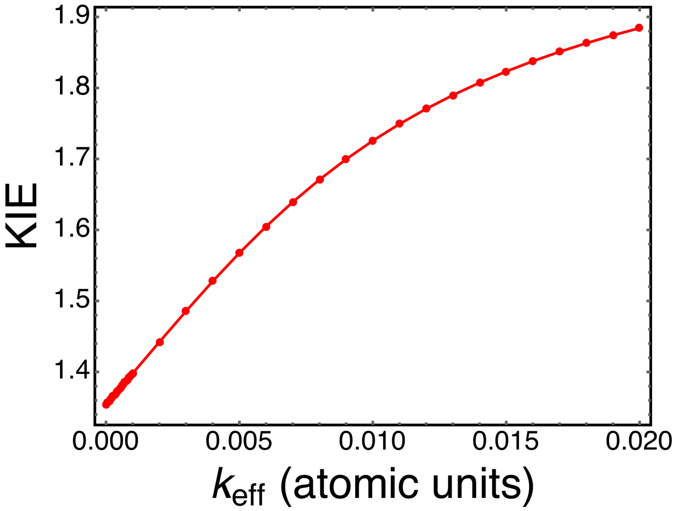

Figure 5.10. KIE versus the effective force constant k_{eff} associated with the probability distribution for the proton donor-acceptor distances at ΔG^{o} = –33.94 kcal/mol and λ = 19.65 kcal/mol for the E2PT system, **2**-H_2.

5.5. Tables

Table 5.1. Parameters used in PCET rate constant expression and resulting KIE value for the EPT (**1**-H_2) system. The parameters are as follows: ΔG^o is the driving force (i.e., reaction free energy), λ_{in} is the inner-sphere reorganization energy, λ_{out} is the outer-sphere reorganization energy, and λ is the total reorganization energy, all in units of kcal/mol

EPT	ΔG^o	λ_{in}	λ_{out}	λ	KIE
Calc.	–24.56	10.88	2.61	13.49	2.5
Expt.	--	--	--	--	2.81

Table 5.2. Pairs of reactant/product vibronic states with maximum percentage contribution to the PCET rate constant for **1**-H_2 at the dominant proton donor-acceptor distance, 2.60 Å for H and 2.55 Å for D

Proton				Deuterium			
States [a]	% cont.	$\Delta G^{\ddagger}_{\mu\nu}$ [b]	$S^2_{\mu\nu}$ [c]	States [a]	% cont.	$\Delta G^{\ddagger}_{\mu\nu}$ [b]	$S^2_{\mu\nu}$ [c]
(0,2)	35.096	0.166	1.6417×10^{-2}	(0,3)	14.129	0.304	3.1810×10^{-3}
(0,3)	56.331	1.207	1.5291×10^{-1}	(0,4)	47.746	1.116	4.2304×10^{-2}
(0,4)	7.291	2.911	3.5082×10^{-1}	(0,5)	32.679	2.219	1.8654×10^{-1}

[a] Pairs of reactant/product vibronic states are given as (μ of reactant, ν of product).

[b] $\Delta G^{\ddagger}_{\mu\nu} = (\Delta G_{\mu\nu} + \lambda)^2 / 4\lambda$, in kcal/mol.

[c] Square of overlap integral between state μ of reactant and state ν of product.

Table 5.3. Parameters used in PCET rate constant expression and resulting KIE value for the EPT (**2**-H_2) system. The parameters are as follows: ΔG^o is the driving force (i.e., reaction free energy), λ_{in} is the inner-sphere reorganization energy, λ_{out} is the outer-sphere reorganization energy, and λ is the total reorganization energy, all in units of kcal/mol

E2PT	ΔG^o	λ_{in}	λ_{out}	λ	KIE
Calc.	–33.98	14.28	5.36	19.65	1.7
Expt.	--	--	--	--	1.02

Table 5.4. Pairs of reactant/product vibronic states with maximum percentage contribution to the PCET rate constant for **2**-H_2 at the dominant proton donor-acceptor distances, $R_{O–O}$ = 2.74 Å and $R_{O–N}$ = 2.69 Å for H and $R_{O–O}$ = 2.69 Å and $R_{O–N}$ = 2.64 Å for D

Proton				Deuterium			
States [a]	% cont.	$\Delta G^{\ddagger}_{\mu\nu}$ [b]	$S^2_{\mu\nu}$ [c]	States [a]	% cont.	$\Delta G^{\ddagger}_{\mu\nu}$ [b]	$S^2_{\mu\nu}$ [c]
(0,3)	8.96	0.045	2.314×10^{-2}	(0,6)	18.82	0.014	4.2207×10^{-2}
(0,5)	55.77	0.1397	1.689×10^{-1}	(0,9)	42.88	0.305	1.5711×10^{-1}
(0,7)	26.19	0.802	2.426×10^{-1}	(0,11)	21.94	0.780	1.7924×10^{-1}

[a] Pairs of reactant/product vibronic states are given as (μ of reactant, ν of product).

[b] $\Delta G^{\ddagger}_{\mu\nu} = (\Delta G_{\mu\nu} + \lambda)^2 / 4\lambda$, in kcal/mol.

[c] Square of overlap integral between state μ of reactant and state ν of product.

5.6. References

1. Lovley, D. R.; Coates, J. D.; Blunt-Harris, E. L.; Phillips, E. J.; Woodward, J. C., Humic substances as electron acceptors for microbial respiration. *Nature* **1996,** *382* (6590), 445.
2. Lahtinen, R.; Fermın, D. J.; Kontturi, K.; Girault, H. H., Artificial photosynthesis at liquid-liquid interfaces: photoreduction of benzoquinone by water soluble porphyrin species. *J. Electroanal. Chem* **2000,** *483* (1-2), 81-87.
3. Soudackov, A.; Hammes-Schiffer, S., Derivation of rate expressions for nonadiabatic proton-coupled electron transfer reactions in solution. *J. Chem. Phys.* **2000,** *113* (6), 2385-2396.
4. Soudackov, A.; Hatcher, E.; Hammes-Schiffer, S., Quantum and dynamical effects of proton donor-acceptor vibrational motion in nonadiabatic proton-coupled electron transfer reactions. *J. Chem. Phys.* **2005,** *122* (1), 014505.
5. Cossi, M.; Rega, N.; Scalmani, G.; Barone, V., Energies, structures, and electronic properties of molecules in solution with the C-PCM solvation model. *J. Comput. Chem.* **2003,** *24* (6), 669-681.
6. Bondi, A., van der Waals volume and radii. *J. Phys. Chem.* **1964,** *68* (3), 441.
7. Floris, F. M.; Tomasi, J.; Ahuir, J. L. P., Dispersion and repulsion contributions to the solvation energy: Refinements to a simple computational model in the continuum approximation. *J. Comput. Chem.* **1991,** *12* (7), 784-791.
8. Pierotti, R. A., A scaled particle theory of aqueous and nonaqueous solutions. *Chem. Rev.* **1976,** *76* (6), 717-726.
9. Newton, M.; Basilevsky, M.; Rostov, I., A frequency-resolved cavity model (FRCM) for treating equilibrium and non-equilibrium solvation energies: 2: Evaluation of solvent reorganization energies. *Chem. Phys.* **1998,** *232* (1-2), 201-210.
10. Basilevsky, M.; Rostov, I.; Newton, M., A frequency-resolved cavity model (FRCM) for treating equilibrium and non-equilibrium solvation energies. *Chem. Phys.* **1998,** *232* (1-2), 189-199.
11. Breneman, C. M.; Wiberg, K. B., Determining atom-centered monopoles from molecular electrostatic potentials. The need for high sampling density in formamide conformational analysis. *J. Comput. Chem.* **1990,** *11* (3), 361-373.
12. Auer, B.; Fernandez, L. E.; Hammes-Schiffer, S., Theoretical analysis of proton relays in electrochemical proton-coupled electron transfer. *J. Am. Chem. Soc* **2011,** *133* (21), 8282-8292.
13. Huynh, M. T.; Mora, S. J.; Villalba, M.; Tejeda-Ferrari, M. E.; Liddell, P. A.; Cherry, B. R.; Teillout, A.-L.; Machan, C. W.; Kubiak, C. P.; Gust, D.; Moore, T. A.; Hammes-Schiffer, S.; Moore, A. L., Concerted one-electron two-proton transfer processes in models inspired by the Tyr-His couple of photosystem II. *ACS Cent. Sci.* **2017,** *3* (5), 372-380.

APPENDIX A: Supporting Information for Chapter 2[§]

Because the formation of an Fe^0 intermediate in the catalytic cycle is unusual, we analyzed the structures of the $[Fe^Ipy]^-$ and $[Fe^0py]^{2-}$ species (Figure A.1) in more detail. Table A.7 provides the relative free energies of the optimized doublet and quartet states of $[Fe^Ipy]^-$ and the relative free energies of the optimized singlet and triplet states of the square pyramidal and trigonal bipyramidal $[Fe^0py]^{2-}$. The doublet $[Fe^Ipy]^-$ state, in which the unpaired spin is localized on the Fe center, is much more thermodynamically stable than the quartet state. For $[Fe^0py]^{2-}$, the singlet square pyramidal state is more thermodynamically stable than the triplet square pyramidal state and both trigonal bipyramidal states. In the doublet and triplet square pyramidal states, the unpaired electrons are primarily localized on the Fe center, without significant delocalization onto the ligands. Moreover, the trigonal bipyramidal structure is highly unfavorable for the $[Fe^0py]^{2-}$ species.

[§] Reproduced with permission from:
Harshan, A. K.; Solis, B. H.; Winkler, J. R.; Gray, H. B.; Hammes-Schiffer, S., *Inorg. Chem.* **2016,** *55* (6), 2934-2940. Copyright 2016 American Chemical Society

A.1. Figure

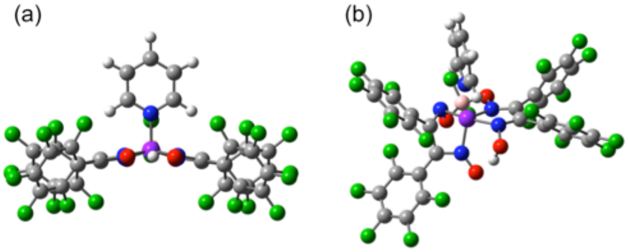

Figure A.1. DFT/BP86 optimized structures for (a) square pyramidal and (b) trigonal bipyramidal $[Fe^0py]^{2-}$.

A.2. Tables

Table A.1. Comparison of bond lengths and angles for intermediates of **B** optimized in gas phase and dichloromethane solution [a]

	$[Fe^{II}py_2]^0$		$[Fe^{I}py]^{-}$		$[Fe^{0}py]^{2-}$	
Bond length or angle	Solution	Gas	Solution	Gas	Solution	Gas
Fe-N1(py)	1.99	2.00	1.99	1.99	1.90	1.90
Fe-N2(py)	2.01	2.02	-	-	-	-
Fe-N(1)	1.88	1.89	1.87	1.87	1.85	1.85
Fe-N(2)	1.89	1.89	1.87	1.88	1.85	1.86
Fe-N(3)	1.89	1.89	1.86	1.87	1.86	1.86
Fe-N(4)	1.90	1.90	1.87	1.88	1.86	1.87
N(1)-Fe-N(2)	97.3	96.8	92.4	92.1	93.8	93.1
N(2)-Fe-N(3)	81.9	82.2	81.4	81.7	82.0	82.4
N(3)-Fe-N(4)	97.8	97.6	93.1	93.0	94.5	94.3
N(4)-Fe-N(1)	82.7	83.1	81.9	82.4	82.4	83.0
N(3)-N(4)-N(1)-Fe	–2.7	–2.6	–17.0	–17.5	–13.8	–13.8

[a] Calculations performed with BP86 functional with 6-31+G(d,p) basis set for central part of molecule and 6-31G basis set for C_6F_6 groups and axial pyridine ligands. Bond lengths are given in angstroms and angles are given in degrees.

Table A.2. Spin density at the Fe center, ρ_{Fe}, and relative free energies for different spin states of intermediates [a]

Catalyst	#pyridines	Charge	S	$<S^2>$	ρ_{Fe}	ΔG (kcal/mol)
A	2	0	0	0.00 (0.00)	0.00 (0.00)	0.00 (0.00)
	2	0	1	2.01 (2.02)	0.70 (0.98)	19.90 (23.83)
	1	0	0	0.00 (0.00)	0.00 (0.00)	0.00 (0.00)
	1	0	1	2.03 (2.04)	1.68 (1.93)	–4.17 (–7.07)
	2	−1	1/2	0.75 (0.79)	–0.07 (0.18)	0.00 (0.00)
	2	−1	3/2	3.76 (3.78)	0.91 (1.00)	26.70 (22.61)
	1	−1	1/2	0.80 (1.32)	1.08 (1.82)	0 (0)
	1	−1	3/2	3.78 (3.77)	1.80 (1.91)	17.76 (12.04)
	2	−2	0	0.00	0.00	0.00
	2	−2	1	2.01	0.12	9.25
	1	−2	0	0.00	0.00	0.00
	1	−2	1	2.05	1.59	15.42
	0	−2	0	0.00	0.00	0.00
	0	−2	1	2.04	1.55	–8.97
B	2	0	2	0.00 (0.00)	0.00 (0.00)	0.00 (0.00)
	2	0	2	2.01(2.03)	0.63 (0.99)	17.84 (23.27)
	1	0	1	0.00 (0.00)	0.00 (0.00)	0.00 (0.00)
	1	0	1	2.04 (2.04)	1.73 (1.96)	–4.84 (–8.00)
	1[b]	1	0	0.00 (0.00)	0.00 (0.00)	0.00 (0.00)
	1[b]	1	1	2.04 (2.04)	1.71 (1.95)	–3.26 (–7.18)
	2	−1	1/2	0.75	–0.06	0.00
	2	−1	3/2	3.79	1.73	21.15
	1	−1	1/2	0.79	1.02	0.00
	1	−1	3/2	3.78	1.84	17.81
	2	−2	0	0.00	0.00	0.00
	2	−2	1	2.01	0.05	9.26
	1	−2	0	0.00	0.00	0.00
	1	−2	1	2.07	1.54	16.32
	0	−2	0	0.00	0.00	0.00
	0	−2	1	2.04	1.58	–7.78

[a] Calculations performed with BP86 functional with 6-31+G(d,p) basis set for central part of molecule and 6-31G basis set for C_6F_6 groups and axial pyridine ligands. B3P86 results for selected intermediates are given in parentheses.

[b] Ligand-protonated species.

Table A.3. Estimated relative free Energies for pyridine dissociation for relevant states of **A** and **B** in dichloromethane solution [a]

Complex	Charge	Reactant	*S*	Product	*S*	Δ*G*
A	0	$Fe^{II}py_2$	0	$Fe^{II}py$	1	9.60
	–1	$Fe^{I}(gly)^{\bullet}py_2$	1/2	$Fe^{I}py$	1/2	–11.43
	–2	$Fe^{0}py_2$	0	$Fe^{0}py$	0	–23.63
	–2	$Fe^{0}py$	0	Fe^{0}	1	7.97
B	0	$Fe^{II}py_2$	0	$Fe^{II}py$	1	9.46
	–1	$Fe^{I}(gly)^{\bullet}py_2$	1/2	$Fe^{I}py$	1/2	–10.62
	–2	$Fe^{0}py_2$	0	$Fe^{0}py$	0	–24.61
	–2	$Fe^{0}py_2$	0	Fe^{0}	1	8.24

[a] Calculations performed with BP86 functional with 6-31+G(d,p) basis set for central part of molecule and 6-31G basis set for C_6F_6 groups and axial pyridine ligands. Free energies are given in kcal/mol, and the product free energy is the sum of the free energy of the complex and a solvated py ligand. Basis set superposition error (BSSE) corrections were not included.

Table A.4. Difference in pK_a associated with protonation at the ligand versus protonation at the metal center for **B** with different functionals [a]

Functional	BP86	B3P86	M06L	ωB97XD[b]
ΔpK_a [c]	2.70	6.34	4.24	–1.08

[a] Calculations presented in this table were performed with the 6-311+G(d,p) basis set with Cl atoms substituted for C_6F_5 groups, which have similar Hammett constant.[1]

[b] The trends in relative pK_a's for all functionals except ωB97XD agree well. Severe spin contamination observed for the doublet state with the ωB97XD functional is most likely responsible for this discrepancy.

[c] ΔpK_a = pK_a of $[\mathrm{Fe}^{\mathrm{I}}\mathrm{py..}\mathbf{H}]^0$ – pK_a of $[\mathrm{Fe}^{\mathrm{III}}\mathbf{H}\mathrm{py}]^0$

Table A.5. Relative pK_a values for **A** and **B** [a]

A	Relative pK_a
[Fe^{III}**H**py]^0	−10.03
[Fe^{II}**H**py]$^-$	9.43
B	Relative pK_a
[Fe^{II}py$_2$…**H**]$^+$	−11.35
[Fe^{I}py…**H**]^0	0.00
[Fe^{III}**H**py]^0	−3.81
[Fe^{II}**H**py]$^-$	15.25
[Fe^{0}py…**H**]$^-$	12.16
[Fe^{III}**H**py…H]$^+$	−18.49
Fe^{III}Hpy…**H**]$^+$	−14.68
[Fe^{II}**H**py…H]^0	1.55
[Fe^{II}Hpy…**H**]^0	−1.54

[a] Calculations were performed with BP86 functional with 6-31+G(d,p) basis set for central part of molecule and 6-31G basis set for C_6F_6 groups and axial pyridine ligands. These pK_a values are plotted in Figure 2.4. The bold **H** indicates the acidic proton, '…H' indicates a protonated ligand, and FeH indicates a metal hydride. [Fe^{I}py…**H**]^0 for **B** is the reference pK_a, and all other values are calculated relative to this value.

Table A.6. Spin properties for protonated species of **A** and **B** [a]

Complex	Protonated	S	$\langle S^2 \rangle$	ρ_{Fe}
A	$[\mathrm{Fe^{III}Hpy}]^0$	1/2	0.76	0.87
	$[\mathrm{Fe^{II}Hpy}]^-$	0	0.00	0.00
B	$[\mathrm{Fe^{III}Hpy}]^0$	1/2	0.76	0.87
	$[\mathrm{Fe^{II}Hpy}]^-$	0	0.00	0.00
	$[\mathrm{Fe^{II}py_2 \ldots H}]^+$	0	0.00	0.00
	$[\mathrm{Fe^{II}py \ldots H}]^+$	1	2.04	1.72
	$[\mathrm{Fe^{II}(gly)^{\bullet}py_2 \ldots H}]^0$	1/2	0.76	–0.06
	$[\mathrm{Fe^{I}py \ldots H}]^0$	1/2	0.81	1.16
	$[\mathrm{Fe^{0}py \ldots H}]^-$	0	0.00	0.00
	$[\mathrm{Fe^{III}Hpy \ldots H}]^+$	1/2	0.77	0.89
	$[\mathrm{Fe^{II}Hpy \ldots H}]^0$	0	0.00	0.00

[a] Calculations were performed with BP86 functional with 6-31+G(d,p) basis set for central part of molecule and 6-31G basis set for C_6F_6 groups and axial pyridine ligands. Fe…H indicates a protonated ligand, and FeH indicates a metal hydride.

Table A.7. Spin densities and relative free energies for Fe^I and Fe^0 states of **B** [a]

Species	S	ρ_{Fe}	ΔG
$[Fe^Ipy]^-$	1/2	1.02	0.00 [b]
	3/2	1.84	17.81
$[Fe^0py]^{2-}$	0	0.00	0.00 [c]
	1	1.46	16.32
tbp-$[Fe^0py]^{2-}$ [d]	0	0.00	50.78
	1	1.23	50.56

[a] Calculations performed with BP86 functional. Free energies given in kcal/mol.

[b] Reference free energy for Fe^I species.

[c] Reference free energy for Fe^0 species.

[d] *tbp*=trigonal bipyramidal. All other species in this table are square pyramidal.

Table A.8. Parameters used for CV simulations of **A** using DigiElch7 [a]

#	Charge Transfer Reaction	E° (V vs SCE)	α	K_S (cm/s)
1	$[Fe^{II}py_2]^0 + e = [Fe^{II}(gly)^{\bullet}py_2]^-$	−0.71	0.5	10000
2	$[Fe^{I}py]^- + e = [Fe^{0}py]^{2-}$	−0.94	0.5	10000
3	$[Fe^{II}py]^0 + e = [Fe^{II}py]^-$	*0.29*	0.5	10000
4	$[Fe^{III}Hpy]^0 + e = [Fe^{II}Hpy]^-$	*0.21*	0.5	10000
	Chemical Reaction	K_{eq}	k_f	k_b
5	$[Fe^{II}py_2]^0 = [Fe^{II}py]^0 + py$	*9.1689E−08*	0.2 [b]	2.1813E+0
6	$[Fe^{II}(gly)^{\bullet}py_2]^- = [Fe^{I}py]^- + py$	7.29E+09	5 [b]	6.8591E−1
8	$py + HA = pyH^+ + A^-$	0.003	1E+07 [c]	3.33E+09
9	$[Fe^{0}py]^{2-} + HA = [Fe^{II}Hpy]^- + A^-$	1	500 [c]	500
10	$[Fe^{II}Hpy]^- + HA = [Fe^{II}H_2py]^0 +$	1000	1E+07 [c]	10000
11	$[Fe^{II}H_2py]^0 + py = [Fe^{II}py_2]^0 + H_2$	1000	1E+07 [c]	10000
12	$[Fe^{I}py]^- + HA = [Fe^{III}Hpy]^0 + A^-$	3.50E−20	0.1 [c]	2.8558E+1

[a] Parameters that were fixed to the DFT/BP86 calculated values are given in italics. All other parameters except the reduction potentials of the first two charge transfer reactions were free to fit to the experimental CVs. When available, the DFT/BP86 calculated values are given in parentheses. The trend in the magnitudes of the forward rate constants was constrained to be the same as the trend in the magnitudes of the equilibrium constants for the catalyst protonation reactions so that larger forward rate constants are associated with larger equilibrium constants for these reactions. All values are given for dichloromethane solution, with concentrations [**A**] = 0.5 mM and [TFA] = 0-10 mM. The scan rate was 100 mV/s.

[b] Unit of k_f is s^{-1} (first-order reaction), and unit of k_b is $M^{-1}s^{-1}$ (second-order reaction).

[c] Unit of k_f is $M^{-1}s^{-1}$ (second-order reaction), and unit of k_b is $M^{-1}s^{-1}$ (second-order reaction).

Table A.9. Parameters used for CV simulations of **B** using DigiElch7 [a]

#	Charge Transfer Reaction	E^{o} (V vs SCE)	α	Ks (cm/s)
1	$[\mathrm{Fe^{II}py_2}]^0 + \mathrm{e} = [\mathrm{Fe^{II}(gly)^{\bullet}py_2}]^-$	*−0.92*	0.5	10000
2	$[\mathrm{Fe^{II}py}]^0 + \mathrm{e} = [\mathrm{Fe^{I}py}]^-$	*−0.05*	0.5	10000
3	$[\mathrm{Fe^{I}py}]^- + \mathrm{e} = [\mathrm{Fe^{0}py}]^{2-}$	*−1.17*	0.5	10000
4	$[\mathrm{Fe^{II}py\ldots H}]^0 + \mathrm{e} = [\mathrm{Fe^{I}py\ldots H}]^-$	*0.73*	0.5	10000
5	$[\mathrm{Fe^{I}py\ldots H}]^0 + \mathrm{e} = [\mathrm{Fe^{0}py\ldots H}]^-$	*−0.45*	0.5	10000
6	$[\mathrm{Fe^{III}Hpy}]^0 + \mathrm{e} = [\mathrm{Fe^{II}Hpy}]^-$	*−0.04*	0.5	10000
7	$[\mathrm{Fe^{III}Hpy\ldots H}]^+ + \mathrm{e} = [\mathrm{Fe^{II}Hpy\ldots H}]^0$	*0.74*	0.5	10000
	Chemical Reaction	K_{eq}	k_{f}	k_{b}
8	$[\mathrm{Fe^{II}py_2}]^0 = [\mathrm{Fe^{II}py}]^0 + \mathrm{py}$	*1.1556E−07*	0.002 [b]	17307
9	$[\mathrm{Fe^{II}(gly)^{\bullet}py_2}]^- = [\mathrm{Fe^{I}py}]^- + \mathrm{py}$	5.84E+007 (6.12E+07)	10 [b]	1.71E−07
10	$[\mathrm{Fe^{I}py}]^- + \mathrm{HA} = [\mathrm{Fe^{I}py\ldots H}]^0 + \mathrm{A}^-$	10	10000 [c]	1000
11	$[\mathrm{Fe^{0}py}]^{2-} + \mathrm{HA} = [\mathrm{Fe^{0}py\ldots H}]^- + \mathrm{A}^-$	1.47E+013 (1.44E+13)	15000 [c]	1.018E−09
12	$[\mathrm{Fe^{I}py\ldots H}]^0 = [\mathrm{Fe^{III}Hpy}]^0$	0.00014657 (0.000156)	0.1 [d]	682.27
13	$[\mathrm{Fe^{0}py\ldots H}]^- = [\mathrm{Fe^{II}Hpy}]^-$	*1245.1*	1 [d]	.0008
14	$\mathrm{py} + \mathrm{HA} = \mathrm{pyH}^+ + \mathrm{A}^-$	0.001	5E+06 [c]	5E+09
15	$[\mathrm{Fe^{II}Hpy}]^- + \mathrm{HA} = [\mathrm{Fe^{II}H_2py}]^0 + \mathrm{A}^-$	1000	12000 [c]	12
16	$[\mathrm{Fe^{II}H_2py}]^0 = [\mathrm{Fe^{II}py}]^0 + \mathrm{H_2}$	1000	10000 [b]	10
17	$[\mathrm{Fe^{0}py}]^{2-} + \mathrm{HA} = [\mathrm{Fe^{II}Hpy}]^- + \mathrm{A}^-$	1.83E+016 (1.79E+16)	16000 [c]	8.72E−13
18	$[\mathrm{Fe^{I}py}]^- + \mathrm{HA} = [\mathrm{Fe^{III}Hpy}]^0 + \mathrm{A}^-$	0.0014567 (1.56E−03)	1E−05 [c]	0.006823
19	$[\mathrm{Fe^{I}py\ldots H}]^0 + \mathrm{HA} = [\mathrm{Fe^{III}Hpy\ldots H}]^+ + \mathrm{A}^-$	2.7735E−18	1E−10 [c]	3.6056E+07
20	$[\mathrm{Fe^{0}py\ldots H}]^- + \mathrm{HA} = [\mathrm{Fe^{II}Hpy\ldots H}]^0 + \mathrm{A}^-$	*358.5*	11000 [c]	30.683
21	$[\mathrm{Fe^{II}Hpy\ldots H}]^0 + \mathrm{py} = [\mathrm{Fe^{II}py_2}]^0 + \mathrm{H_2}$	3.0054E+13	20000 [c]	6.6546E−10

[a] Parameters that were fixed to the DFT/BP86 calculated values are given in italics. All other parameters were free to fit to the experimental CVs. When available, the DFT/BP86 calculated values are given in parentheses. The trend in the magnitudes of the forward rate constants was constrained to be the same as the trend in the magnitudes of the equilibrium constants for the catalyst protonation reactions so that larger forward rate constants are associated with larger equilibrium constants for these reactions. All values are given for dichloromethane solution, with concentrations [**B**] = 0.5 mM and [TFA] = 0-10 mM. The scan rate was 100 mV/s.

[b] Unit of k_{f} is $\mathrm{s^{-1}}$ (first-order reaction), and the unit of k_{b} is $\mathrm{M^{-1}s^{-1}}$ (second-order reaction).

[c] Unit of k_{f} is $\mathrm{M^{-1}s^{-1}}$ (second-order reaction), and the unit of k_{b} is $\mathrm{M^{-1}s^{-1}}$ (second-order reaction).

[d] Unit of k_{f} is $\mathrm{s^{-1}}$ (first-order reaction), and the unit of k_{b} is $\mathrm{s^{-1}}$ (first-order reaction).

A.3. Coordinates and Energies of Optimized Structures

1. $[\mathrm{Fe^{II}py_2}]^0$, Complex **A**
E = -5792.67511971 hartrees

Fe	-0.00002800	0.03180500	-0.00551300
N	-1.40904700	-0.08017000	-1.25103700
O	-1.27782300	-0.11044200	-2.59426200
B	-0.00024600	0.51134800	-3.18131800
O	1.27719000	-0.11096300	-2.59451500
N	1.40870400	-0.08068300	-1.25131900
C	2.62137000	-0.26786000	-0.73582500
C	2.62311000	-0.24281400	0.72986100
N	1.41651500	-0.01989900	1.24331800
O	1.27625500	-0.08194100	2.58539500
B	0.00037000	0.55734600	3.16666500
O	-1.27582500	-0.08154800	2.58564800
N	-1.41633700	-0.01941700	1.24360200
C	-2.62311500	-0.24187700	0.73038300
C	-2.62168100	-0.26690200	-0.73530200
F	0.00055700	1.92089400	2.92464700
F	0.00044800	0.18624700	4.49425900
N	0.00031200	2.02851400	-0.03792200
C	-1.17310400	2.73376200	-0.04288000
C	1.17397200	2.73335200	-0.04314800
C	-1.20536200	4.13327800	-0.05262300
H	-2.09775600	2.16079300	-0.03315200
C	1.20671700	4.13285500	-0.05289500
H	2.09842300	2.16005300	-0.03364400
C	0.00080300	4.85410600	-0.05767200
H	-2.17273900	4.64047200	-0.05208900
H	2.17427100	4.63971200	-0.05258400
H	0.00099400	5.94705800	-0.06265300
N	-0.00037800	-2.00161100	0.04582000
C	-0.00071700	-2.72707200	-1.11780800
C	-0.00030700	-2.68053600	1.23845700
C	-0.00097600	-4.12888900	-1.11947100
H	-0.00078300	-2.16458600	-2.05085800
C	-0.00056200	-4.08075700	1.29626600
H	-0.00004500	-2.07778800	2.14684400
C	-0.00089600	-4.82359100	0.10205100
H	-0.00123700	-4.65638700	-2.07571700
H	-0.00049300	-4.57160800	2.27233700
H	-0.00109300	-5.91654900	0.12359500
F	-0.00045800	0.13217400	-4.50577500
F	0.00005800	1.88388000	-2.96352400
C	-3.83101300	-0.42491200	-1.56894600
C	-4.90645500	0.47994900	-1.47738800
C	-3.95289400	-1.46168700	-2.51548200
C	-6.04935500	0.37189200	-2.27781400
C	-5.07915900	-1.58935400	-3.33783100
C	-6.13287500	-0.66987300	-3.21495500
C	-3.81781300	-0.46667200	1.56985000
C	-4.24291600	0.48815500	2.51645700

C	-4.56583300	-1.65683300	1.48644900
C	-5.35027300	0.26992200	3.34513300
C	-5.68186700	-1.89867100	2.29641500
C	-6.07315800	-0.92862300	3.23225500
C	3.83046800	-0.42638600	-1.56970700
C	4.90643500	0.47784900	-1.47819400
C	3.95160300	-1.46309400	-2.51641200
C	6.04915000	0.36924500	-2.27881200
C	5.07766200	-1.59129100	-3.33896000
C	6.13192700	-0.67243700	-3.21611300
C	3.81790000	-0.46800600	1.56909200
C	4.56542500	-1.65847700	1.48565700
C	4.24359300	0.48674600	2.51551200
C	5.68153300	-1.90068100	2.29541100
C	5.35103800	0.26815100	3.34397600
C	6.07341500	-0.93069700	3.23106900
F	-7.17056100	-1.15115300	4.03758600
F	-6.38307100	-3.08549500	2.19298700
F	-4.16194000	-2.65604900	0.59915100
F	-5.74862400	1.22986000	4.25372200
F	-3.57424100	1.69983900	2.60932600
F	-7.25159900	-0.79153400	-4.01214400
F	-5.17182300	-2.62438000	-4.24721700
F	-7.07791600	1.28768400	-2.16545400
F	-4.81824900	1.55405700	-0.58885500
F	-2.95037600	-2.41636400	-2.61728400
F	2.94849600	-2.41714900	-2.61822300
F	5.16957900	-2.62623200	-4.24851800
F	7.25045400	-0.79462400	-4.01349700
F	7.07825900	1.28442500	-2.16647700
F	4.81900000	1.55185200	-0.58945800
F	4.16093400	-2.65763900	0.59857200
F	6.38223000	-3.08780400	2.19196100
F	7.17089700	-1.15359000	4.03619200
F	5.74997200	1.22802400	4.25237700
F	3.57544700	1.69872200	2.60838000

2. $[Fe^{II}py]^{0}$, Complex **A**
E = -5544.39550301

Fe	0.00008500	0.63939900	-0.01798100
N	-1.37254000	0.27871100	-1.26934600
O	-1.25662700	0.26180300	-2.61011000
B	-0.00018100	0.92770100	-3.17890900
O	1.25611400	0.26130100	-2.61036700
N	1.37231000	0.27815700	-1.26962600
C	2.54551900	-0.11126700	-0.75021200
C	2.55230000	-0.10344200	0.69585400
N	1.38070700	0.27726000	1.22520100
O	1.25653100	0.18711400	2.56325800
B	0.00044200	0.83162500	3.16284200
O	-1.25602400	0.18760900	2.56351500
N	-1.38042900	0.27779000	1.22548300
C	-2.55226900	-0.10247900	0.69636900

C	-2.54578400	-0.11028600	-0.74969600
F	0.00068600	2.19787700	2.90391400
F	0.00050900	0.47847300	4.48953100
N	0.00047200	2.65291100	0.02445300
C	-1.17882200	3.34225700	0.04558700
C	1.18002000	3.34182500	0.04555000
C	-1.21153600	4.74167300	0.08475700
H	-2.09263000	2.74699000	0.03781300
C	1.21324600	4.74122800	0.08471800
H	2.09361300	2.74622600	0.03776700
C	0.00098600	5.45535200	0.10359200
H	-2.17441500	5.25652100	0.10351600
H	2.17631300	5.25572400	0.10344900
H	0.00118700	6.54800600	0.13587100
F	-0.00037600	0.64790100	-4.52185200
F	0.00012600	2.28379100	-2.85338100
C	-3.69082300	-0.50443900	-1.59393900
C	-4.91936000	0.18038700	-1.53137800
C	-3.59308000	-1.56677400	-2.51599600
C	-6.00655000	-0.16055200	-2.34402500
C	-4.66246900	-1.92443300	-3.34644600
C	-5.87319200	-1.21848500	-3.25740800
C	-3.69639700	-0.50172000	1.53985700
C	-4.24819800	0.39261100	2.47966000
C	-4.26076600	-1.78965200	1.47225100
C	-5.30780600	0.02742400	3.31741400
C	-5.32518400	-2.18032600	2.29427200
C	-5.84791500	-1.26570600	3.22179200
C	3.69024700	-0.50585900	-1.59467300
C	4.91895000	0.17872300	-1.53258900
C	3.59205100	-1.56839600	-2.51645500
C	6.00585200	-0.16262100	-2.34545000
C	4.66115100	-1.92646500	-3.34710200
C	5.87203800	-1.22073700	-3.25855300
C	3.69642600	-0.50315600	1.53911800
C	4.26031800	-1.79128600	1.47131400
C	4.24871500	0.39090500	2.47888900
C	5.32473800	-2.18240700	2.29312100
C	5.30833500	0.02527200	3.31643300
C	5.84795900	-1.26804600	3.22062000
F	-6.89647000	-1.63521600	4.03650700
F	-5.84815900	-3.45556600	2.20890000
F	-3.72152300	-2.72619000	0.59247900
F	-5.83712600	0.92973800	4.21744600
F	-3.75554400	1.68858300	2.55297300
F	-6.93482100	-1.56725000	-4.06439900
F	-4.54431000	-2.97652200	-4.23088900
F	-7.19309900	0.54243400	-2.26474100
F	-5.05131700	1.26461100	-0.66143600
F	-2.42584900	-2.31050800	-2.57586700
F	2.42470100	-2.31198600	-2.57577400
F	4.54255700	-2.97875800	-4.23124300
F	6.93338400	-1.56990700	-4.06574000
F	7.19255900	0.54015200	-2.26665400

F	5.05135000	1.26316200	-0.66298300
F	3.72059700	-2.72755000	0.59154300
F	5.84724400	-3.45782700	2.20755400
F	6.89652300	-1.63799500	4.03512500
F	5.83814000	0.92732700	4.21643900

3. $[\mathrm{Fe^{II}(gly)^{\bullet}py_2}]^-$, Complex **A**
E = -5792.77748072 hartrees

Fe	-0.00002700	0.04103200	-0.00799400
N	-1.39868900	-0.07254400	-1.25139600
O	-1.26931100	-0.12411500	-2.61222200
B	-0.00024400	0.48880600	-3.18628000
O	1.26870600	-0.12458000	-2.61246600
N	1.39835600	-0.07303400	-1.25166800
C	2.62587500	-0.27220400	-0.73137600
C	2.63024100	-0.22779400	0.71800600
N	1.40831200	0.00935000	1.23596100
O	1.26626700	-0.11175200	2.59327600
B	0.00036100	0.51378900	3.17032500
O	-1.26586900	-0.11131000	2.59351600
N	-1.40813400	0.00986000	1.23623100
C	-2.63025700	-0.22679500	0.71851500
C	-2.62618900	-0.27125900	-0.73086800
F	0.00058900	1.89590000	2.97372700
F	0.00042400	0.13585700	4.51222400
N	0.00031800	2.03253200	-0.05096800
C	-1.17368800	2.73556500	-0.05796900
C	1.17457200	2.73515000	-0.05815800
C	-1.20579300	4.13562800	-0.07121300
H	-2.09373300	2.15443100	-0.04660500
C	1.20716800	4.13520100	-0.07140800
H	2.09441200	2.15368800	-0.04694900
C	0.00081400	4.85647000	-0.07790100
H	-2.17341600	4.64347800	-0.07194900
H	2.17496900	4.64271000	-0.07230500
H	0.00100700	5.95026600	-0.08538000
N	-0.00037900	-1.98667500	0.04943500
C	-0.00071700	-2.71051200	-1.11403200
C	-0.00031100	-2.66317500	1.24185000
C	-0.00097900	-4.11282200	-1.11540800
H	-0.00078300	-2.14195400	-2.04373600
C	-0.00056900	-4.06428400	1.30001900
H	-0.00004500	-2.05294700	2.14542700
C	-0.00090300	-4.80742100	0.10627300
H	-0.00123900	-4.64064100	-2.07188900
H	-0.00050100	-4.55489800	2.27669200
H	-0.00110200	-5.90117100	0.12793900
F	-0.00044300	0.12017300	-4.52952600
F	0.00003200	1.87837400	-3.00027100
C	-3.82757300	-0.43007300	-1.56729500
C	-4.93558600	0.43778800	-1.45621100
C	-3.93080800	-1.44496800	-2.54498400
C	-6.07756200	0.31488200	-2.25564800

C	-5.05295500	-1.57953600	-3.37046600
C	-6.13578100	-0.69927400	-3.22240800
C	-3.81362900	-0.45133400	1.56440800
C	-4.20156300	0.47706500	2.55829600
C	-4.60772200	-1.61375800	1.45756900
C	-5.29817000	0.25951100	3.39948500
C	-5.71942200	-1.84786000	2.27566000
C	-6.06535100	-0.90729500	3.25624600
C	3.82703800	-0.43142100	-1.56803800
C	4.93566100	0.43561300	-1.45666600
C	3.92941600	-1.44587700	-2.54626500
C	6.07745800	0.31229400	-2.25629800
C	5.05135900	-1.58082300	-3.37196100
C	6.13483600	-0.70141700	-3.22357800
C	3.81370900	-0.45278100	1.56364900
C	4.60724100	-1.61558600	1.45674800
C	4.20231100	0.47554100	2.55735000
C	5.71902200	-1.85012000	2.27460100
C	5.29901800	0.25756600	3.39829900
C	6.06562400	-0.90961200	3.25500300
F	-7.16409300	-1.12433400	4.07380800
F	-6.45956800	-3.01561800	2.14646800
F	-4.25324300	-2.61365400	0.54684900
F	-5.66159500	1.20454800	4.34678700
F	-3.51915000	1.67988700	2.67660500
F	-7.25997500	-0.83598800	-4.02206300
F	-5.12613000	-2.60339800	-4.30293200
F	-7.13426100	1.20529300	-2.12385100
F	-4.88588800	1.50981500	-0.55877600
F	-2.92368300	-2.39389200	-2.66325100
F	2.92149800	-2.39389900	-2.66500900
F	5.12366100	-2.60422700	-4.30499900
F	7.25882700	-0.83851600	-4.02345100
F	7.13481400	1.20187400	-2.12416900
F	4.88685900	1.50715400	-0.55860100
F	4.25206400	-2.61544000	0.54625500
F	6.45858400	-3.01824400	2.14536600
F	7.16445900	-1.12707600	4.07232700
F	5.66311000	1.20253500	4.34541300
F	3.52050000	1.67870200	2.67567900

4. $[Fe^{I}py]^{-}$, Complex **A**

E = -5544.53597378 hartrees

Fe	0.00007900	0.59630400	-0.04133300
N	-1.33489200	0.14562500	-1.26715900
O	-1.24418000	0.11710700	-2.62974500
B	-0.00021600	0.76398500	-3.18736400
O	1.24364000	0.11667700	-2.62999900
N	1.33463200	0.14513300	-1.26743200
C	2.54546200	-0.18417000	-0.75431400
C	2.55330900	-0.15658900	0.66860600
N	1.33935100	0.16835700	1.18270300
O	1.24369600	0.05861200	2.54012800

B	0.00042100	0.66122600	3.15306600
O	-1.24325400	0.05916900	2.54038600
N	-1.33912100	0.16889700	1.18297600
C	-2.55330900	-0.15557000	0.66912500
C	-2.54575000	-0.18319700	-0.75379500
F	0.00072000	2.05732500	2.99779100
F	0.00046800	0.26147200	4.48545900
N	0.00045800	2.58719700	0.09123200
C	-1.17815100	3.27716000	0.11284700
C	1.17931600	3.27672800	0.11308200
C	-1.21083900	4.67733000	0.14908400
H	-2.09005100	2.67752900	0.11051900
C	1.21250600	4.67688700	0.14931800
H	2.09099700	2.67676400	0.11096100
C	0.00096300	5.39205300	0.16587300
H	-2.17460900	5.19162700	0.16838300
H	2.17646000	5.19083100	0.16881000
H	0.00116000	6.48550300	0.19595600
F	-0.00040100	0.50338000	-4.55152600
F	0.00005600	2.14335000	-2.89015100
C	-3.69871200	-0.51879500	-1.60932700
C	-4.89781800	0.21894500	-1.56391200
C	-3.64888200	-1.58425500	-2.53408500
C	-5.99248400	-0.06994200	-2.38786700
C	-4.72349700	-1.88510600	-3.38035700
C	-5.90138900	-1.12685600	-3.30444800
C	-3.70349000	-0.48615300	1.53016700
C	-4.19559600	0.43566700	2.47918700
C	-4.35240600	-1.73571400	1.47627300
C	-5.25911300	0.13199400	3.33604900
C	-5.42879800	-2.06119100	2.31210100
C	-5.88091300	-1.12316800	3.25027800
C	3.69813800	-0.52014400	-1.61008500
C	4.89753400	0.21713700	-1.56481600
C	3.64773100	-1.58548600	-2.53494600
C	5.99193700	-0.07207800	-2.38900400
C	4.72207500	-1.88665200	-3.38145100
C	5.90026900	-1.12885800	-3.30568200
C	3.70352200	-0.48767500	1.52941200
C	4.35189200	-1.73751400	1.47537200
C	4.19622300	0.43392400	2.47834000
C	5.42831600	-2.06346300	2.31097300
C	5.25978800	0.12978400	3.33497800
C	5.88102800	-1.12564500	3.24906700
F	-6.94394600	-1.43053800	4.08426700
F	-6.03305100	-3.30737900	2.23467300
F	-3.89497900	-2.71493700	0.59423700
F	-5.72680500	1.06832700	4.24482600
F	-3.64708000	1.71011400	2.54333400
F	-6.97516700	-1.42592700	-4.12746000
F	-4.64978900	-2.94659700	-4.26746500
F	-7.15080500	0.69117000	-2.32106500
F	-5.00301000	1.31323400	-0.70027100
F	-2.53069900	-2.40026100	-2.58253100

F	2.52923300	-2.40106600	-2.58327500
F	4.64779800	-2.94802000	-4.26866000
F	6.97377900	-1.42824600	-4.12892900
F	7.15056000	0.68858600	-2.32233400
F	5.00330500	1.31129200	-0.70107700
F	3.89385200	-2.71654300	0.59343900
F	6.03201300	-3.30991300	2.23341100
F	6.94409900	-1.43348200	4.08283500
F	5.72807700	1.06590800	4.24366300
F	3.64829600	1.70861900	2.54259500

5. $[\mathrm{Fe}^0\mathrm{py}]^{2-}$, Complex A
E = -5544.55116669 hartrees

Fe	0.00003600	0.38533300	-0.00466100
N	-1.33790300	-0.00962800	-1.22503100
O	-1.25025500	-0.05725000	-2.59794400
B	-0.00025200	0.53004600	-3.18519300
O	1.24966700	-0.05767600	-2.59818800
N	1.33759200	-0.01011200	-1.22529200
C	2.58240000	-0.23112000	-0.71883300
C	2.59131600	-0.17751200	0.71598100
N	1.35281700	0.07065700	1.22144300
O	1.24896200	-0.07276600	2.58801100
B	0.00037300	0.50731200	3.19358100
O	-1.24856900	-0.07226400	2.58825700
N	-1.35262300	0.07116000	1.22170300
C	-2.59131500	-0.17654400	0.71648400
C	-2.58269300	-0.23018400	-0.71833000
F	0.00064900	1.91397800	3.09378600
F	0.00041800	0.08026200	4.53419200
N	0.00038400	2.28941100	-0.04311500
C	-1.18021900	2.99562000	-0.05235900
C	1.18123500	2.99520400	-0.05246000
C	-1.20739400	4.39355600	-0.07505600
H	-2.09512300	2.40082000	-0.03373100
C	1.20889800	4.39313000	-0.07515900
H	2.09593200	2.40008100	-0.03390400
C	0.00087900	5.11846400	-0.08823600
H	-2.17547600	4.90308000	-0.07898800
H	2.17715800	4.90231500	-0.07917300
H	0.00107200	6.21279900	-0.10474400
F	-0.00045000	0.15348100	-4.53923500
F	0.00000500	1.94039300	-3.05130900
C	-3.75374500	-0.45530000	-1.56906100
C	-4.92696000	0.32822700	-1.46600000
C	-3.78054600	-1.46923000	-2.56017600
C	-6.04514400	0.13792800	-2.28521800
C	-4.87761800	-1.66270000	-3.40666100
C	-6.02118700	-0.86130100	-3.26819800
C	-3.74823900	-0.45693200	1.57333200
C	-4.14447800	0.43237700	2.60447200
C	-4.53431600	-1.62615100	1.44388000
C	-5.22501500	0.17032700	3.45224000

C	-5.63422600	-1.89951800	2.26589900
C	-5.98109200	-1.00022400	3.28287800
C	3.75321400	-0.45662000	-1.56979100
C	4.92672100	0.32649600	-1.46692900
C	3.77947400	-1.47052700	-2.56094500
C	6.04467900	0.13584300	-2.28637300
C	4.87631400	-1.66434400	-3.40765000
C	6.02018400	-0.86334200	-3.26938600
C	3.74828800	-0.45843800	1.57258900
C	4.53379300	-1.62802000	1.44293400
C	4.14516200	0.43065700	2.60366800
C	5.63375900	-1.90191900	2.26469900
C	5.22576800	0.16808300	3.45118700
C	5.98126800	-1.00281300	3.28162400
F	-7.07120500	-1.25985300	4.11084200
F	-6.36058200	-3.07946600	2.11324300
F	-4.18311000	-2.60354200	0.50678400
F	-5.60091300	1.08678900	4.43079800
F	-3.50043100	1.65465000	2.74517100
F	-7.12566600	-1.06147000	-4.09385700
F	-4.87872700	-2.69004800	-4.34611400
F	-7.16493400	0.96024500	-2.16564800
F	-4.97195600	1.39921400	-0.56306700
F	-2.73245400	-2.37361900	-2.65355400
F	2.73105800	-2.37455900	-2.65414600
F	4.87688700	-2.69166200	-4.34713700
F	7.12443100	-1.06385800	-4.09527200
F	7.16477700	0.95776800	-2.16699100
F	4.97226700	1.39742800	-0.56395700
F	4.18191600	-2.60523100	0.50590300
F	6.35953300	-3.08220100	2.11185100
F	7.07144600	-1.26296800	4.10933600
F	5.60231000	1.08434300	4.42968700
F	3.50172600	1.65323200	2.74453300

6. [Fe^{III}Hpy]^{0} , Complex **A**

E = -5544.98440599 hartrees

Fe	0.00003100	0.35305700	-0.01780800
N	-1.38624300	0.10550800	-1.26312500
O	-1.26329100	0.06677200	-2.59798400
B	-0.00022600	0.71407600	-3.18062000
O	1.26272400	0.06631400	-2.59824600
N	1.38595900	0.10498400	-1.26341200
C	2.59170600	-0.17100800	-0.74532500
C	2.59658200	-0.16465100	0.69754900
N	1.39312100	0.10664600	1.22278700
O	1.26411800	-0.00240000	2.55364300
B	0.00041500	0.62749600	3.16224200
O	-1.26368500	-0.00186200	2.55390600
N	-1.39290400	0.10720000	1.22307400
C	-2.59657800	-0.16363300	0.69808200
C	-2.59199000	-0.17002300	-0.74479400
F	0.00068200	1.99564500	2.92449100

F	0.00047100	0.24946100	4.48113100
N	0.00041600	2.39192400	0.01236300
C	-1.17641900	3.08461100	0.02701100
C	1.17751100	3.08417000	0.02702500
C	-1.21058000	4.48427700	0.05361700
H	-2.09326400	2.49377800	0.02423000
C	1.21219400	4.48382200	0.05362600
H	2.09413400	2.49299200	0.02427500
C	0.00094100	5.19923800	0.06633500
H	-2.17416600	4.99796700	0.06763800
H	2.17597200	4.99715200	0.06765900
H	0.00114600	6.29214500	0.08905700
F	-0.00042400	0.39762000	-4.51476100
F	0.00005500	2.07628600	-2.88987900
C	-3.76674900	-0.45733200	-1.59166500
C	-4.92335700	0.34300400	-1.53743500
C	-3.76796100	-1.52949800	-2.50720400
C	-6.03594100	0.10297300	-2.35182800
C	-4.86439500	-1.78807700	-3.33935300
C	-6.00201700	-0.96890700	-3.25823400
C	-3.76735900	-0.47312500	1.54450600
C	-4.24866900	0.45822500	2.48632600
C	-4.42603200	-1.71537000	1.47650100
C	-5.33052800	0.17176900	3.32659800
C	-5.51452700	-2.02699200	2.30085700
C	-5.96562100	-1.07735300	3.23082300
C	3.76619900	-0.45871300	-1.59243100
C	4.92308500	0.34123800	-1.53841400
C	3.76687600	-1.53086100	-2.50799200
C	6.03542500	0.10086300	-2.35303800
C	4.86305800	-1.78978000	-3.34036700
C	6.00096400	-0.97098400	-3.25946300
C	3.76740200	-0.47465200	1.54373400
C	4.42556000	-1.71716000	1.47554000
C	4.24926300	0.45645200	2.48551500
C	5.51408100	-2.02926700	2.29967800
C	5.33116000	0.16951200	3.32557300
C	5.96572700	-1.07986300	3.22961500
F	-7.03673200	-1.36901000	4.04767500
F	-6.13164200	-3.25923200	2.21452700
F	-3.96155900	-2.68681700	0.59248400
F	-5.78704900	1.10924600	4.23045200
F	-3.65731000	1.71203400	2.56314400
F	-7.08996800	-1.21924500	-4.06655300
F	-4.84434900	-2.85077100	-4.21858100
F	-7.14989300	0.91669500	-2.28070000
F	-4.95263900	1.43906900	-0.67254100
F	-2.67501400	-2.37855100	-2.56166400
F	2.67365100	-2.37957000	-2.56223900
F	4.84249000	-2.85245300	-4.21960800
F	7.08866900	-1.22166100	-4.06800900
F	7.14966000	0.91421500	-2.28211300
F	4.95290300	1.43727200	-0.67349900
F	3.96053100	-2.68837000	0.59155500

F	6.13068100	-3.26175200	2.21316700
F	7.03686800	-1.37200000	4.04625700
F	5.78822900	1.10675500	4.22939300
F	3.65843500	1.71050100	2.56250400
H	-0.00025700	-1.16269100	-0.01169400

7. [Fe^{II}Hpy]$^{-}$, Complex **A**

E= -5545.12033375 hartrees

Fe	0.00000300	0.25088900	-0.01457300
N	-1.38154400	0.02528300	-1.25159100
O	-1.26751900	-0.01978400	-2.60030900
B	-0.00026300	0.58390300	-3.18549300
O	1.26690200	-0.02023200	-2.60057200
N	1.38121900	0.02477300	-1.25187700
C	2.60064100	-0.18605700	-0.74100600
C	2.60448000	-0.16269500	0.71344800
N	1.39101800	0.06601300	1.22644900
O	1.26763600	-0.04185700	2.57182900
B	0.00039100	0.56027100	3.16773800
O	-1.26722100	-0.04134500	2.57209100
N	-1.39082700	0.06654200	1.22673400
C	-2.60447800	-0.16171600	0.71398000
C	-2.60094000	-0.18508700	-0.74047400
F	0.00065600	1.94696400	2.99621900
F	0.00044700	0.15949700	4.49805800
N	0.00037800	2.25533900	-0.02388300
C	-1.17431100	2.95789600	-0.02240500
C	1.17533400	2.95745200	-0.02254300
C	-1.20742100	4.35778900	-0.02068500
H	-2.09234000	2.36895100	-0.01670500
C	1.20897300	4.35733100	-0.02082800
H	2.09313800	2.36815400	-0.01694600
C	0.00091200	5.07832200	-0.02033600
H	-2.17394600	4.86812600	-0.01626300
H	2.17569100	4.86730300	-0.01651900
H	0.00112000	6.17206000	-0.01701000
F	-0.00046900	0.21360300	-4.52357900
F	0.00000500	1.97320400	-2.99702400
C	-3.78655500	-0.42548800	-1.58235800
C	-4.93279400	0.39036700	-1.50070400
C	-3.82758600	-1.47543100	-2.52614600
C	-6.05884800	0.19271100	-2.30834300
C	-4.93434500	-1.68433600	-3.35870800
C	-6.05647300	-0.84990900	-3.24631300
C	-3.77793700	-0.45019300	1.56200300
C	-4.22503500	0.46893800	2.53522200
C	-4.49311800	-1.66051600	1.46620400
C	-5.31237700	0.19795400	3.37420600
C	-5.59312700	-1.95144600	2.28317600
C	-6.00181000	-1.01727900	3.24523900
C	3.78601000	-0.42687600	-1.58311800
C	4.93247400	0.38869900	-1.50181600
C	3.82659200	-1.47698300	-2.52674700

C	6.05830400	0.19065500	-2.30967200
C	4.93312400	-1.68627900	-3.35951200
C	6.05547200	-0.85210000	-3.24749200
C	3.77798900	-0.45168300	1.56122900
C	4.49263200	-1.66230900	1.46525300
C	4.22568000	0.46723200	2.53438100
C	5.59267800	-1.95373700	2.28199700
C	5.31307200	0.19575500	3.37314100
C	6.00195300	-1.01977300	3.24400600
F	-7.08726100	-1.29021600	4.06130500
F	-6.26303300	-3.15985000	2.16442900
F	-4.07803700	-2.63680400	0.56038200
F	-5.73398700	1.12934900	4.30925000
F	-3.60554200	1.70530100	2.64623600
F	-7.16190000	-1.05768400	-4.05507100
F	-4.94966100	-2.73216700	-4.26463400
F	-7.16019100	1.03000700	-2.20622200
F	-4.94442000	1.47325200	-0.61609200
F	-2.77225600	-2.36886700	-2.60681700
F	2.77108200	-2.37024300	-2.60698900
F	4.94801100	-2.73427500	-4.26525500
F	7.16067900	-1.06026900	-4.05644900
F	7.15987500	1.02769200	-2.20790400
F	4.94455400	1.47170700	-0.61736100
F	4.07694700	-2.63839600	0.55949000
F	6.26204100	-3.16242500	2.16308300
F	7.08744800	-1.29320000	4.05984800
F	5.73527500	1.12694600	4.30812100
F	3.60676600	1.70387300	2.64553200
H	-0.00027100	-1.27326600	0.01964600

8. $[Fe^{II}py_2]^0$, Complex **B**

E = -5568.56189964 hartrees

Fe	0.00534000	-0.03525400	0.00374000
N	-1.40388300	-0.12037900	-1.24793800
O	-1.26470500	-0.15164200	-2.59836000
B	0.00017000	0.49439600	-3.16005000
O	1.28668100	-0.13517300	-2.59047100
N	1.41968900	-0.11698300	-1.24596800
C	2.63732900	-0.29943800	-0.73743100
C	2.64768700	-0.26990500	0.72841300
N	1.43636900	-0.07928900	1.24022500
O	1.28168500	-0.01886900	2.58320300
O	-1.22982900	-0.04700300	2.56408400
N	-1.41746600	-0.09084400	1.26525600
C	-2.63189600	-0.27681400	0.73099400
C	-2.61509600	-0.29809800	-0.73351700
N	-0.01584900	1.96160700	0.03795200
C	-1.19401400	2.66346400	0.05061100
C	1.15401800	2.67783700	0.03059800
C	-1.23353000	4.06333300	0.06246900
H	-2.11514300	2.08519100	0.05363500
C	1.17813500	4.07767000	0.04225500

H	2.08171000	2.11017000	0.01233300
C	-0.03212100	4.79250500	0.05760200
H	-2.20421700	4.56418200	0.07353100
H	2.14283900	4.59010800	0.03569700
H	-0.03855500	5.88548400	0.06360600
N	-0.00714700	-2.05759000	0.02292500
C	0.00686500	-2.77078100	-1.14777800
C	-0.02879900	-2.74883000	1.20765100
C	0.00418900	-4.17289700	-1.16309900
H	0.01811800	-2.19654100	-2.07369300
C	-0.03172300	-4.14896600	1.25300000
H	-0.05350200	-2.15263500	2.12025800
C	-0.01379200	-4.87985800	0.05104000
H	0.01555700	-4.69102800	-2.12437000
H	-0.05059600	-4.65078600	2.22336300
H	-0.01591400	-5.97299900	0.06173800
F	0.01215600	0.15968200	-4.49829600
F	0.00051300	1.86304700	-2.90048300
C	-3.82195400	-0.43696900	-1.57702300
C	-4.87348900	0.49665700	-1.50727200
C	-3.96001800	-1.47871800	-2.51491800
C	-6.01024900	0.41029800	-2.31921100
C	-5.08095800	-1.58645700	-3.34755500
C	-6.11150700	-0.63882600	-3.24587100
C	-3.83751300	-0.45368800	1.56342600
C	-4.22894000	0.51401200	2.51121100
C	-4.62614800	-1.61871200	1.48875300
C	-5.33958800	0.33461000	3.34534500
C	-5.74849300	-1.82083800	2.30100200
C	-6.10340200	-0.83805600	3.23788300
C	3.84227800	-0.44426200	-1.57962900
C	4.90485000	0.47713000	-1.50518800
C	3.96867900	-1.48072000	-2.52601300
C	6.03961400	0.38433600	-2.31899000
C	5.08661600	-1.59360600	-3.36186500
C	6.12786700	-0.65827300	-3.25441600
C	3.85544500	-0.44143600	1.56206700
C	4.63356800	-1.61387900	1.49609800
C	4.26670700	0.54278300	2.48330200
C	5.76583000	-1.80825400	2.29648500
C	5.39008900	0.37257200	3.30216900
C	6.14271400	-0.80853500	3.20672900
F	-7.20538700	-1.02245400	4.04899000
F	-6.48963500	-2.98490600	2.20370100
F	-4.25937100	-2.63560100	0.60467800
F	-5.70197000	1.31017400	4.25515200
F	-3.52743800	1.70943300	2.59629800
F	-7.22505100	-0.73966200	-4.05445000
F	-5.19041400	-2.62761600	-4.24894300
F	-7.01566500	1.35469900	-2.22808200
F	-4.76713000	1.57942300	-0.63073500
F	-2.97941200	-2.45770300	-2.60010300
F	2.97849600	-2.44951200	-2.61565600
F	5.18356800	-2.62918400	-4.27079200

F	7.23905200	-0.76518700	-4.06512900
F	7.05553700	1.31673500	-2.22166200
F	4.81131000	1.55497000	-0.62074700
F	4.24788900	-2.64092300	0.63400700
F	6.49628300	-2.97894600	2.21174600
F	7.25459100	-0.98520600	4.00436800
F	5.77319300	1.36299200	4.18575900
F	3.56992200	1.74103800	2.55800700
H	0.19842000	0.03616600	2.68565000

9. $[\mathrm{Fe^{II}py}]^0$, Complex **B**
E = -5320.28201423 hartrees

Fe	-0.00305000	0.53094800	-0.02510900
N	-1.37233700	0.19319400	-1.28212300
O	-1.24028800	0.16062000	-2.62843400
B	0.00207800	0.86075500	-3.16413200
O	1.27504300	0.20343600	-2.61588300
N	1.39181100	0.21789000	-1.27365100
C	2.57737200	-0.13694400	-0.75676700
C	2.58500600	-0.12478200	0.69088600
N	1.39494000	0.19444000	1.21125600
O	1.25970500	0.21055200	2.55825400
O	-1.24564100	0.27039200	2.52500400
N	-1.40519000	0.22040300	1.22790000
C	-2.58992600	-0.12110800	0.67910600
C	-2.55736200	-0.15623000	-0.76647800
N	-0.00256900	2.55584800	0.14729500
C	-1.18259800	3.24449400	0.20788200
C	1.17528000	3.25050600	0.14003400
C	-1.21724200	4.64411500	0.26242000
H	-2.09498300	2.64684700	0.21562700
C	1.20664800	4.65010600	0.19397800
H	2.08923000	2.65730500	0.09011400
C	-0.00639100	5.36120100	0.25342400
H	-2.18067200	5.15630600	0.30937400
H	2.16857600	5.16721800	0.18550500
H	-0.00797400	6.45372500	0.29202500
F	0.01738300	0.63592600	-4.51894900
F	-0.01542200	2.20778500	-2.78495800
C	-3.70345700	-0.52882100	-1.62081200
C	-4.90927900	0.19671000	-1.59007900
C	-3.62653900	-1.60856400	-2.52381300
C	-5.99376100	-0.12134500	-2.41575800
C	-4.69368200	-1.94477500	-3.36609300
C	-5.88146200	-1.19819000	-3.30916800
C	-3.75902800	-0.45407400	1.51513600
C	-4.28084200	0.47486200	2.43727500
C	-4.37352800	-1.72051300	1.47120700
C	-5.35620500	0.16631300	3.27846800
C	-5.45659700	-2.05468200	2.29382800
C	-5.94649200	-1.10540900	3.20413900
C	3.73089900	-0.50084300	-1.60295300
C	4.93763400	0.22240200	-1.55509200

C	3.66063400	-1.57050600	-2.51907600
C	6.02885700	-0.08793500	-2.37471300
C	4.73377900	-1.89788100	-3.35723000
C	5.92224500	-1.15391300	-3.28184400
C	3.75231700	-0.45802200	1.53311500
C	4.36687100	-1.72392800	1.48351100
C	4.28021400	0.47405400	2.44803500
C	5.45693200	-2.05556700	2.29811000
C	5.36499300	0.16860700	3.27821800
C	5.95508800	-1.10318900	3.20080900
F	-7.01172100	-1.42007200	4.02243700
F	-6.02825500	-3.31114600	2.22985700
F	-3.86975900	-2.69484300	0.61112100
F	-5.85267400	1.10593300	4.16149500
F	-3.74702800	1.75715800	2.48534300
F	-6.94145400	-1.52530600	-4.12856300
F	-4.59631300	-3.01513700	-4.23189300
F	-7.15799000	0.62198800	-2.36750400
F	-5.02111300	1.29948700	-0.74048800
F	-2.48361100	-2.39096300	-2.55380800
F	2.51702000	-2.35109700	-2.56686300
F	4.64205900	-2.95793900	-4.23612000
F	6.98857600	-1.47327400	-4.09601500
F	7.19389200	0.65279500	-2.30782200
F	5.04324400	1.31608500	-0.69216800
F	3.85780700	-2.69723500	0.62699600
F	6.02867900	-3.31110400	2.23161400
F	7.02741100	-1.41524500	4.00966700
F	5.86841000	1.11003100	4.15437100
F	3.73882500	1.75233800	2.50305600
H	0.18978400	0.28669200	2.67873600

10. $[Fe^{II}(gly)^{\bullet}py_2]^-$, Complex **B**

E = -5568.65181896 hartrees

Fe	-0.00841800	-0.04707500	0.00961000
N	-1.40108100	-0.14022600	-1.24002900
O	-1.26264200	-0.18207400	-2.60341200
B	0.00538600	0.44134200	-3.16390800
O	1.27332700	-0.17937600	-2.60755700
N	1.40362900	-0.14137400	-1.24167400
C	2.63897600	-0.31570600	-0.72908100
C	2.65542700	-0.26543100	0.72091400
N	1.42681500	-0.06831500	1.24172000
O	1.28011100	-0.08979100	2.60825000
O	-1.24677900	-0.08744200	2.57742600
N	-1.42221700	-0.07856400	1.26510600
C	-2.65188500	-0.26206800	0.72273700
C	-2.63255700	-0.30417400	-0.72916500
N	-0.01094500	1.94261700	0.00392500
C	-1.18535800	2.65069200	0.00218800
C	1.16438800	2.64944800	-0.00697300
C	-1.21608500	4.05120400	-0.00146400
H	-2.10617400	2.07071400	0.00765800

C	1.19641800	4.04978000	-0.01112600
H	2.08438700	2.06852000	-0.01255300
C	-0.00951100	4.77295000	-0.00847500
H	-2.18400800	4.55875800	-0.00090800
H	2.16480600	4.55635800	-0.01960600
H	-0.00887800	5.86681100	-0.01421200
N	-0.01190900	-2.06341600	0.04927300
C	0.02075600	-2.78105400	-1.11767500
C	-0.04720100	-2.74631900	1.23700000
C	0.02317400	-4.18362900	-1.12539700
H	0.04514500	-2.20546900	-2.04297400
C	-0.04519300	-4.14709900	1.28971200
H	-0.08607300	-2.13812100	2.14147500
C	-0.00807300	-4.88448200	0.09233300
H	0.05058100	-4.70699700	-2.08396400
H	-0.07443500	-4.64401600	2.26291900
H	-0.00512900	-5.97835700	0.10877500
F	0.00150300	0.10342900	-4.51721300
F	0.00272200	1.83031800	-2.95119800
C	-3.82993400	-0.42412200	-1.57771400
C	-4.91215600	0.47680100	-1.47291300
C	-3.95390100	-1.42883900	-2.56384900
C	-6.04818200	0.39512900	-2.28541700
C	-5.07116200	-1.52338800	-3.40128200
C	-6.12802900	-0.61088800	-3.25922800
C	-3.84477400	-0.44278100	1.56106300
C	-4.18827100	0.48564800	2.57151300
C	-4.68774100	-1.57082000	1.44935000
C	-5.28528500	0.30095700	3.42064600
C	-5.80241100	-1.76984600	2.27247900
C	-6.10083500	-0.83100000	3.27034900
C	3.83699500	-0.44135900	-1.57410700
C	4.92372400	0.45535400	-1.47229000
C	3.95708300	-1.44753800	-2.55976100
C	6.06057700	0.36514800	-2.28276000
C	5.07441900	-1.54990300	-3.39581200
C	6.13676700	-0.64351100	-3.25390800
C	3.85388700	-0.43051700	1.55449800
C	4.70410100	-1.55529500	1.44340800
C	4.21094800	0.51588800	2.54480000
C	5.83585900	-1.73185200	2.24730500
C	5.32714100	0.35447200	3.37201500
C	6.14908400	-0.77403000	3.22303900
F	-7.20043500	-1.01497400	4.09697500
F	-6.59052400	-2.90615300	2.13642800
F	-4.38091800	-2.57516700	0.52541300
F	-5.60185000	1.24840800	4.38496800
F	-3.46928700	1.66860700	2.69290200
F	-7.24809900	-0.70778000	-4.07169500
F	-5.16701400	-2.53930300	-4.34122300
F	-7.07724300	1.31947400	-2.16078500
F	-4.83717600	1.54489800	-0.57140400
F	-2.97571900	-2.40840800	-2.67806700
F	2.97336500	-2.42201500	-2.67405000

F	5.16577200	-2.56869700	-4.33336700
F	7.25885500	-0.75068300	-4.06265700
F	7.09411900	1.28524300	-2.16005900
F	4.85190200	1.53126700	-0.57905200
F	4.38436000	-2.57908200	0.54599500
F	6.62623400	-2.86725400	2.11776800
F	7.26797900	-0.93515900	4.02825900
F	5.65837100	1.32242200	4.31068100
F	3.48091500	1.69296200	2.66434900
H	0.21554900	-0.01870600	2.70804400

11. [Fe^{I}py]$^{-}$, Complex **B**

E = -5320.40924106 hartrees

Fe	0.00528800	0.56107900	-0.06958700
N	-1.33798500	0.10066600	-1.29018100
O	-1.23446800	0.06363400	-2.65596200
B	0.00100600	0.74559300	-3.18789600
O	1.26328400	0.10784600	-2.65942100
N	1.36054300	0.12774500	-1.29418900
C	2.57090000	-0.18696600	-0.77924700
C	2.58223600	-0.13589500	0.64983700
N	1.36240800	0.17235800	1.15610100
O	1.24102600	0.18039200	2.51276500
O	-1.21518200	0.23479500	2.49801400
N	-1.35248900	0.20369100	1.17795100
C	-2.56929100	-0.12322700	0.65483600
C	-2.54914000	-0.19750500	-0.77240700
N	-0.00926500	2.52342200	0.23385300
C	-1.19136800	3.21564600	0.24571700
C	1.16720100	3.22518900	0.25909000
C	-1.22867900	4.61587300	0.27108800
H	-2.10090000	2.61256000	0.23982600
C	1.19319600	4.62555700	0.28676600
H	2.08160400	2.62936600	0.26077500
C	-0.02075200	5.33830900	0.28865800
H	-2.19546800	5.12537200	0.27672400
H	2.15574000	5.14280300	0.30458300
H	-0.02522200	6.43201600	0.30475400
F	0.00382300	0.53766200	-4.56237800
F	-0.02179200	2.11553100	-2.83553200
C	-3.70377600	-0.53451300	-1.62424800
C	-4.89972800	0.20988200	-1.58590000
C	-3.65938700	-1.60528500	-2.54374100
C	-5.99369800	-0.07681800	-2.41126800
C	-4.73382600	-1.90414100	-3.39072600
C	-5.90764700	-1.13912700	-3.32198900
C	-3.71978200	-0.43514100	1.51743400
C	-4.19549800	0.48829400	2.47396000
C	-4.38407600	-1.67878700	1.47318900
C	-5.25376500	0.19454200	3.34129500
C	-5.45742100	-1.99315600	2.31661500
C	-5.89107100	-1.05267900	3.26119100
C	3.72433100	-0.52480900	-1.63125000

C	4.92659600	0.20903100	-1.58499300
C	3.67207700	-1.58578600	-2.56206400
C	6.01900900	-0.07843500	-2.41219300
C	4.74438400	-1.88445100	-3.41175100
C	5.92461700	-1.13005900	-3.33436800
C	3.73675300	-0.44379900	1.51062300
C	4.40674400	-1.68417800	1.45934100
C	4.21873600	0.48406400	2.45938800
C	5.49127800	-1.99112300	2.29121400
C	5.28948800	0.19827700	3.31371100
C	5.93192700	-1.04608700	3.22810900
F	-6.94955600	-1.35017700	4.10673800
F	-6.07320500	-3.23539700	2.24695200
F	-3.94246800	-2.66765100	0.59265500
F	-5.70388500	1.13701500	4.25552800
F	-3.64748300	1.76472600	2.52823800
F	-6.98196000	-1.43624600	-4.14631300
F	-4.66511100	-2.97243500	-4.27109600
F	-7.14776000	0.69269100	-2.35196400
F	-5.00190400	1.31171200	-0.73097900
F	-2.54806400	-2.43142500	-2.58413400
F	2.55458300	-2.40323700	-2.61045300
F	4.66760700	-2.94320200	-4.30291900
F	6.99704300	-1.42765600	-4.16102500
F	7.17958400	0.68056100	-2.34370700
F	5.03719500	1.30188600	-0.71913500
F	3.96120400	-2.67504700	0.58416500
F	6.11181700	-3.23025100	2.21738800
F	7.00092500	-1.33689300	4.06203500
F	5.74579700	1.14499300	4.21991400
F	3.65862200	1.75495200	2.52113100
H	0.14130400	0.24074100	2.63312800

12. $[Fe^0py]^{2-}$, Complex **B**

E = -5320.41480778 hartrees

Fe	0.00705500	0.27296400	-0.00781300
N	-1.33841300	-0.11268000	-1.22304300
O	-1.24427300	-0.16579600	-2.59728500
B	0.00819100	0.41992500	-3.18085200
O	1.26321300	-0.16278700	-2.60054800
N	1.35475900	-0.11232600	-1.22550000
C	2.61063600	-0.28146900	-0.72224800
C	2.62321900	-0.20922100	0.71528900
N	1.37482200	-0.00639000	1.22067600
O	1.23741300	-0.06170200	2.58108700
O	-1.20809200	-0.04147500	2.57271800
N	-1.35799600	0.00670700	1.23957400
C	-2.60491200	-0.19814000	0.72003700
C	-2.59227000	-0.27479700	-0.71852600
N	-0.00965500	2.17700300	-0.02286100
C	-1.19366200	2.88436100	-0.03727800
C	1.16960300	2.89289800	-0.03325900
C	-1.22473000	4.28231600	-0.05384800

H	-2.10747700	2.28752400	-0.03164900
C	1.19114300	4.29079300	-0.04992200
H	2.08761300	2.30236400	-0.02522800
C	-0.01950200	5.01413800	-0.06043700
H	-2.19544300	4.78738800	-0.06438900
H	2.15830600	4.80266600	-0.05768000
H	-0.02331500	6.10852200	-0.07647700
F	0.00668500	0.04628500	-4.53734600
F	0.00669700	1.83233000	-3.04697200
C	-3.77051500	-0.44374200	-1.56786500
C	-4.91684600	0.37966600	-1.44753100
C	-3.84184900	-1.43994100	-2.57697300
C	-6.04334700	0.24553100	-2.26514300
C	-4.94821300	-1.57691600	-3.42167400
C	-6.06193000	-0.73691700	-3.26550800
C	-3.76354500	-0.44318200	1.57976600
C	-4.10436700	0.43854000	2.63841900
C	-4.60048100	-1.57845200	1.44876100
C	-5.17627200	0.20188400	3.50477400
C	-5.69384600	-1.82322700	2.28784100
C	-5.98298100	-0.93335100	3.33129200
C	3.78703400	-0.45557800	-1.57330900
C	4.93343100	0.36854100	-1.46273400
C	3.85249600	-1.45631000	-2.57794800
C	6.05627500	0.22955000	-2.28482700
C	4.95492800	-1.59838000	-3.42698500
C	6.06960100	-0.75806700	-3.28001100
C	3.78706200	-0.43981600	1.57264800
C	4.63144300	-1.57064700	1.44432800
C	4.13346600	0.45604600	2.61778100
C	5.73491500	-1.79785500	2.27479500
C	5.21667200	0.23787900	3.47431600
C	6.02973500	-0.89366500	3.30464200
F	-7.06480100	-1.16707700	4.18016200
F	-6.46821300	-2.97329000	2.13178500
F	-4.30701500	-2.55616300	0.49135800
F	-5.49508100	1.11497800	4.50960300
F	-3.42532100	1.64342700	2.78216200
F	-7.17773500	-0.88244600	-4.08957900
F	-4.99381500	-2.59188800	-4.37509200
F	-7.12983700	1.11111900	-2.12989100
F	-4.91713000	1.44369100	-0.53342700
F	-2.83501400	-2.38993300	-2.68480300
F	2.84303800	-2.40420700	-2.67749700
F	4.99511500	-2.61728600	-4.37621400
F	7.18163500	-0.90881500	-4.10800200
F	7.14437500	1.09432600	-2.15828300
F	4.93857700	1.43689300	-0.55367600
F	4.33571300	-2.55995300	0.50029000
F	6.51411300	-2.94508600	2.12500800
F	7.12047400	-1.11165300	4.14581800
F	5.54079000	1.16584500	4.46336900
F	3.44175400	1.65424500	2.75791800
H	0.11270000	-0.04083700	2.68618300

13. $[Fe^{I}py\ldots H]^{0}$, Complex **B**

E = -5320.87506508 hartrees

Fe	-0.01220200	0.44712700	0.05471000
N	-1.35684400	0.08031500	-1.18884700
O	-1.26858800	0.11671500	-2.53691400
B	0.01581900	0.70377900	-3.09500400
O	1.20456300	-0.04571600	-2.53341300
N	1.32320300	0.01555100	-1.18506600
C	2.56128300	-0.23965200	-0.69870000
C	2.61104500	-0.15729300	0.72370000
N	1.40576000	0.12960000	1.25107500
O	1.37897600	0.21331600	2.63981000
O	-1.29581600	-0.15387400	2.66185200
N	-1.37514800	-0.06476800	1.21836400
C	-2.61570200	-0.28461500	0.70364800
C	-2.59478200	-0.23364000	-0.70993000
N	0.00083900	2.44598500	0.20883000
C	-1.18295600	3.12957700	0.27565500
C	1.17426600	3.14467600	0.13119200
C	-1.22439500	4.52981400	0.26737300
H	-2.09121500	2.52734600	0.33625200
C	1.19606700	4.54538700	0.11756200
H	2.09049000	2.55474200	0.07862200
C	-0.01907900	5.25212900	0.18404900
H	-2.18937200	5.03873300	0.31967300
H	2.15353700	5.06641900	0.05047800
H	-0.02707600	6.34522100	0.16896600
F	-0.00285500	0.46784800	-4.45058700
F	0.10155500	2.06032200	-2.74325600
C	-3.74295200	-0.48196400	-1.60347300
C	-4.88482800	0.33987500	-1.58927200
C	-3.72684900	-1.53729900	-2.53831700
C	-5.96448000	0.13757400	-2.45761000
C	-4.78703000	-1.75690800	-3.42633400
C	-5.91101500	-0.91658100	-3.38236100
C	-3.81347000	-0.53116800	1.53112900
C	-4.27726200	0.43781500	2.44620400
C	-4.56199700	-1.72186300	1.43486000
C	-5.42025900	0.23891000	3.22861800
C	-5.71496400	-1.94414700	2.20002900
C	-6.14326200	-0.95872600	3.10269500
C	3.70531600	-0.54464800	-1.57845100
C	4.84984700	0.27439000	-1.61138400
C	3.68872100	-1.65367600	-2.44910400
C	5.92968100	0.01924000	-2.46475100
C	4.74991200	-1.92710200	-3.32100800
C	5.87570600	-1.08829900	-3.32497500
C	3.81592200	-0.38799700	1.54704000
C	4.49132100	-1.62427300	1.53961500
C	4.33605200	0.61499600	2.38875800
C	5.62678800	-1.86009200	2.32564200
C	5.46420000	0.40567200	3.19050500

C	6.11253800	-0.83914200	3.15682700
F	-7.27255000	-1.16561800	3.86679200
F	-6.41512300	-3.12960600	2.08745700
F	-4.13116900	-2.73407300	0.58096200
F	-5.85274800	1.21541900	4.10500100
F	-3.60947000	1.65299900	2.54583600
F	-6.96759100	-1.13111300	-4.24394600
F	-4.74809500	-2.80458700	-4.32498200
F	-7.06688100	0.97219300	-2.41915900
F	-4.93819500	1.42229600	-0.70596600
F	-2.64825400	-2.40722300	-2.56171600
F	2.61001000	-2.52307500	-2.42299900
F	4.71033900	-3.02650600	-4.15585000
F	6.93275000	-1.35518400	-4.17128000
F	7.03263000	0.85383700	-2.47635600
F	4.90216200	1.40896900	-0.79671300
F	4.00302400	-2.66623000	0.75482000
F	6.25573700	-3.09048000	2.30230900
F	7.22831700	-1.05736200	3.93879700
F	5.95321500	1.41618800	3.99665700
F	3.73838500	1.87003300	2.40162800
H	0.39875000	0.23298800	2.83683500
H	-1.33237500	-1.11855500	2.85141100

14. $[\mathrm{Fe^{III}Hpy}]^0$, Complex **B**
E = -5320.87251639 hartrees

Fe	0.00101800	0.26380500	-0.02070800
N	-1.38071600	0.04562200	-1.26563000
O	-1.25078800	0.00348600	-2.60686600
B	-0.00066900	0.68075700	-3.16209500
O	1.27559700	0.03063500	-2.60848600
N	1.40111300	0.05732300	-1.27148400
C	2.61288200	-0.19534800	-0.75923400
C	2.62491500	-0.18313700	0.68778200
N	1.41694800	0.04604400	1.20944600
O	1.27447100	0.03342500	2.54957500
O	-1.22938500	0.07141600	2.52618200
N	-1.39679200	0.05074500	1.23378600
C	-2.61327000	-0.18620300	0.69078900
C	-2.59199200	-0.20669700	-0.74904700
N	-0.01833500	2.31179600	0.13177700
C	-1.19906400	3.00027500	0.15615600
C	1.15483900	3.01373300	0.14408200
C	-1.24064000	4.40018300	0.19337900
H	-2.11268900	2.40491200	0.14756400
C	1.18162800	4.41401300	0.18163200
H	2.07491300	2.42854700	0.12338400
C	-0.03348500	5.12277900	0.20453100
H	-2.20743500	4.90783100	0.21111600
H	2.14278700	4.93256600	0.18916100
H	-0.03958000	6.21565900	0.23045000
F	0.00495800	0.42350100	-4.51066800
F	-0.00823000	2.03439900	-2.81397800

C	-3.76593900	-0.47439000	-1.60501600
C	-4.90326200	0.35362100	-1.57281400
C	-3.78272900	-1.55505800	-2.50987600
C	-6.01158500	0.13248500	-2.39854600
C	-4.87530300	-1.79585900	-3.35240300
C	-5.99361000	-0.94904800	-3.29338400
C	-3.79841800	-0.43933200	1.53341600
C	-4.24778800	0.51612500	2.46607800
C	-4.50145400	-1.65865600	1.48287800
C	-5.33779700	0.27770300	3.31134700
C	-5.60077600	-1.92210400	2.30984900
C	-6.01705800	-0.94833600	3.23080200
C	3.78917900	-0.46370000	-1.60995400
C	4.93252300	0.35587900	-1.56570200
C	3.80289800	-1.53585900	-2.52564400
C	6.04303900	0.13502900	-2.38835600
C	4.89703900	-1.77532400	-3.36659800
C	6.02113200	-0.93716300	-3.29440400
C	3.81350500	-0.44398700	1.52739800
C	4.50455700	-1.66947300	1.47237800
C	4.28462900	0.51565800	2.44419400
C	5.61486900	-1.93577800	2.28379300
C	5.38804400	0.27525800	3.27138100
C	6.05525100	-0.95743000	3.18874000
F	-7.09746900	-1.19331000	4.05284600
F	-6.26106400	-3.13382100	2.23855000
F	-4.07510300	-2.65752600	0.61000000
F	-5.75998100	1.24230300	4.20585100
F	-3.62163900	1.75542900	2.52398600
F	-7.07845800	-1.18148400	-4.11246500
F	-4.87072600	-2.86800200	-4.22125900
F	-7.10672000	0.97410000	-2.34885300
F	-4.91793100	1.45976500	-0.71982700
F	-2.70968200	-2.43010300	-2.54479600
F	2.72477400	-2.40393800	-2.57283000
F	4.88880600	-2.83880600	-4.24581100
F	7.10780800	-1.16916800	-4.11098600
F	7.14387900	0.96821900	-2.32533300
F	4.95051200	1.45433300	-0.70235600
F	4.05608200	-2.66804400	0.61169600
F	6.26340000	-3.15294000	2.21122700
F	7.14655700	-1.20510300	3.99428000
F	5.83237200	1.24246000	4.15121100
F	3.66208900	1.75612300	2.50816900
H	0.19895400	0.08983900	2.66966400
H	-0.01195400	-1.25044400	-0.01321300

15. [Fe^{0}py…H]$^{-}$, Complex **B**

E = -5320.99155268 hartrees

Fe	-0.00502700	0.23715400	0.08313000
N	-1.34962100	-0.08885200	-1.16768500
O	-1.25819200	-0.07282500	-2.53245800

B	0.01024500	0.50156900	-3.10414400
O	1.23153400	-0.15526200	-2.51916500
N	1.34063200	-0.08617900	-1.15790600
C	2.59960400	-0.26284600	-0.67787600
C	2.64394600	-0.18910100	0.75169600
N	1.41359000	-0.00078100	1.27581200
O	1.37661100	0.02968800	2.68159000
O	-1.30865800	-0.35160200	2.69205500
N	-1.38836300	-0.15808100	1.23656800
C	-2.64657900	-0.32991100	0.73071100
C	-2.61005400	-0.30242000	-0.69368100
N	-0.01927100	2.14952600	0.09705300
C	-1.21309900	2.83323800	0.12276800
C	1.14732500	2.87637200	0.04728200
C	-1.26646100	4.23102300	0.10450500
H	-2.11837600	2.22561800	0.15805900
C	1.14830700	4.27532400	0.03057100
H	2.07425200	2.30252400	0.01727200
C	-0.07248000	4.97663000	0.05799400
H	-2.24286600	4.72248100	0.12271700
H	2.10527400	4.80220300	-0.01107100
H	-0.09321200	6.06982700	0.03899500
F	0.00529000	0.16977700	-4.45828100
F	0.05525300	1.89615700	-2.89697700
C	-3.77164600	-0.44231200	-1.58790100
C	-4.86645900	0.44318900	-1.53693000
C	-3.83345000	-1.45762800	-2.56774200
C	-5.96192000	0.34228200	-2.40318500
C	-4.90732200	-1.57000900	-3.45900700
C	-5.97963600	-0.66933000	-3.37333100
C	-3.84554300	-0.50570200	1.55804400
C	-4.17725000	0.41551300	2.58308300
C	-4.74634900	-1.58362900	1.38826700
C	-5.31197800	0.27248900	3.38738900
C	-5.89932600	-1.73794500	2.16781700
C	-6.18293900	-0.80885400	3.17924000
C	3.75542400	-0.48963600	-1.55841400
C	4.88345100	0.35680400	-1.55015200
C	3.78648300	-1.55985400	-2.48139900
C	5.97620400	0.17077400	-2.40511800
C	4.85718800	-1.75672000	-3.36153100
C	5.96061300	-0.89125500	-3.32023600
C	3.85256500	-0.35808200	1.57622200
C	4.65306400	-1.51912500	1.50832200
C	4.27155300	0.63003500	2.49506000
C	5.79918400	-1.69406400	2.29426400
C	5.40299400	0.47399600	3.30369300
C	6.17439800	-0.69341100	3.20169500
F	-7.31403300	-0.95667900	3.96829800
F	-6.73880100	-2.82746900	1.97890500
F	-4.46444500	-2.58058100	0.45171800
F	-5.61136500	1.21353300	4.36305400
F	-3.39667500	1.55272900	2.76162500
F	-7.05683100	-0.78343600	-4.23950000

F	-4.94469600	-2.58874400	-4.39894100
F	-7.01336400	1.24658300	-2.32642500
F	-4.85675400	1.50457800	-0.62449600
F	-2.83473300	-2.41719600	-2.62580400
F	2.75888800	-2.49061800	-2.48933700
F	4.86204400	-2.82749600	-4.24296300
F	7.03521600	-1.08932400	-4.17482200
F	7.05817700	1.04150400	-2.37391100
F	4.90840800	1.46679600	-0.69751300
F	4.27972600	-2.56875300	0.66821300
F	6.54483700	-2.86180400	2.20869800
F	7.30255300	-0.85493800	3.99191100
F	5.79097700	1.47747500	4.18048400
F	3.58011200	1.83285200	2.57305500
H	0.39278700	0.04657800	2.85530200
H	-1.28218900	-1.32901900	2.78646600

16. $[\mathrm{Fe^{II}Hpy}]^{-}$, Complex **B**

E = 5320.99877613 hartrees

Fe	0.01207200	0.16116400	-0.00700400
N	-1.37592400	-0.04456000	-1.24502500
O	-1.25807900	-0.08915900	-2.59874500
B	0.00407500	0.52564800	-3.16899700
O	1.27695300	-0.07718500	-2.59388700
N	1.39317000	-0.03939100	-1.24290200
C	2.62373400	-0.22398700	-0.74026700
C	2.63571000	-0.19049400	0.71475000
N	1.41569400	0.00445500	1.22532200
O	1.26619500	-0.01283800	2.57218800
O	-1.22307900	0.01280900	2.56213800
N	-1.39266600	0.00453500	1.25623400
C	-2.61263800	-0.19197000	0.72368000
C	-2.59551100	-0.23010300	-0.73293300
N	-0.01992400	2.16620600	0.02836900
C	-1.20025600	2.86502500	0.02832000
C	1.15072300	2.88193200	0.03582400
C	-1.24222700	4.26488700	0.04229100
H	-2.11439400	2.27068200	0.01757600
C	1.17365400	4.28191300	0.04945100
H	2.07305900	2.29987900	0.02907200
C	-0.03959300	4.99574000	0.05248400
H	-2.21289700	4.76767100	0.04167400
H	2.13719300	4.79829000	0.05372300
H	-0.04733600	6.08946300	0.05988900
F	0.01071500	0.17871600	-4.51547400
F	0.00200200	1.91573300	-2.96194700
C	-3.78318700	-0.44129800	-1.58071100
C	-4.91014100	0.40156300	-1.50439400
C	-3.84509900	-1.48682500	-2.52835300
C	-6.03604500	0.23380700	-2.31890100
C	-4.95197900	-1.66660600	-3.36750200
C	-6.05446000	-0.80598000	-3.25950700
C	-3.79688000	-0.42935700	1.56719400

C	-4.19118500	0.49402400	2.56010000
C	-4.57254600	-1.60328900	1.46787800
C	-5.28024800	0.26313100	3.40926600
C	-5.67773800	-1.85142500	2.29156700
C	-6.03007500	-0.91435700	3.27304800
C	3.80811200	-0.43366700	-1.58880700
C	4.94228800	0.40002000	-1.50403600
C	3.86424300	-1.47023800	-2.54795400
C	6.06698900	0.23303700	-2.32001900
C	4.96938000	-1.64754700	-3.38973500
C	6.07817500	-0.79606400	-3.27256100
C	3.81983800	-0.43375800	1.56009200
C	4.57981800	-1.61779700	1.46410000
C	4.23712300	0.49946000	2.53309600
C	5.69304300	-1.86682700	2.27692300
C	5.33691900	0.26959400	3.36854100
C	6.07066500	-0.91874900	3.23832200
F	-7.11860800	-1.14692800	4.09994900
F	-6.40491600	-3.02710600	2.16703300
F	-4.21407700	-2.59193100	0.54998600
F	-5.64686100	1.20261200	4.36223100
F	-3.52666800	1.70828500	2.67327300
F	-7.16061600	-0.98469100	-4.07555300
F	-4.98781400	-2.71190100	-4.27681700
F	-7.11708300	1.09898900	-2.22146900
F	-4.90132500	1.48537100	-0.61997700
F	-2.81269800	-2.40709500	-2.60651200
F	2.82827500	-2.38607600	-2.63266600
F	4.99887800	-2.68444900	-4.30885400
F	7.18328500	-0.97382300	-4.09032800
F	7.15403500	1.08975400	-2.21310000
F	4.94073900	1.47585400	-0.60913400
F	4.19943000	-2.61087600	0.56207900
F	6.40452000	-3.05183800	2.15968200
F	7.16697700	-1.15237400	4.05323500
F	5.72657300	1.21755300	4.30269300
F	3.57813200	1.71660900	2.64455000
H	0.17107200	0.02381700	2.67665000
H	-0.01846300	-1.36254700	0.03496200

17. [Fe^{II}Hpy…H] , Complex **B**

E = -5321.45835734 hartrees

Fe	-0.01335100	0.20313200	0.08640400
N	-1.38842100	-0.00029300	-1.15631200
O	-1.27303300	-0.03049100	-2.49334500
B	-0.02549300	0.62034200	-3.08765600
O	1.23754100	-0.01061400	-2.52112600
N	1.36733600	0.01022300	-1.18309100
C	2.60159300	-0.19427000	-0.71147700
C	2.65156400	-0.18867900	0.74219000
N	1.46096000	0.00734800	1.28917600
O	1.41691300	-0.03620600	2.66981500
O	-1.32325700	0.05737700	2.69732500

N	-1.45221900	0.03395400	1.27312500
C	-2.66333800	-0.19392900	0.76145700
C	-2.62918100	-0.23048100	-0.68178000
N	0.03904400	2.22397200	0.14442900
C	-1.13130000	2.93746600	0.13691700
C	1.21998400	2.91775800	0.14517100
C	-1.15303400	4.33776100	0.13571000
H	-2.05548700	2.35901000	0.12412800
C	1.26402100	4.31812700	0.14451800
H	2.13585500	2.32664800	0.14225100
C	0.06162700	5.04794400	0.13886000
H	-2.11458300	4.85640800	0.12515100
H	2.23405100	4.82067700	0.14269000
H	0.07058400	6.14096200	0.13243500
F	-0.04082400	0.29969000	-4.42625000
F	-0.03850400	1.98970000	-2.81761500
C	-3.78606000	-0.48847400	-1.55812600
C	-4.92706000	0.33692100	-1.54332800
C	-3.78882200	-1.55973800	-2.47704100
C	-6.01761000	0.12764000	-2.39523600
C	-4.85933300	-1.78429300	-3.35166600
C	-5.97928100	-0.93880500	-3.30702800
C	-3.87747300	-0.42776200	1.57575700
C	-4.40011900	0.56910400	2.42907900
C	-4.59936500	-1.63809200	1.49510700
C	-5.57602500	0.37770800	3.16552100
C	-5.78215300	-1.85206900	2.21486200
C	-6.27012100	-0.83814800	3.05459900
C	3.76431100	-0.42046500	-1.59089000
C	4.88882000	0.42608400	-1.55985000
C	3.79191200	-1.48257000	-2.51914400
C	5.98948000	0.24415900	-2.40488100
C	4.87411500	-1.68103600	-3.38581100
C	5.97817300	-0.81609400	-3.32461200
C	3.87448500	-0.43611100	1.53781800
C	4.58459400	-1.64819800	1.44020100
C	4.37151200	0.52350200	2.44112500
C	5.73714300	-1.90103300	2.19521400
C	5.51746800	0.29590700	3.21270300
C	6.20298700	-0.92266000	3.08698500
F	-7.42733300	-1.03810400	3.77499400
F	-6.45424300	-3.05387500	2.12129000
F	-4.11292200	-2.66998400	0.69976500
F	-6.06380800	1.37728300	3.98282800
F	-3.75703000	1.79635200	2.51570500
F	-7.04638600	-1.15992000	-4.15359800
F	-4.83652700	-2.84626100	-4.23384800
F	-7.11539600	0.96817100	-2.35556800
F	-4.96430000	1.43356600	-0.67555700
F	-2.72164000	-2.44292400	-2.49619000
F	2.74029700	-2.38340500	-2.55620300
F	4.87728200	-2.73540200	-4.27755700
F	7.05561500	-1.01047700	-4.16477000
F	7.07033500	1.10538700	-2.35146600

F	4.89620800	1.51692400	-0.68515400
F	4.11357000	-2.64970000	0.59532500
F	6.40215000	-3.10677600	2.08220800
F	7.33523800	-1.15761000	3.83913700
F	5.98418800	1.26307100	4.08197500
F	3.73097300	1.75117100	2.55214200
H	0.43999700	0.02835500	2.85957000
H	-1.88872100	-0.66607600	3.05524500
H	0.02399500	-1.31918800	0.12006700

A.4. Reference

1. Solis, B. H.; Hammes-Schiffer, S., Substitution effects on cobalt diglyoxime catalysts for hydrogen evolution. *J. Am. Chem. Soc.* **2011,** *133*, 19036-19039.

APPENDIX B: Supporting Information for Chapter 3[§]

B.1. Materials and Methods

B.1.1. Computational methods

The nomenclature for all systems used hereafter is fully described in the main text. The systematic net dehydrogenation of the unit cell used in calculations was described by corresponding proton-coupled redox potentials. The potentials are computed relative to the $Ni^{2+/3+}$ potential, which was measured experimentally. The scheme utilized in this work for computing relative proton-coupled redox potentials is presented below. For the 5H state of the NiFe system, several hydrogen configurations close in energy were found, thereby complicating straightforward interpretation.

As discussed in the main text, assigning oxidation states to species in condensed phases is a challenging task, and thus we verified the consistency of results obtained with different approaches. Here, we briefly describe a method that is based on calculations of maximally localized Wannier functions (MLWFs).[1-2] In this scheme, the centers of MLWFs are computed for the valence states of the system, and those located in the close proximity of the transition metal ions are identified and used to define site-specific magnetizations and oxidation states. In particular, the magnetic moment (μ) associated with a certain site is computed by subtracting the number of spin down MLWF centers from the number of spin up MLWF centers associated with the site: $\mu = N_\uparrow - N_\downarrow$. The oxidation state ($OS$) is defined as the number of valence electrons of the ion of interest minus the total number of MLWF centers associated with that site: $OS = N_{valence} - (N_\uparrow + N_\downarrow)$. This intuitive approach was shown to give results in agreement with other methods for iron complexes and cobalt oxides, and it is expected that this method allows for assigning atomic oxidation states unambiguously for other strongly ionic systems as well.[1, 3]

[§] Reproduced with permission from:
Goldsmith, Z. K.; Harshan, A. K.; Gerken, J. B.; Vörös, M.; Galli, G.; Stahl, S. S.; Hammes-Schiffer, S. *Proc. Natl. Acad. Sci. U.S.A.* **2017,** *114* (12), 3050-3055. Copyright 2017 National Academy of Sciences

We computed magnetizations and oxidation states for the $n = 4$ system with and without iron using the Wannier method. The results are compared to the approach used in the main text (which we call "Spin density" approach) in Table B.2. To compute MLWFs, we used the QBOX code[4-5] with the same pseudopotentials that were used for our calculations with Quantum-ESPRESSO: the unit cell described in the Chapter 3, the PBE0 hybrid functional, Gamma-point only Brillouin zone sampling (verifying that the Gamma-point sampling gives accurate site-specific magnetizations and oxidation states), and a reduced wave function energy cutoff of 60 Ry. As Table B.3 shows, the Wannier method agrees well with the analysis based on the integrated spin densities.

B.1.2. Experimental details

Stock solutions of Fe-free KOH in water were prepared by the method of Boettcher and co-workers.[6] Samples of $Ni(OH)_2$ were prepared by addition of a 0.1 M $Ni(NO_3)_2$ solution to an excess of Fe-free 1 M KOH. The lime-green precipitate was filtered and rinsed. NiOOH was prepared by a similar precipitation, followed by addition of 0.5 equivalents of $K_2S_2O_8$ in water. On addition, the lime-green $Ni(OH)_2$ promptly darkened to black. Filtration yielded a fine solid suitable for spectroscopy. Samples of nominal composition $Ni_{0.75}Fe_{0.25}(OH)_2$ were prepared by a similar process starting from a solution containing $Ni(NO_3)_2$ and $FeSO_4$ in 3:1 ratio. The precipitate exhibited a color change, gaining a yellow tint, during its isolation that suggested the formation of Fe^{3+}. Further oxidation to $Ni_{0.75}Fe_{0.25}OOH$ was effected with $K_2S_2O_8$ as above to yield a purplish black solid. Ex-situ spectra were obtained by diffuse-reflectance measurements of films of slurries of the precipitated materials in Fe-free 1 M KOH between silica plates (Figures B.6 and B.7). Because of the variable thickness of the different slurries, no attempt was made to calculate molar absorptivity values.

Spectroelectrochemistry was performed on films of $Ni_{1-x}Fe_x(OH_{1-y})_2$ deposited on a FTO-on-glass transparent electrode. The (hydr)oxide films were produced by anodic decomposition of deposits of metal acetylacetonate complexes in the desired stoichiometry using the following procedure. A solution of 50 mM $Ni(acac)_2$ in 1:1 iPrOH:CH_3CN with 5 µl/ml of poly(tetrahydrofuran) ($M_n \sim 250$) added was coated on the electrode, allowed to dry to a film, and the excess was wiped off. The electrode was placed in Fe-free 1 M KOH and CV was performed until the shape of the peaks was consistent from scan to scan (~ 3 cycles). Any NiOOH formed that was not part of an adherent film was wiped off and the process repeated until a sufficiently dark film was produced (12 - 20 layers). $Ni_{1-x}Fe_x(OH_{1-y})_2$ films were produced in a similar process using a deposition solution composed of the appropriate mixture of $Ni(acac)_2$ and $Fe(acac)_3$ stock solutions. Once formed, the catalyst films were placed in fresh Fe-free 1 M KOH in a cuvette constructed from a 50 ml polystyrene culture flask. A Pt wire separated by a polyethylene frit was used as the counter electrode and a 1 M KOH Hg/HgO reference electrode was used. Potentials are reported vs. NHE (Hg/HgO in 1 M KOH + 140 mV).[7] The electrode was held at a given potential until the current reached steady-state (2 - 5 minutes) and then a spectrum was obtained while holding that potential. Molar absorptivities (on a per-metal basis) were calculated based on the area of the cathodic peak in the CV and assume that this peak arises from a $1e^-$/Ni atom process.

B.1.3. Calculation of proton-coupled redox potentials using a reference reaction

Scheme B1. Reaction of interest, reference reaction, and relative reaction.

$$
\begin{array}{ccccccc|c}
\frac{n'}{n}\big[\mathrm{MO}_x\mathrm{H}_{y-n} & + & \frac{n}{2}\mathrm{H}_2 & \rightarrow & \mathrm{MO}_x\mathrm{H}_y\big] & & & \frac{n'}{n}\Delta G^{\mathrm{o}} \\
\mathrm{MO}_x\mathrm{H}_{y'} & & & \rightarrow & \mathrm{MO}_x\mathrm{H}_{y'-n'} & + & \frac{n'}{2}\mathrm{H}_2 & -\Delta G^{\mathrm{o}}_{\mathrm{ref}} \\
\hline
\mathrm{MO}_x\mathrm{H}_{y'} & + & \frac{n'}{n}\mathrm{MO}_x\mathrm{H}_{y-n} & \rightarrow & \mathrm{MO}_x\mathrm{H}_{y'-n'} & + & \frac{n'}{n}\mathrm{MO}_x\mathrm{H}_y & \Delta G^{\mathrm{o}}_{\mathrm{rel}}
\end{array}
$$

The first reaction is the reaction of interest, and the second reaction is the reference reaction. All free energies shown here correspond to reduction free energies. When adding the two reactions, the H_2 on both sides cancel because the first line is multiplied by n'/n, leading to:

$$\Delta G^{\mathrm{o}}_{\mathrm{rel}} = \frac{n'}{n}\Delta G^{\mathrm{o}} - \Delta G^{\mathrm{o}}_{\mathrm{ref}} \ . \qquad \text{(B1)}$$

The free energies for the reaction of interest and the reference reaction are related to the reduction potentials as follows:

$$E^{o} = -\frac{\Delta G^{o}}{nF} \qquad E^{o}_{\text{ref}} = -\frac{\Delta G^{o}_{\text{ref}}}{n'F}, \tag{B2}$$

F is the Faraday constant. Here E^{o}_{ref} is the experimental value for the reference reaction reduction potential. Plugging these expressions into Eq. (B1) gives the expression for the reduction potential for the reaction of interest:

$$E^{o} = -\frac{\Delta G^{o}_{\text{rel}}}{n'F} + E^{o}_{\text{ref}}. \tag{B3}$$

Note that the number of OH bonds is the same on the right and left sides of the relative reaction shown on the last line of Scheme B1. For solids, the relative electronic energy change obtained from DFT at 0 K is a reasonable approximation for the relative free energy change in the last line of Scheme B1. For this reaction, the number of OH bonds and all other types of bonds is the same for reactants and products, resulting in a negligible change in zero point energy and vibrational entropy, and translational and rotational entropy effects are negligible because H_2 is not part of this reaction. Thus,

$$\Delta G^{o}_{\text{rel}} \approx \Delta U^{o}_{\text{rel}} = \frac{n'}{n}\Delta U^{o} - \Delta U^{o}_{\text{ref}}, \tag{B4}$$

where ΔU^{o} and $\Delta U^{o}_{\text{ref}}$ correspond to the change in electronic energies for the processes

$$\begin{array}{ll} \text{MO}_x\text{H}_{y-n} \rightarrow \text{MO}_x\text{H}_y & \Delta U^{o} \\ \text{MO}_x\text{H}_{y'-n'} \rightarrow \text{MO}_x\text{H}_{y'} & \Delta U^{o}_{\text{ref}} \end{array} \tag{B5}$$

Note that the two processes in Eq. (B5) have different numbers of atoms on the left and right sides, but such effects cancel out in this scheme. Substituting Eq. (B4) into Eq. (B3),

$$E^{o} = -\frac{\Delta U^{o}}{nF} + \frac{\Delta U^{o}_{\text{ref}}}{n'F} + E^{o}_{\text{ref}} = -\frac{\Delta U^{o}}{nF} + E_{\text{corr}}. \tag{B6}$$

The correction factor, $E_{\text{corr}} = E^{o}_{\text{ref}} + \frac{\Delta U^{o}_{\text{ref}}}{n'F}$, is the difference between the experimental and calculated reduction potentials for the reference reaction. All calculations must be performed using the same cell and the same computational parameters with the same code to ensure proper cancellation of zero reference energies.

B.2. Figures

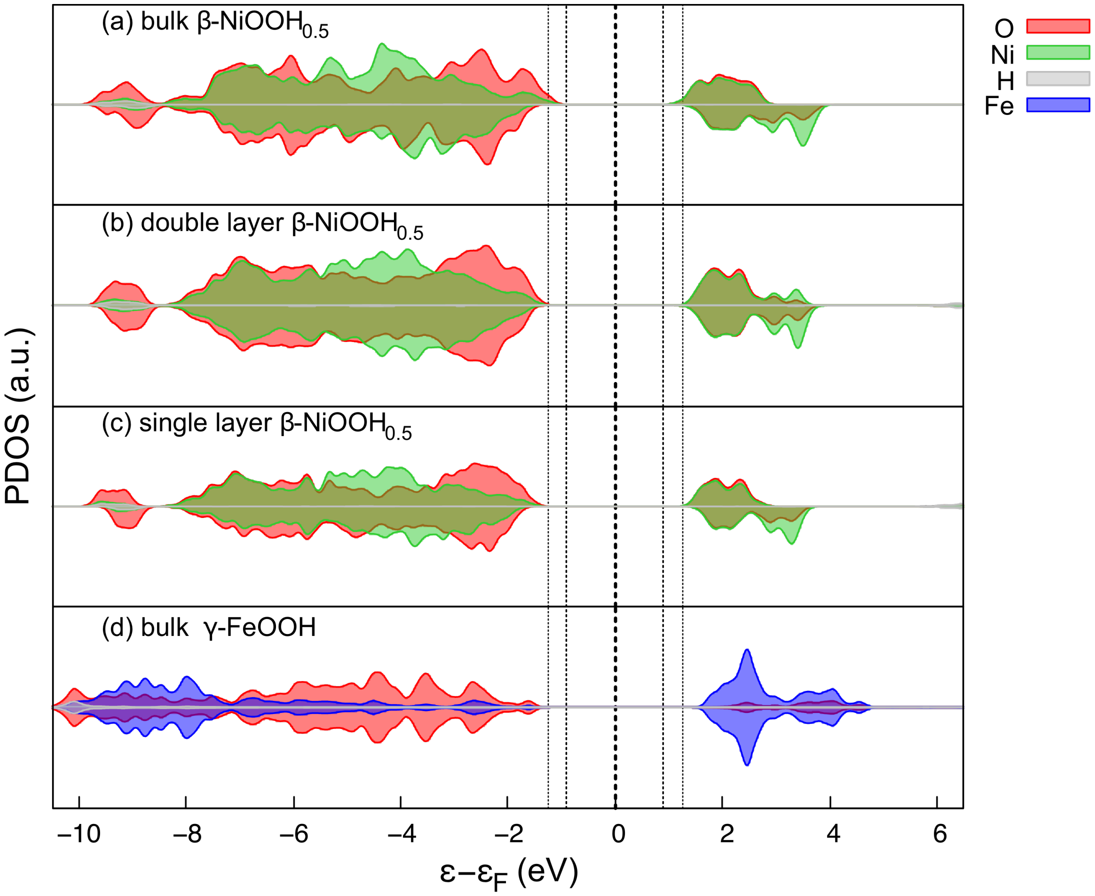

Figure B.1. Projected density of states (PDOS) for (a) bulk (42 atom unit cell 3D-periodic), (b) double layer (28 atom unit cell 2D-periodic), (c) single layer (14 atom unit cell 2D-periodic), β-NiOOH$_{0.5}$, and (d) bulk γ-FeOOH as calculated with PBE0. The bulk calculations are periodic in all three dimensions with no vacuum in between layers. The single layer calculations are the same as described in the Chapter 3, and the double layer calculations just replace the single layer with a double layer. The similarities among these different types of calculations indicates that interlayer hydrogen-bonding interactions do not qualitatively impact the PDOS. Part (c) is the same as the top panel of Figure 3.5a in Chapter 3 but is expanded along the abscissa here.

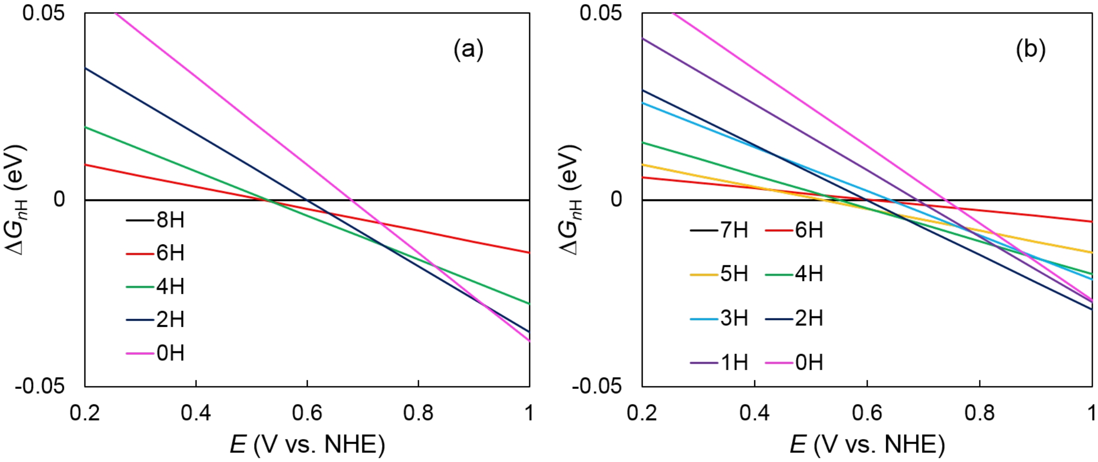

Figure B.2. Plots of the relative formation free energies versus potential for (a) the pure Ni system and (b) the Fe-doped system. The relative formation free energy is defined to be $\Delta G_{nH} = 0.59\frac{\Delta n}{4}\left(E_{nH} - E\right)$ where E is the applied potential, Δn is the difference in the number of H atoms in the unit cell of the least oxidized species (8H for pure and 7H for doped) relative to that of the nH, and E_{nH} is the calculated proton-coupled redox potential for the reaction associated with converting the least oxidized species to the nH species. The least oxidized species corresponds to the black horizontal line at $\Delta G_{nH} = 0$, and the other lines intersect this horizontal line at the potential associated with converting the least oxidized species to the nH species. At any applied potential E, the species associated with the lowest value of ΔG_{nH} is the most thermodynamically stable species at pH 14. Thus, the information provided herein corresponds to a one-dimensional slice of a Pourbaix diagram.

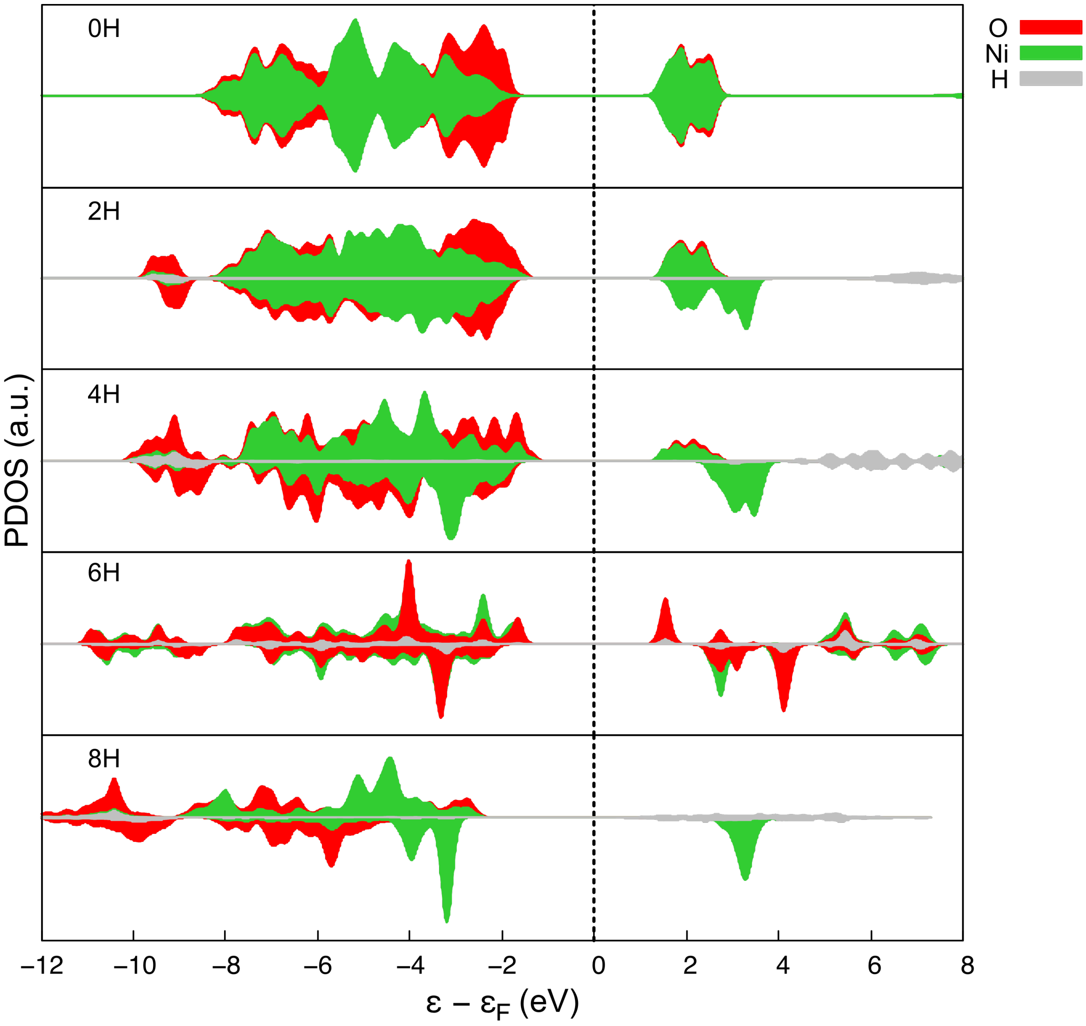

Figure B.3. PDOS analysis for $Ni_4O_8H_n$ calculated with PBE0 functional. The Fermi level is represented by the dotted line.

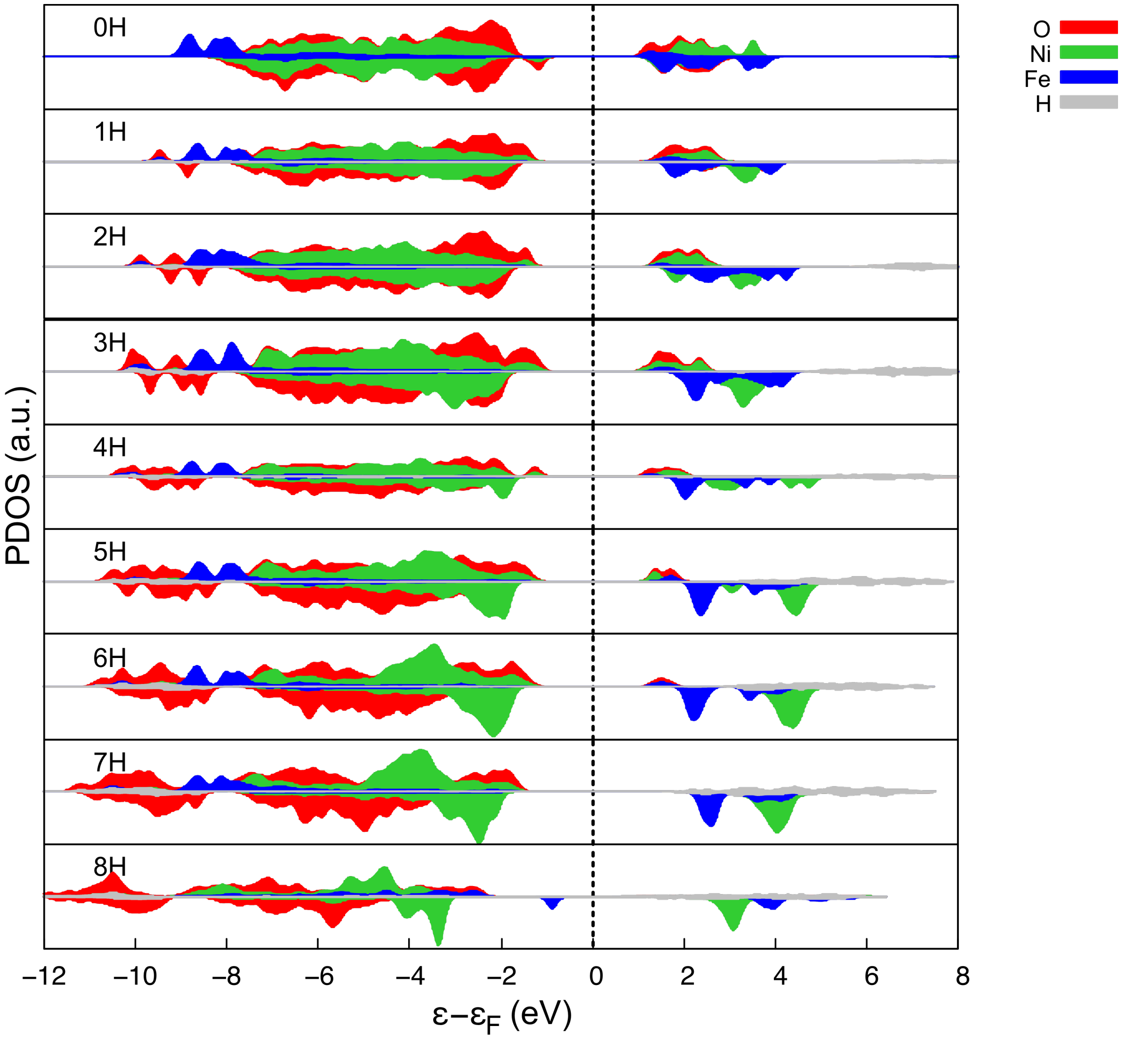

Figure B.4. PDOS analysis for $Ni_3Fe_1O_8H_n$ calculated with PBE0 functional. The Fermi level is represented by the dotted line.

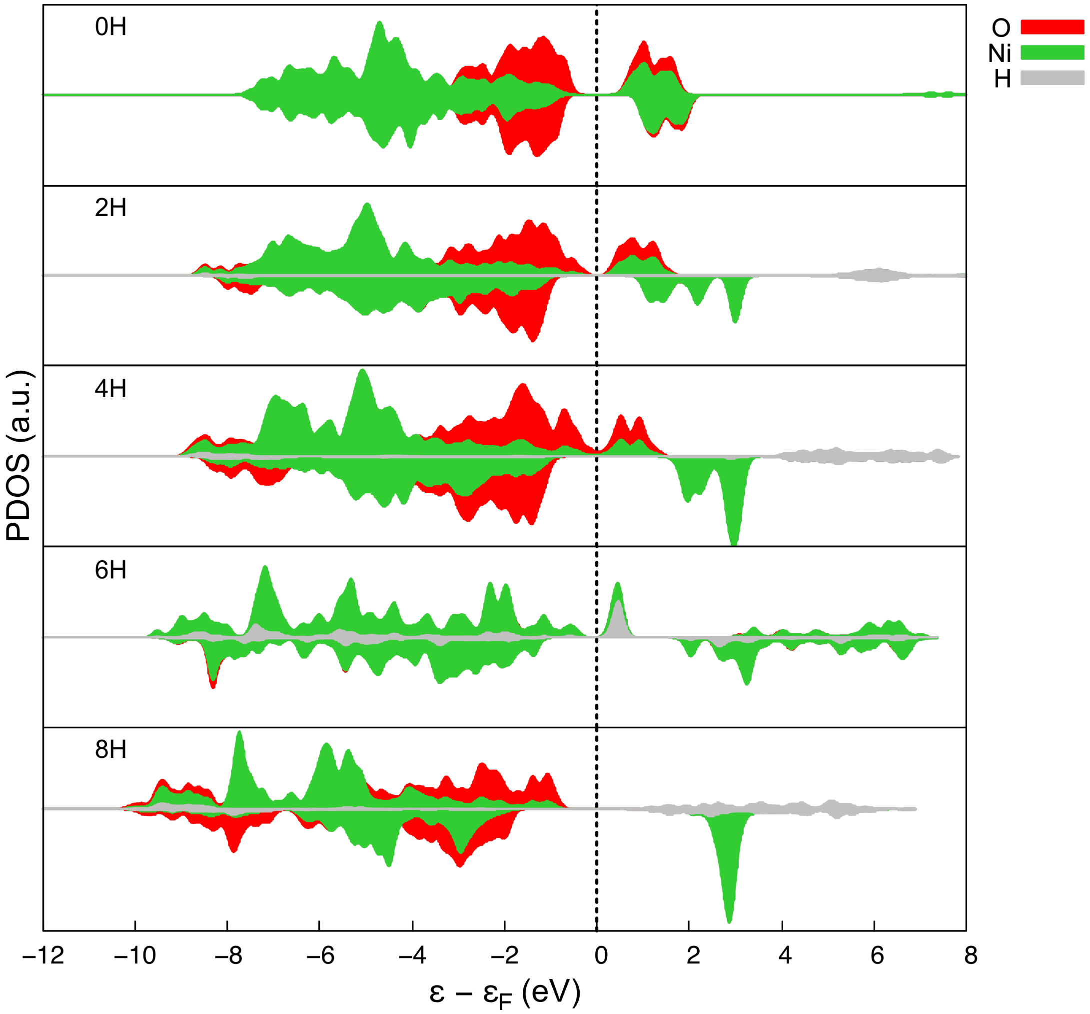

Figure B.5. PDOS analysis for $Ni_4O_8H_n$ calculated with PBE+U functional. The Fermi level is represented by the dotted line. Note that the energy gap nearly vanishes for some stoichiometries, suggesting that this level of theory is not adequate.

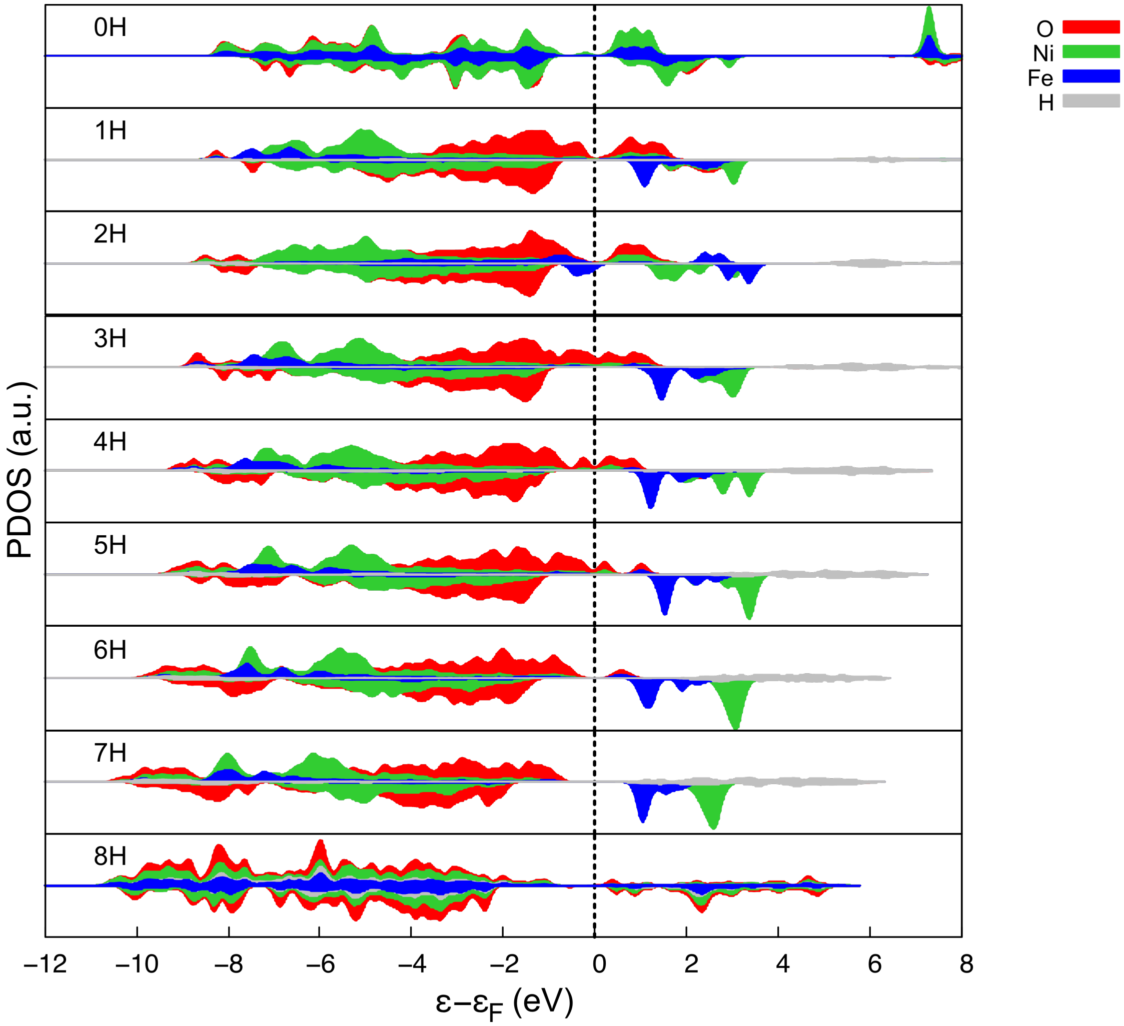

Figure B.6. PDOS analysis for $Ni_3Fe_1O_8H_n$ calculated with PBE+U functional. The Fermi level is represented by the dotted line. Note that the energy gap nearly vanishes for some stoichiometries, suggesting that this level of theory is not adequate.

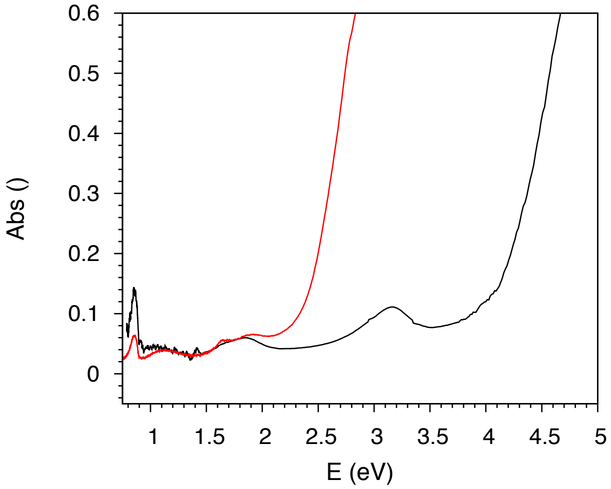

Figure B.7. Diffuse reflectance spectrum of a bulk sample of $Ni(OH)_2$ (black trace), various symmetry-forbidden transitions can be observed at energies lower than the band edge of *ca.* 4 eV. Collectively, these give rise to the pale lime-green color of nickel hydroxide. After precipitation of $Ni_3Fe_1O_8H_8$, the solid develops a rufous color due to aerobic oxidation. The resulting mixed oxidation-state results in a lower band edge of *ca.* 2 eV (red trace). At lower energies, some of the transitions observed in $Ni(OH)_2$ can still be observed.

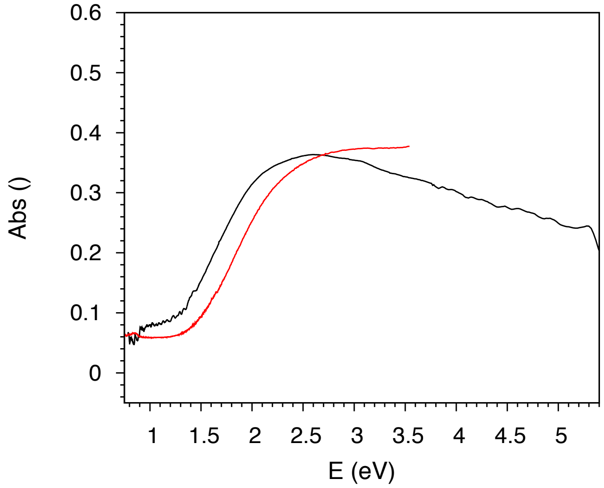

Figure B.8. Diffuse reflectance spectra after oxidation of the bulk samples ($Ni_4O_8H_4$ black trace, nominally $Ni_3Fe_1O_8H_4$ red trace). The oxidized materials have band edges of *ca.* 1.5 eV, leading to their purplish or brownish black colors. The oxidized Fe-containing material reacts with water, a process that leads to the catalytic currents observed in the CV experiments. This reaction leads to the partial reduction of the sample to a composition between $Ni_3Fe_1O_8H_4$ and $Ni_3Fe_1O_8H_7$.

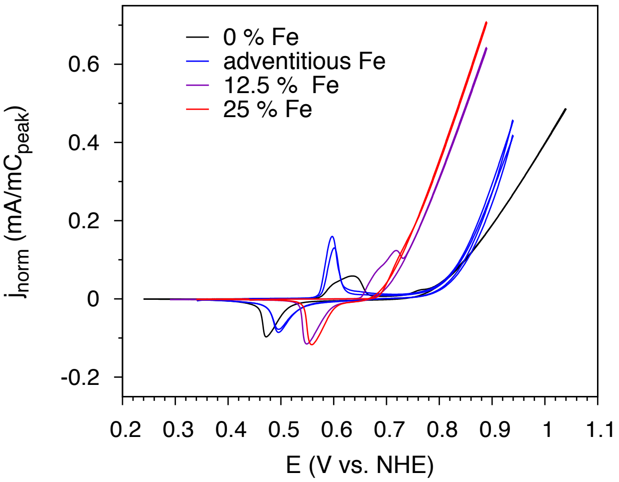

Figure B.9. Cyclic voltammagrams of NiFe systems with all levels of Fe doping studied, including adventitious amounts of Fe and 12.5% Fe. Experimental details are identical to those in Fig. 3.1 in the main text. Current densities are normalized to the peak area of the cathodic peak.

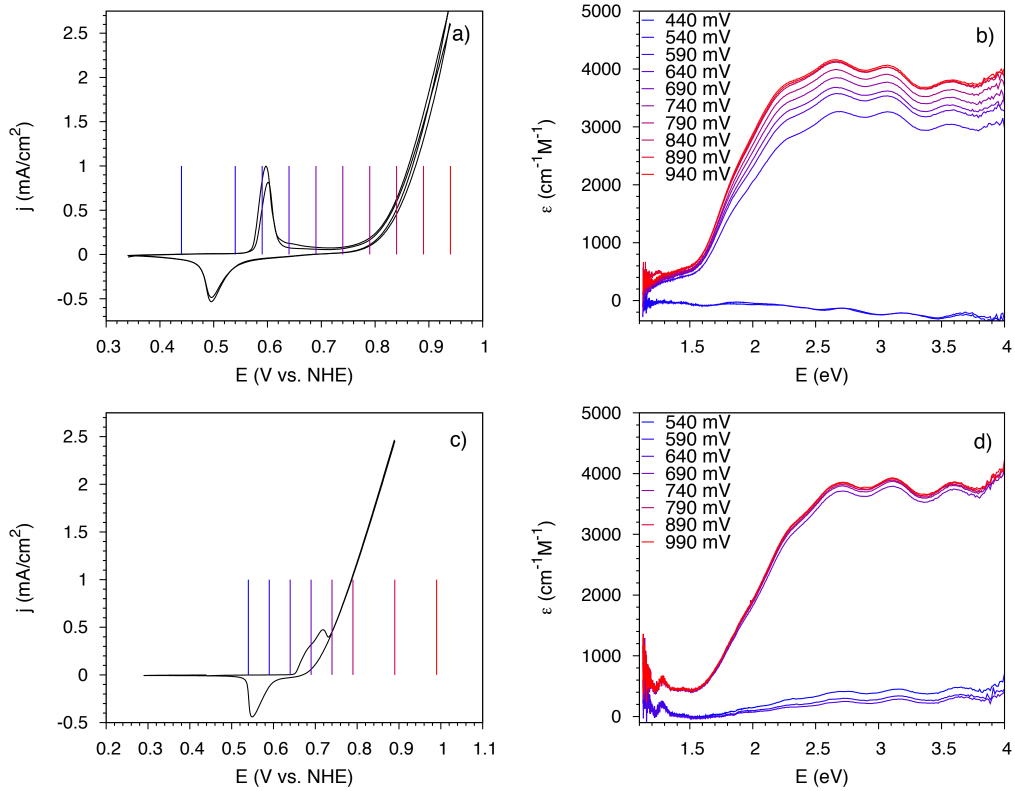

Figure B.10. Cyclic voltammograms of the (a) adventitious levels of Fe (cf. Ref. [6]) and (c) 12.5 % Fe films with lines indicating the potentials where spectra (b and d, respectively) were obtained at steady-state during constant-potential electrolysis.

B.3. Tables

Table B.1. Ni−O and Fe−O bond lengths for $n = 8$ ($Ni(OH)_2$) and $n = 2$ ($NiOOH_{0.5}$) calculated with PBE+U and PBE0

		Bond lengths (Å)			
Structure	Functional	$Ni-O_1$	$Ni-O_2$	$Ni-O_3$	O−H
$Ni_4O_8H_8$	PBE+U	2.03	2.03	2.03	0.96
	PBE0	2.00	2.00	2.00	0.95
$Ni_4O_8H_2$	PBE+U	2.10	1.91	1.94	0.97
	PBE0	2.08	1.87	1.90	0.96

Table B.2. Magnetizations calculated with PBE+U and PBE0. All the configurations investigated here are ferromagnetic, because the antiferromagnetic and ferromagnetic configurations were shown to be near identical energetically[8] and could interchange/coexist in room temperature conditions

	PBE+U				PBE0			
$Ni_4O_8H_n$ [a]	Ni	Ni	Ni	Ni	Ni	Ni	Ni	Ni
8H	1.63	1.63	1.64	1.64	1.67	1.67	1.67	1.67
6H	1.15	1.16	1.62	1.62	0.92	0.93	1.62	1.62
4H	1.07	1.08	1.15	1.15	0.87	0.87	0.93	0.93
2H	0.24	0.24	1.14	1.14	0.01	0.01	0.91	0.91
0H	0.16	0.16	0.17	0.17	0.00	0.00	0.00	0.00

	PBE+U				PBE0			
$Ni_3Fe_1O_8H_n$ [a]	Fe	Ni	Ni	Ni	Fe	Ni	Ni	Ni
8H	3.27	1.63	1.63	1.64	3.43	1.67	1.67	1.67
7H	3.76	1.67	1.67	1.68	3.82	1.66	1.66	1.67
6H	3.25	1.64	1.64	1.64	3.25	1.66	1.66	1.66
5H	3.15	1.28	1.65	1.66	3.24	0.92	1.62	1.63
4H	3.20	1.18	1.18	1.63	3.33	0.89	0.89	1.61
3H	3.20	1.07	1.18	1.32	3.33	0.86	0.88	0.94
2H	3.27	0.52	1.10	1.19	3.32	0.01	0.88	0.88
1H	2.60	0.34	1.08	1.21	2.70	0.01	0.87	0.91
0H	2.85	0.24	0.25	1.17	2.88	0.01	0.01	0.88

[a] The stoichiometry of the film is represented by nH.

Table B.3. Magnetizations and oxidation states calculated with the integrated spin density approach, compared with those calculated using the Wannier method

	Spin density				Wannier			
$Ni_4O_8H_4$	Ni	Ni	Ni	Ni	Fe	Ni	Ni	Ni
Magnetization	0.87	0.87	0.93	0.93	1	1	1	1
Oxidation state	3	3	3	3	3	3	3	3
	Spin density				Wannier			
$Ni_3Fe_1O_8H_4$	Fe	Ni	Ni	Ni	Fe	Ni	Ni	Ni
Magnetization	3.33	0.89	0.89	1.61	4	1	1	2
Oxidation state	4	3	3	2	4	3	3	2

Table B.4. Proton-coupled redox potentials for pure $Ni_4O_8H_n$ [a] and 25% Fe- doped $Ni_3Fe_1O_8H_n$ calculated with PBE+U [b]

$Ni_4O_8H_n$			$Ni_3Fe_1O_8H_n$		
Reactant	Products	E (V)	Reactant	Products	E (V)
8H	6H + H_2	0.55	8H	7H + 0.5 H_2	−0.34
	4H + 2 H_2	0.53 [c]	7H	6H + 0.5 H_2	0.11
	2H + 3 H_2	0.55		5H + 1 H_2	0.27
6H	4H + H_2	0.50		4H + 1.5 H_2	0.36
4H	2H + H_2	0.61		3H + 2 H_2	0.47
2H	0H + H_2	0.75		2H + 2.5 H_2	0.46
				1H + 3 H_2	0.49
				0H + 3.5 H_2	0.53

[a] In the reactant and products, nH denotes the stoichiometry of the film.

[b] The PBE0 results given in Table 3.1 and are more consistent with the experimental cyclic voltammetry.

[c] This potential is set equal to the experimental value, and all other reported potentials are calculated relative to this value.

Table B.5. Proton-coupled redox potentials for pure $Ni_4O_8H_n$ and 25% Fe- doped $Ni_3Fe_1O_8H_n$ calculated with PBE0 using 8H → 2H + 3 H_2 as the reference reaction [a]

$Ni_4O_8H_n$			$Ni_3Fe_1O_8H_n$		
Reactant	Products	*E* (V)	Reactant	Products	*E* (V)
8H	6H + H_2	0.46	8H	7H + 0.5 H_2	−0.78
	4H + 2 H_2	0.47	7H	6H + 0.5 H_2	0.54
	2H + 3 H_2	0.53 [b]		5H + 1 H_2	0.46
6H	4H + H_2	0.48		4H + 1.5 H_2	0.49
4H	2H + H_2	0.67		3H + 2 H_2	0.57
2H	0H + H_2	0.86		2H + 2.5 H_2	0.54
				1H + 3 H_2	0.63
				0H + 3.5 H_2	0.67

[a] In the reactant and products, *n*H denotes the stoichiometry of the film.

[b] This potential is set equal to the experimental value at pH 14, and all other reported potentials are calculated relative to this value. The analogous table using the 8H → 4H + 2 H_2 reaction as the reference is given as Table 3.1 of the Chapter 3, shifting all potentials upward by 0.06 V.

Table B.6. Ni−O and Fe−O bond lengths (Å) for selected systems containing Ni^{2+}, Ni^{3+}, Ni^{4+}, Fe^{3+} and Fe^{4+} from experiment[a] and calculated with PBE+U[b, c]

Pure					Doped		
Structure	Expt.[a]		Calc.		Structure	Calc.[d]	
	Ni−O	Ni−O	Ni−O	Ni−O		Fe−O	Fe−O
$Ni_4O_8H_8$ (Ni^{2+})	2.06	N/A	2.03	N/A	$Ni_3Fe_1O_8H_7$ (Fe^{3+})	2.07	N/A
$Ni_4O_8H_4$ (Ni^{3+})	2.07	1.89	2.05	1.91	$Ni_3Fe_1O_8H_4$ (Fe^{4+})	2.09	1.88
$Ni_4O_8H_2$ (Ni^{4+})	N/A	N/A	1.90	N/A			

[a] XAFS data taken from Ref.[9]. $Ni_4O_8H_4$ is compared to the results for *β*-NiOOH presented in this reference.

[b] Oxidation states determined by the magnetization analysis.

[c] Calculated values shown are the average of the six M−O bonds if there is no quasi Jahn-Teller effect, resulting in a single bond length reported and N/A given for the other column, or the averages of two long and four short M−O bonds if there is a quasi Jahn-Teller effect, resulting in two different bond lengths reported.

[d] Experiments show a contraction of the Fe−O bond lengths from 2.01 Å to 1.90 Å upon oxidation of the Fe-doped system.[10]

Table B.7. Band gaps (eV) calculated with PBE0

nH	$Ni_4O_8H_n$		$Ni_3Fe_1O_8H_n$	
	Direct	Indirect	Direct	Indirect
8H	3.17	3.17	1.67	1.66
7H			3.40	3.40
6H	2.92	2.80	2.94	2.55
5H			2.64	2.49
4H	2.75	2.65	2.42	2.22
3H			2.42	2.22
2H	2.96	2.96	2.81	2.74
1H			2.83	2.70
0H	3.37	3.32	2.44	2.40

B.4. Additional Computational Details and Geometries

Cartesian coordinates of all structures and energies calculated from gas phase optimizations performed with PBE+*U* functional. The single-point energies calculated with PBE0 for the same geometries are also given. The unit cell parameters used for all cases are $a = 5.82499$, $b = 5.02802$ and $c = 14.1643$.

$Ni_4O_8H_n$ single layer

$n = 0$

−1487.2979068089 Ry (PBE+*U*)

−1487.51066769 Ry (PBE0)

Ni	0.01795196	1.666201339	4.697450092
Ni	1.47440881	4.179413533	4.698023603
Ni	2.930476273	1.666240738	4.69735816
Ni	4.387068007	4.18102574	4.696664152
O	5.843119798	5.017433103	5.61312807
O	1.474287916	2.503016233	5.613648283
O	0.019733405	3.342135734	3.781255112
O	1.475015334	0.827863807	3.781627127
O	2.931025098	5.017621455	5.613035515
O	4.386821118	2.503903706	5.613158873
O	2.932008642	3.342424432	3.781702693
O	4.388019103	0.829037737	3.780789681

$n = 2$

−1489.9159953801 Ry (PBE+*U*)

−1490.16296813 Ry (PBE0)

Ni	0.023082056	1.666133910	4.697584005
Ni	1.476884594	4.220312775	4.729792512
Ni	2.935341086	1.665724032	4.696734136
Ni	4.389880746	4.139022588	4.664760131
O	5.810010499	4.992797428	5.626852872
O	1.481911615	2.672769948	5.829448845
O	0.055918697	3.366808070	3.767881196
O	1.479871716	0.826605634	3.785137508
O	2.968487966	4.993925031	5.623951685
O	4.392118202	2.503922888	5.609446622
O	2.897072200	3.366662834	3.768742200
O	4.394029083	0.657954553	3.565965762
H	1.467151744	2.910876387	6.770673136
H	4.395466725	0.421055882	2.624656899

$n = 4$

−1492.5129464143 Ry (PBE+*U*)

−1492.78735597 Ry (PBE0)

Ni	0.000550424	1.659939586	4.69764892
Ni	1.459237757	4.171604892	4.707930916
Ni	2.913093818	1.659589315	4.699358559
Ni	4.372394828	4.177971661	4.697823131
O	5.835012452	5.052125081	5.600123071
O	1.399095359	2.39901982	5.862986436
O	-0.004148605	3.300007003	3.803178902
O	1.517134744	0.953662417	3.54160716
O	2.922002853	5.048973634	5.601689563
O	4.311019606	2.362115499	5.854967161
O	2.907719079	3.30226083	3.805076778
O	4.424410118	0.915398982	3.537113837
H	1.331047218	2.176664802	6.801419458
H	4.484656614	1.12206862	2.594880973
H	4.267998522	2.002551453	6.752339583
H	1.563513673	1.294307996	2.636895223

$n = 6$
−1495.0949267361 Ry (PBE+U)
−1495.3836359 Ry (PBE0)

Ni	-0.026149812	1.635076173	4.704659896
Ni	1.508349988	4.194597084	4.723272705
Ni	2.948719711	1.594134399	4.665705467
Ni	4.359276433	4.235080043	4.751891061
O	5.897354433	5.022152094	5.891170454
O	1.559189292	2.420781364	5.730228221
O	-0.072126280	3.403411894	3.691440093
O	1.404604194	0.805786856	3.534801848
O	2.994988095	5.067657424	5.732579474
O	4.374195084	2.626290494	5.821706178
O	2.933872127	3.207715626	3.598907632
O	4.314005142	0.762724627	3.687359599
H	1.681793105	2.275228670	6.676138429
H	5.899030270	5.085975508	6.851779928
H	-0.193876420	3.548519564	2.745390154
H	4.313204384	2.764996538	6.774867194
H	1.389440431	0.736483120	2.574780200

$n = 8$
−1497.6838024809 Ry (PBE+U)
−1497.97694869 Ry (PBE0)

Ni	0.010231913	1.640113162	4.702279929
Ni	1.465818683	4.154274572	4.701878545
Ni	2.919767626	1.640047554	4.701680729
Ni	4.376508209	4.153115519	4.701053662

O	5.831534693	4.989598479	5.833813644
O	1.463605086	2.477527087	5.83900729
O	0.009023026	3.319422191	3.569299307
O	1.465855193	0.803360499	3.568602826
O	2.919493797	4.992861887	5.836838335
O	4.376705397	2.475710481	5.831754015
O	2.922258426	3.316342503	3.565877091
O	4.37963187	0.805722017	3.570430721
H	1.445861473	2.504830192	6.799662646
H	4.388444181	0.833194958	2.60978371
H	5.819415924	5.027099551	6.793919847
H	0.016729252	3.336842434	2.608431874
H	4.357325879	2.510963635	6.791711346
H	2.887681719	5.032369319	6.796777325
H	1.475918077	0.815745222	2.607548616
H	2.944116224	3.332262849	2.604968381

$Ni_3Fe_1O_8H_n$ single layer

$n = 0$

−1415.8476874440 Ry (PBE+U)

−1416.00678696 Ry (PBE0)

Fe	0.018263568	1.665835187	4.696212502
Ni	1.4710351	4.178192896	4.704233766
Ni	2.930203029	1.666733975	4.698394383
Ni	4.392261652	4.181695314	4.69021659
O	5.846736946	5.019698696	5.642593395
O	1.339984094	2.57347056	5.675547839
O	0.019617938	3.340524656	3.750454312
O	1.469536682	0.823349204	3.774011304
O	2.95006934	4.951484821	5.625544313
O	4.394356469	2.508492444	5.619390581
O	2.91313514	3.407803803	3.768799882
O	4.514735509	0.759036003	3.722442494

$n = 1$

−1417.1594050902 Ry (PBE+U)

−1417.338276 Ry (PBE0)

Fe	0.013472091	1.639424667	4.638853467
Ni	1.509518040	4.208984937	4.716089081
Ni	2.964401926	1.699263343	4.710245196
Ni	4.436449622	4.182231124	4.690343907
O	5.844168231	5.062389774	5.640331000
O	1.328387084	2.439081208	5.859748462
O	0.024112983	3.305539919	3.767064916
O	1.477063207	1.051533113	3.722435891
O	3.017091771	5.038192863	5.607226285
O	4.434139402	2.502402199	5.637630877
O	2.959566997	3.373493833	3.803508873
O	4.590530748	0.755256157	3.663069953
H	1.117771234	2.382089183	6.806270128

$n = 2$

−1418.4592877221 Ry (PBE+U)

−1418.68076517 Ry (PBE0)

Fe	-0.016019238	1.637830889	4.687444130
Ni	1.483107455	4.196329535	4.741803268
Ni	2.933604687	1.631447328	4.695493268
Ni	4.386072808	4.147551970	4.684486714
O	5.852209533	5.027414503	5.650484964
O	1.461347627	2.636633648	5.858638227
O	0.077088041	3.303726843	3.783210425
O	1.455290567	0.826152040	3.769067108

O	2.945768559	5.002902729	5.630869435
O	4.411129130	2.272542568	5.686663658
O	2.884647337	3.319289688	3.801085669
O	4.406352208	0.803500904	3.464786089
H	1.436074623	2.834559674	6.808785078
H	4.450553592	0.764689641	2.498809476

$n = 3$
−1419.7434627619 Ry (PBE+U)
−1419.973008 Ry (PBE0)

Fe	-0.017112676	1.722186277	4.653801149
Ni	1.497349042	4.179418074	4.720391961
Ni	2.911035820	1.649052346	4.689270843
Ni	4.349106538	4.140507420	4.658496161
O	5.756341687	5.060604877	5.738087571
O	1.442959568	2.525271444	5.916931116
O	0.024001476	3.346316992	3.748435273
O	1.398128210	0.963600262	3.752585923
O	2.962159640	5.006349221	5.614722198
O	4.388535000	2.328735437	5.679801851
O	2.904395879	3.251515121	3.723387081
O	4.428589412	0.776561760	3.500102022
H	1.494144748	2.585647256	6.880060386
H	4.531196599	0.705921791	2.540326537
H	5.519501308	5.163235403	6.672095148

$n = 4$
−1421.0547492370 Ry (PBE+U)
−1421.29761971 Ry (PBE0)

Fe	-0.040678080	1.601433830	4.665091219
Ni	1.478514305	4.146987548	4.675024241
Ni	2.887210231	1.681087016	4.760623184
Ni	4.372892819	4.209240861	4.747498833
O	5.866605377	4.993426835	5.629375373
O	1.256883954	2.489399907	5.627537023
O	-0.083169890	3.158240570	3.490676868
O	1.521375766	0.703511677	3.563263128
O	2.851307207	5.055029880	5.892820909
O	4.409947946	2.592003506	5.855369467
O	2.950577541	3.436902781	3.774478005
O	4.415173638	0.810080182	3.722993174
H	-0.490349158	3.003190679	2.624542443
H	4.721741139	2.749325559	6.758519317
H	2.663192511	5.081522552	6.839092107
H	1.708153387	0.509278991	2.633757041

$n = 5$
−1422.3492669235 Ry (PBE+U)
− 1422.60075754 Ry (PBE0)

Fe	0.010198816	1.566619784	4.743380683
Ni	1.428675300	4.116924466	4.685752722
Ni	2.893533392	1.627114174	4.719851804
Ni	4.391018445	4.216728820	4.752083196
O	5.778894006	5.032881608	5.751173023
O	1.292099840	2.366639874	5.711351945
O	-0.027198991	3.169675663	3.559406598
O	1.489213496	0.758019273	3.504373196
O	2.828583847	4.984340753	5.840450205
O	4.369619581	2.589511746	5.809153570
O	3.014247481	3.367384767	3.657881271
O	4.464437051	0.794571716	3.728592981
H	-0.187256171	3.013241386	2.620648222
H	4.548634660	2.717986181	6.750714985
H	2.650865610	5.062195793	6.784799902
H	1.414525901	0.717957108	2.544448062
H	3.116751963	3.476432843	2.705268024

$n = 6$
−1423.6353072578 Ry (PBE+U)
−1423.89139489 Ry (PBE0)

Fe	0.002360241	1.643714181	4.698801814
Ni	1.465529570	4.119303883	4.682712548
Ni	2.915741589	1.643687912	4.703494180
Ni	4.364189668	4.197260979	4.723592558
O	5.858179357	5.032756601	5.848160377
O	1.299631531	2.384373338	5.715534750
O	-0.028459045	3.287923662	3.557016689
O	1.441714987	0.792077147	3.557035087
O	2.881157553	4.971059297	5.837354988
O	4.392372065	2.495037418	5.847521889
O	2.949451360	3.344041088	3.569639609
O	4.528940250	0.902762432	3.684300993
H	6.107155372	5.181244257	6.767651193
H	-0.274120730	3.154569954	2.634462528
H	4.575636448	2.601757822	6.787497966
H	2.851344541	4.957822063	6.798710470
H	1.265709308	0.692514596	2.614825886
H	2.987465535	3.357563581	2.608668056

$n = 7$
−1424.896999410 Ry (PBE+U)
−1425.19455057 Ry (PBE0)

Fe	0.145523136	1.718893980	4.919074387
Ni	1.491261434	4.140051652	4.641326705
Ni	2.911527239	1.697402812	4.690203131
Ni	4.372384362	4.179149054	4.680727558
O	5.849524045	4.978938858	5.836079019
O	1.495130553	2.529540721	5.882369336
O	-0.005398121	3.297535857	3.562847780
O	1.438429003	0.833860241	3.559926298
O	2.919405839	5.015078462	5.768843341
O	4.384490939	2.501629342	5.851194831
O	2.954634859	3.356909489	3.476174788
O	4.447265478	0.876224311	3.645621718
H	4.389470861	0.851418431	2.685705734
H	6.034237102	4.735501344	6.749278342
H	-0.098378076	3.131324504	2.620001129
H	4.198475484	2.564919564	6.793431926
H	2.819453964	4.965808656	6.724068211
H	1.318950997	0.877614305	2.606532525
H	2.942636975	3.375086529	2.514715575

n = 8
−1426.126278458 Ry (PBE+*U*)
−1426.40044836 Ry (PBE0)

Fe	0.003521666	1.651984825	4.695780212
Ni	1.451671566	4.15722978	4.694711522
Ni	2.910506928	1.644938766	4.705401618
Ni	4.382541542	4.163663116	4.709471354
O	5.840874743	4.968681058	5.880036624
O	1.463461148	2.485608946	5.866776075
O	-0.008641136	3.36205699	3.508629263
O	1.48791558	0.78849357	3.511995959
O	2.91053551	4.996504676	5.823913391
O	4.338177835	2.502398891	5.88411103
O	2.925289926	3.319575782	3.585428868
O	4.360299932	0.806594429	3.544298692
H	1.466900575	2.534515998	6.827197504
H	4.378359597	0.77824327	2.583542076
H	5.730210066	4.766524171	6.813863037
H	0.125296798	3.599242784	2.585820462
H	4.126401228	2.509925428	6.821881108
H	2.848355666	5.051348357	6.781499896
H	1.739151587	0.795796922	2.583429413
H	2.995095893	3.278076353	2.627531

B.5. References

1. Chen, J.; Wu, X.; Selloni, A., Electronic structure and bonding properties of cobalt oxide in the spinel structure. *Phys. Rev. B* **2011,** *83* (24), 245204.
2. Sit, P. H. L.; Zipoli, F.; Chen, J.; Car, R.; Cohen, M. H.; Selloni, A., Oxidation State Changes and Electron Flow in Enzymatic Catalysis and Electrocatalysis through Wannier-Function Analysis. *Chem. Eur. J.* **2011,** *17* (43), 12136-12143.
3. Sit, P. H. L.; Zipoli, F.; Chen, J.; Car, R.; Cohen, M. H.; Selloni, A., Oxidation state changes and electron flow in enzymatic catalysis and electrocatalysis through Wannier‐function analysis. *Chem- Eur. J.* **2011,** *17* (43), 12136-12143.
4. Gygi, F.; Fattebert, J.-L.; Schwegler, E., Computation of maximally localized Wannier functions using a simultaneous diagonalization algorithm. *Comput. Phys. Commun.* **2003,** *155* (1), 1-6.
5. Gygi, F., Architecture of Qbox: A scalable first-principles molecular dynamics code. *IBM J. Res. Dev.* **2008,** *52* (1.2), 137-144.
6. Trotochaud, L.; Young, S. L.; Ranney, J. K.; Boettcher, S. W., Nickel-iron oxyhydroxide oxygen-evolution electrocatalysts: the role of intentional and incidental iron incorporation. *J. Am. Chem. Soc* **2014,** *136* (18), 6744-53.
7. Corti, H.; Fernández-Prini, R., Behaviour of the mercury, mercuric oxide electrode in alkaline solutions in the temperature range 298–363 K. *J. Chem. Soc. Faraday Trans. I* **1982,** *78* (2), 545-554.
8. Tkalych, A. J.; Yu, K.; Carter, E. A., Structural and Electronic Features of β-$Ni(OH)_2$ and β-NiOOH from First Principles. *J. Phys. Chem. C* **2015,** *119* (43), 24315-24322.
9. Mansour, A. N.; Melendres, C. A., XAFS investigation of the structure and valency of nickel in some oxycompounds. *Physica B: Condensed Matter* **1995,** *208–209*, 583-584.
10. Friebel, D.; Louie, M. W.; Bajdich, M.; Sanwald, K. E.; Cai, Y.; Wise, A. M.; Cheng, M. J.; Sokaras, D.; Weng, T. C.; Alonso-Mori, R.; Davis, R. C.; Bargar, J. R.; Norskov, J. K.; Nilsson, A.; Bell, A. T., Identification of highly active Fe sites in (Ni,Fe)OOH for electrocatalytic water splitting. *J. Am. Chem. Soc.* **2015,** *137* (3), 1305-13.

APPENDIX C: Supporting Information for Chapter 4[§]

C.1. Figures

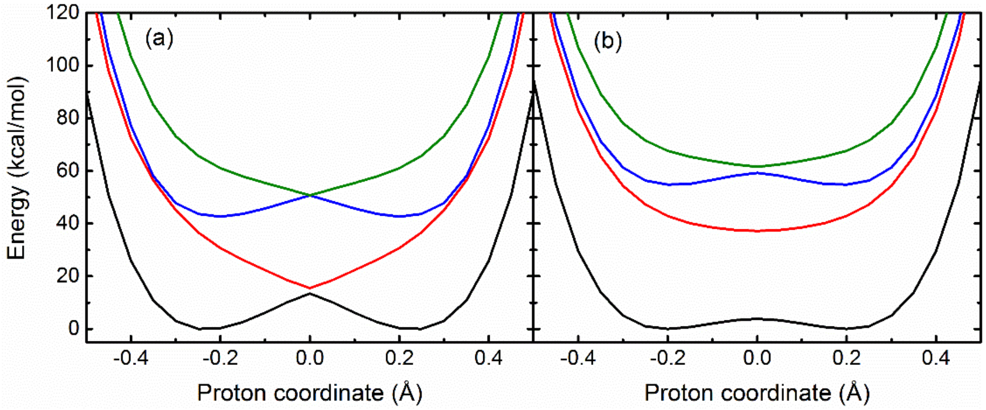

Figure C.1. Four-state averaged CASSCF proton potential energy curves for the (a) open and (b) stacked geometries of the phenoxyl-phenol system. All results shown in this figure were generated with the 6-31G basis set using MolPro.

[§] Reproduced with permission from:

Harshan, A. K.; Yu, T.; Soudackov, A. V.; Hammes-Schiffer, S. *J. Am. Chem. Soc* **2015,** *137* (42), 13545-13555. Copyright 2015 American Chemical Society

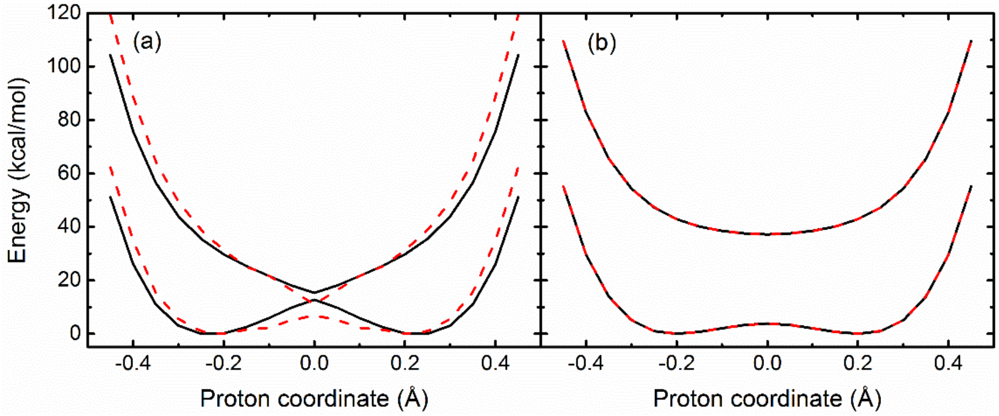

Figure C.2. CASSCF (solid black lines) and CASPT2 (dashed red lines) proton potential energy curves for the (a) open and (b) stacked geometries of the phenoxyl-phenol system. All results shown in this figure were generated with the 6-31G basis set using MOLCAS.

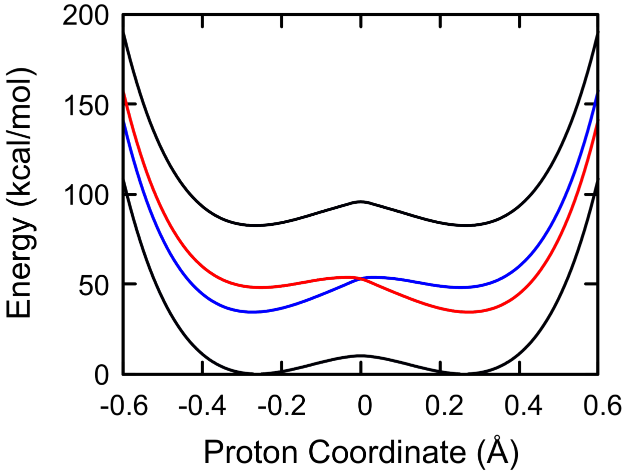

Figure C.3. Diabatic (blue and red) and adiabatic (black) energy curves for the stacked benzyl/toluene structure given in Ref [1]. These results are obtained from caclulations using two-state averaged CASSCF(3,6) with the 6-31G** basis set. Semiclassical parameters for this structure are calculated to be: electronic coupling V^{el} = 14965 cm^{-1}, proton transfer time, τ_p (fs)=3.55 fs, electron transfer time, τ_p (fs) = 0.35 fs, and adiabaticity parameter, $p = \tau_p/\tau_e$ = 10.0. Adiabatic coupling, V^{ad} =50.9 cm^{-1}, semiclassical coupling, V^{sc} = 50.5 cm^{-1}, nonadiabatic coupling, V^{na} = 157 cm^{-1}, and true vibronic coupling, V^{full} = 50.8 cm^{-1}.

C.2. Transition State Geometries from M06-2X/6311+G** Calculations

1. Open TS

C	-0.39280033	-2.06860660	0.00000000
O	-0.82873155	-0.84774822	0.00000000
H	0.00000000	0.00000000	0.00000000
C	0.99420344	-2.37493095	0.00000000
C	1.40978980	-3.68741611	0.00000000
C	0.47933002	-4.72950621	0.00000000
C	-0.88734752	-4.44184144	0.00000000
C	-1.32551216	-3.13697647	0.00000000
H	1.70350816	-1.55865867	0.00000000
H	2.46707498	-3.91338506	0.00000000
H	0.81637527	-5.75608459	0.00000000
H	-1.60578419	-5.24969308	0.00000000
H	-2.37707620	-2.88788567	0.00000000
O	0.82873155	0.84774822	0.00000000
C	0.39280033	2.06860660	0.00000000
C	1.32551216	3.13697647	0.00000000
C	0.88734752	4.44184144	0.00000000
C	-0.47933002	4.72950621	0.00000000
C	-1.40978980	3.68741611	0.00000000
C	-0.99420344	2.37493095	0.00000000
H	2.37707620	2.88788567	0.00000000
H	1.60578419	5.24969308	0.00000000
H	-0.81637527	5.75608459	0.00000000
H	-2.46707498	3.91338506	0.00000000
H	-1.70350816	1.55865867	0.00000000

2. Stacked TS

C	1.46355300	0.97546600	-0.18858600
O	1.18607200	2.23246600	-0.02615000
H	0.00002600	2.36859100	-0.00009100
C	0.95674400	0.24412100	-1.29826100
C	1.19267900	-1.11073800	-1.40758000
C	1.95332700	-1.77115700	-0.44525500
C	2.49992400	-1.05924800	0.63007700
C	2.25736200	0.28625900	0.76859600
H	0.38076400	0.78189400	-2.03850700
H	0.78294900	-1.66219100	-2.24251300
H	2.13549100	-2.83267000	-0.53621300
H	3.10290200	-1.57721000	1.36309000
H	2.64663100	0.85665100	1.60046500
O	-1.18602200	2.23251500	0.02617000
C	-1.46351500	0.97550800	0.18857400
C	-0.95679400	0.24417400	1.29829100

C	-1.19281400	-1.11066600	1.40765000
C	-1.95343600	-1.77108300	0.44529900
C	-2.49987000	-1.05920100	-0.63013000
C	-2.25723600	0.28629300	-0.76867300
H	-0.38066600	0.78190700	2.03845200
H	-0.78320800	-1.66210300	2.24265400
H	-2.13569000	-2.83257600	0.53630600
H	-3.10277100	-1.57717000	-1.36320100
H	-2.64637900	0.85666700	-1.60061400

C.3. Reference

1. Skone, J. H.; Soudackov, A. V.; Hammes-Schiffer, S., Calculation of vibronic couplings for phenoxyl/phenol and benzyl/toluene self-exchange reactions: implications for proton-coupled electron transfer mechanisms. *J. Am. Chem. Soc* **2006,** *128* (51), 16655-16663.

APPENDIX D: Supporting Information for Chapter 5

D.1. Coordinates for EPT and E2PT Reactant and Product Structures

1-H_2 Reactant (EPT)

E = –807.498132 a.u.

C	0.483863	-1.157332	-0.156580
C	1.871623	-1.054098	-0.034358
C	2.463625	0.203611	0.116935
C	1.668354	1.351271	0.144153
C	0.277971	1.252494	0.021703
C	-0.311216	-0.009332	-0.129203
H	0.028930	-2.134530	-0.275653
H	3.541244	0.290576	0.215542
H	2.124453	2.328043	0.262532
H	-1.387614	-0.097623	-0.227206
O	-0.452482	2.412577	0.052221
H	-1.416485	2.236838	-0.023232
O	2.607675	-2.219679	-0.064539
H	3.550833	-2.010115	-0.010331
O	-3.211141	2.097810	-0.192432
C	-3.998433	3.168126	-0.534987
C	-3.531948	4.451533	0.191338
H	-4.120836	5.304489	-0.150717
H	-3.673491	4.335394	1.267938
H	-2.476331	4.636965	-0.015098
C	-3.691865	3.319974	-2.081943
H	-3.995496	2.420416	-2.616510
H	-4.273142	4.174560	-2.432587
H	-2.628857	3.507886	-2.229099
C	-5.489945	2.895562	-0.320491
C	-6.449720	3.835235	-0.728378
C	-5.923370	1.718145	0.301395
C	-7.810867	3.600473	-0.521698
H	-6.139322	4.753289	-1.216882
C	-7.285969	1.481533	0.509317
H	-5.191092	0.989560	0.628983
C	-8.236027	2.420327	0.097138
H	-8.537392	4.336839	-0.849060
H	-7.599683	0.566382	1.000611
H	-9.293171	2.238568	0.259195

1-H_2 Product (EPT)

E = –807.539802 a.u.

C	0.624208	-1.231081	-0.159235
C	2.019423	-1.004624	-0.049011
C	2.536798	0.309104	0.075073
C	1.673674	1.376997	0.090493
C	0.241339	1.189280	-0.018565
C	-0.243927	-0.169903	-0.145697
H	0.268889	-2.250727	-0.252450
H	3.608987	0.453671	0.159436
H	2.045331	2.390854	0.184469
H	-1.313271	-0.322126	-0.232619
O	-0.551238	2.183376	-0.001359
H	-2.383678	2.083640	-0.058905
O	2.811813	-2.090639	-0.066955
H	3.747118	-1.840669	0.000166
O	-3.355083	1.955212	0.002029
C	-4.023414	3.118184	-0.513958
C	-3.551471	4.362768	0.259504
H	-4.085770	5.255690	-0.074729
H	-3.729811	4.232886	1.330171
H	-2.481203	4.520396	0.098231
C	-3.700989	3.263772	-2.012249
H	-4.009034	2.366029	-2.554440
H	-4.220210	4.124147	-2.441222
H	-2.625372	3.406757	-2.150169
C	-5.525644	2.910646	-0.314024
C	-6.429316	3.897003	-0.744456
C	-6.042606	1.756867	0.289583
C	-7.805796	3.735282	-0.576874
H	-6.056889	4.798352	-1.220704
C	-7.422637	1.591227	0.457912
H	-5.362127	0.987737	0.631914
C	-8.311694	2.578051	0.025994
H	-8.482087	4.510800	-0.921559
H	-7.796388	0.690310	0.933936
H	-9.381035	2.449873	0.156751

2-H_2 Reactant (E2PT)

E = –1097.535711 a.u.

O	-2.369994	0.191481	-1.171581
H	-2.593923	-0.732591	-1.516255
N	-2.263443	-2.398436	-1.689660
C	-1.173492	0.049891	-0.515344
C	-0.420058	1.185703	-0.209107
H	-0.797715	2.162463	-0.491848
C	-0.698666	-1.227951	-0.150875

C	-1.549638	-2.457615	-0.397211
H	-2.316531	-2.520629	0.383858
H	-0.933925	-3.365763	-0.321575
C	-3.399749	-3.338894	-1.726367
H	-3.033236	-4.374747	-1.623339
H	-4.038534	-3.127311	-0.864745
C	-4.189204	-3.196386	-3.028750
H	-5.006404	-3.925112	-3.029814
H	-4.642892	-2.198551	-3.060642
C	-3.283984	-3.390963	-4.251817
H	-2.940257	-4.432758	-4.286908
H	-3.840362	-3.204375	-5.176165
C	-2.068212	-2.460017	-4.161949
H	-2.394392	-1.418303	-4.264827
H	-1.361132	-2.659583	-4.973598
C	-1.346017	-2.627626	-2.824793
H	-0.519648	-1.916936	-2.742489
H	-0.920141	-3.643232	-2.753047
C	0.804324	1.071614	0.456141
C	1.289164	-0.192560	0.808741
C	0.535223	-1.329998	0.498404
H	0.919628	-2.307578	0.772064
H	1.377307	1.961856	0.691619
O	2.495832	-0.377417	1.438711
H	2.882598	0.477215	1.728386
O	3.661106	1.875034	2.622802
C	4.805473	2.518845	2.225032
C	4.254270	3.507697	1.117294
H	5.111386	4.076126	0.751618
H	3.812960	2.934561	0.302693
H	3.518616	4.186294	1.547837
C	5.795873	1.534392	1.563266
H	6.655693	2.081798	1.173470
H	6.149022	0.812328	2.302718
H	5.307211	1.002561	0.744982
C	5.462288	3.309894	3.360811
C	6.588409	4.108712	3.109361
C	4.977744	3.219562	4.671424
C	7.217984	4.799711	4.147413
H	6.982695	4.189213	2.101795
C	5.607552	3.909756	5.712248
H	4.109540	2.604234	4.875916
C	6.729667	4.702007	5.454411
H	8.089654	5.409300	3.933901
H	5.222173	3.825757	6.722943
H	7.217028	5.237581	6.261999

2-H_2 Product (E2PT)

E = –1097.593100 a.u.

O	-2.496118	0.298936	-1.131329
H	-2.658092	-1.371818	-1.813854
N	-2.296233	-2.344985	-1.704045
C	-1.352087	0.219738	-0.550126
C	-0.560337	1.390532	-0.271976
H	-0.977212	2.351114	-0.558026
C	-0.800626	-1.066891	-0.158168
C	-1.647640	-2.300465	-0.340851
H	-2.473254	-2.300769	0.375944
H	-1.070795	-3.215691	-0.208015
C	-3.452488	-3.309710	-1.741516
H	-3.040530	-4.297697	-1.522413
H	-4.127042	-3.020604	-0.935410
C	-4.144769	-3.276228	-3.100475
H	-4.946115	-4.020507	-3.084734
H	-4.616592	-2.296973	-3.240276
C	-3.162705	-3.549373	-4.246031
H	-2.795352	-4.579998	-4.176140
H	-3.671882	-3.450737	-5.208685
C	-1.979204	-2.577515	-4.171103
H	-2.321116	-1.555809	-4.370890
H	-1.222788	-2.816179	-4.923851
C	-1.304706	-2.624046	-2.803748
H	-0.514386	-1.878683	-2.715779
H	-0.884445	-3.611090	-2.598323
C	0.663010	1.306545	0.340475
C	1.224491	0.033020	0.723963
C	0.434411	-1.141721	0.440326
H	0.852204	-2.103086	0.725068
H	1.241317	2.200219	0.550771
O	3.728833	1.729620	2.854782
C	4.811909	2.466358	2.268947
C	4.255024	3.444597	1.218601
H	5.054405	4.052446	0.787402
H	3.772114	2.888195	0.410189
H	3.519521	4.112617	1.674562
C	5.805045	1.489047	1.613515
H	6.646603	2.029475	1.173193
H	6.195057	0.787187	2.355295
H	5.308045	0.922386	0.820942
C	5.508249	3.234918	3.394951
C	6.616670	4.048892	3.105355
C	5.083372	3.141987	4.726721
C	7.280835	4.747191	4.116176

H	6.969928	4.133751	2.082874
C	5.747040	3.841166	5.742332
H	4.230658	2.520959	4.969373
C	6.848598	4.645683	5.443122
H	8.137322	5.364998	3.866343
H	5.398180	3.755568	6.766430
H	7.362429	5.187116	6.230377